Assessment of Geothermal Application for Electricity Production from the Prairie Evaporite Formation of Williston Basin in South-West Manitoba

by

Niloofar Firoozy

A Thesis submitted to the Faculty of Graduate Studies of
The University of Manitoba
in partial fulfilment of the requirements of the degree of

MASTER OF SCIENCE

Department of Civil Engineering
University of Manitoba
Winnipeg

Abstract

In this thesis, the potential of enhanced geothermal system to provide adequate energy to a 10 MW electricity power plant from Prairie Evaporite Formation of Williston Basin was investigated. This formation partly consists of halite with low thermal resistance and high thermal conductivity, which translates into a lower drilling length to reach the desired temperature, comparing to other rock types.

To this end, two numerical models with experimental data in south-west Manitoba (i.e. Tilston) and south-east Saskatchewan (i.e. Generic) were designed. The thermal reservoirs were located at 1.5 km (Tilston site) and 3 km (Generic site) with approximate thicknesses of 118 m. Considering an injection brine of 6% NaCl at 15°C, the final derived temperature at wellhead of the production wells were 43°C and 105°C respectively.

Finally, the Generic site was concluded as a suitable candidate for electricity production by providing higher surfaced fluid temperature than the minimum of 80°C.

Acknowledgement

First and foremost, I would like to thank my academic advisor Dr. Hartmut Holländer, for his direction, support, and encouragement through my Master's studies. Furthermore, I would like to thank my colleagues at Geotechnical office and Groundwater team who made my workplace a professional and cheerful one.

I would like to express my appreciation to my committee members Dr. Marolo Alfaro and Dr. Stefan Cenkowski for their effort in evaluating my thesis.

Finally, I would like to extend my gratitude to Manitoba Hydro for the financial support of this research.

To my wonderful parents who have taught me to be a strong, hardworking woman and because of all their sacrifices and supports through my way.

There is no way to thank them enough.

Contents

List of Tables

List of Figures

Nomenclature

A_0	Surface heat generation of the crystalline basement, $\mu w/m^3$
$\dot{A}$	Distance between the formations, m
ΔA	Thickness of the formations, derived by kriging method, m
b	Boltzmann constant, J/K
b_c	Corresponding boundary condition
c	Average specific heat capacity of solid and liquid phases, J/kg/K
c_f	Specific heat capacity of fluid, J/kg/K
$c_{p,n}$	Normalized value of specific heat capacity, °C
c_s	Specific heat capacity of solid, J/kg/K
$\dot{C}(e)$	Electricity production capacity, W
d	Well diameter, m
D	Slope of the empirical/statistically derived heat flow (Q) vs. Heat generation and (A_0) relation, km
D_{Dp}	Displacement of production well from the vertical at depth of z, m
D_{Tp}	Depth of production well, m
D_w	Distance between injection and production well at the reservoir, m
f	Degree of freedom
$\tilde{f}$	Pipe (well) friction factor
g	Gravitational acceleration, m/s^2
h	Thickness of the reservoir, m
$\dot{h}$	Fracture height, m
h_h	Hydraulic head, m
h_p	Hydro-static pressure, m
k	The intrinsic permeability of porous media, m^2
K_{fr}	Hydraulic conductivity of fractures, m/s
K_s	Average hydraulic conductivity of the reservoir, m/s
K_x	Hydraulic conductivity of the reservoir at X direction, m/s
K_y	Hydraulic conductivity of the reservoir at Y direction, m/s
K_z	Hydraulic conductivity of the reservoir at Z direction, m/s
L	Fractures' length, m

M	Mass, kg
$\dot{m}$	Total mass flow in the well, kg/s
N_a	Avogadro's number, 1/mol
N_{eq}	Number of equations
P	Pressure, mpa
P_{op}	Static formation pressure, Pa
ΔP	Pressure drop, Pa
ΔP_{dp}	Production well dynamic pressure drop, Pa
ΔP_{fp}	Production well frictional pressure drop, Pa
ΔP_{ip}	Interface pressure, Pa
ΔP_0	Surface over pressure, Pa
q	Darcy flow velocity, m/s
Q	Flow rate, m^3/day
Q_r	Reduced heat flow, W/m^2
$\dot{Q}$	Heat loss, W/m
r	Cylindrical radius, m
R	System's matrix with N_{eq} rows and columns
Re	Reynolds number, [ ]
s	Fracture aperture, m
S_0	Prediction location in kriging formula
T	Average temperature of solid and liquid phases, K
t	Time, s
T_b	Temperature of crystalline basement surface, °C
T_i	Temperature at the injection well, °C
T_{in}	Input temperature of an EGS system, °C
T_f	Temperature of the liquid phase, K
T_{out}	Output temperature of an EGS system, °C
T_p	Temperature at the production well, °C
T_s	Temperature of the solid phase, K
T_z	Temperature at depth z, °C

u_i	Average fluid velocity at injection well, m/s
u_p	Average fluid velocity at production well, m/s
VHC	Volumetric heat capacity, $J/m^3°C$
V_t	Total volume of the solid phase, m^3
V_v	Void volume of the solid phase, m^3
V_0	Initial volume, m^3
x	Primary variable for error estimation
z	Depth, m
Z	The groundwater elevation from a defined datum, m
$\hat{Z}$	The measured value at specific location for kriging formula
α	Thermal diffusivity, m^2/s
β	Compression coefficient, 1/K
γ	Thermal expansion coefficient, 1/K
δ	Angle between two consecutive edges of supermesh, radian
ε	Error of the primary variable
λ	Average thermal conductivity of solid and liquid phases, W/mk
λ_f	Thermal conductivity of the fluid phase, W/mk
λ_s	Thermal conductivity of solid phase, W/mk
μ	Dynamic viscosity, $N\text{-}s/m^2$
ν_i	Kinematic viscosity of fluid at injection well, m^2/s
ν_p	Kinematic viscosity of fluid at production well, m^2/s
ξ	Dimensional solution vector
ρ	Average density of solid and liquid phases, kg/m^3
ρ_f	Density of liquid phase, kg/m^3
ρ_s	Density of solid phase, kg/m^3
φ	Porosity, (-)
ω_i	Defined weight for kriging formula

Acronyms

AB/TR	Forward Adams-Bashforth/Backward Trapezoid Rule
AFM	Advancing Front Method
BC	Boundary Condition
BH	Bottom hole temperature
DLS	Dominant Land Survey
EGS	Enhanced Geothermal System
FEFLOW	Finite Element Subsurface Flow Simulation System
FEM	Finite Element Method
GIS	Geographic Information System
FE/BE	Forward/Backward Euler
GHP	Ground Heat Pipe
HDR	Hot Dry Rock
IC	Initial Condition
NEGB	North Eastern German Basin
ORC	Organic Rankine Cycle
TGI	Target Geoscience Investigation
TVD	Total vertical depth
RMS	Root Mean Square
WCSB	Western Canadian Sedimentary Basin

Chapter 1. Introduction

Overview

Geothermal energy is the use of thermal energy from interior parts of the earth. Geothermal systems are divided into various types based on specific thermal properties of their reservoirs.

In this chapter, the principal of the geothermal energy as a renewable source of power is introduced. Then the geothermal systems' types, specific fields' criteria, and applications are proposed. Lastly, the objective of this research considering the geothermal potential of Canada and specifically Manitoba being presented.

1.1 Geothermal Energy

Humans' life depends on natural energy resources. By increasing the population, the demands for energy has been raised as well. The application of fossil fuels, as the main source of energy, has been increased proportionally since 1960, which led to enormous environmental hazards such as greenhouse effects.

Based on the statistical review of world energy, the highest energy consumption is attributed to the fossil fuels (e.g. oil, gas and coal) which provided more than 45000 TWh per year in 2014 (Con-struc, 2015). The limited source of fossil fuels cannot provide adequate energy for the increasing demand continuously. Therefore, other types of energy resources have been introduced to supply the growing demand. The application of the renewable energies, which provide an unlimited source of energy with minimum environmental impacts, commencing in 1990 with a high growing pace within the recent decade (Con-struc, 2015).

As a renewable source of energy, geothermal has been applied for various purposes worldwide. The foundation of the geothermal energy is heat. The extracted heat is either produced by nuclear reactions within earth's core for deep geothermal systems, which will last for billions of years, or solar radiation for shallow geothermal systems (Ghosh and Prelas, 2011). The inner core of the Earth has the potential to generate 42×10^{12} W energy based on the generated heat of approximately 4300°C; this heat cannot be trapped and utilized totally due to losses on its path to the surface and particular geophysical and geological properties of earth's formations (Ghosh

and Prelas, 2011). Thus, geothermal energy is attributed to the portion of the earth's core heat that could be utilized for energy production.

1.2 Geothermal systems

1.2.1 **Geothermal potential**

Geothermal gradient refers to the variation of temperature as a function of depth, which estimates the geothermal potential of specific sites. The geothermal potential of a site was evaluated by vast investigations regarding lithology, topography and geochemical and hydrological properties.

Based on Gupta and Roy (2006) a geothermal potential inspection should provide adequate information on the initial qualifications of geothermal fields such as estimation of the shape, size, and depth of the reservoir (geothermal source), recharge water and homogeneity of the target formation, determination and study of bedrock formation, surface temperature, and accessibility of the site (Ghosh and Prelas, 2011, Gupta and Roy, 2006, Lumb, 1981). The existence of a large source of heat is the first and the most significant priority for a field to be considered as a geothermal source. Several methods are used to evaluate the existence of reservoirs such as satellite imagery, aerial photography and geologic and structural mapping (Gupta and Roy, 2006). After verification of reservoir presence, by using temperature data derived from geochemical and geophysical surveys and temperature gradient hole, the reservoir size can be estimated.

1.2.2 **Reservoir types**

Thermal reservoirs have been categorized into five different classes based on:

- The production fluid's chemical composition after extraction (whether the fluid was injected artificially or presents naturally),
- Exergy of the system
- Aquifer thickness
- Geochemical fluid properties in the reservoir, and
- Temperature and porosity of the reservoir (Gupta and Roy, 2006).

The exergy of a system is defined as the maximum usable energy produced through the equilibrium process of the reservoir and its surrounding area. Hydrothermal and Conductive (Hot Dry Rock) Systems are the two main classes which are based on the existence of hot water/fluid within the reservoirs, the reservoir's formation and trapped heat (Gupta and Roy, 2006).

Hydrothermal systems: This class has been divided into vapor dominated, hot water, geo-pressured and magma subcategories. For all these categories, the fluid (vapor) exists at high temperature and pressure within the reservoir. Most of the recent geothermal plants like Larderello (Italy), Geysers (USA), Cerro Prieto (Mexico), Wairakei (New Zealand), Reykjavik (Iceland), Salton Sea (USA) and Otake (Japan) are vapor dominated based on highly active tectonic regions with capability of producing fluid with 180°C temperature (Gupta and Roy, 2006).

Hot dry rock systems (HDR): Based on the definition of the U.S. Energy Research and Development Administration (ERDA) a HDR geothermal resource is "The heat stored in rocks

within 10 km of the surface from which the energy cannot be economically produced by natural hot water or steam" (Panel, 1977). The absence of a hot aquifer or steam at hot dry rock (HDR) systems makes these systems applicable at most of the geothermal fields.

The working principle of these systems relies on hydraulic fracturing (fracking) and fluid circulation within the reservoir. A high-pressure fluid is injected into rock formations at 3-7 km depth, depending on the reservoir's location, and the heated fluid is extracted at the production well. The injected fluid can be water or any other kind of fluid e.g. butane, pentane or a refrigerant related on the chemical properties of the geothermal system which is also called reservoir (Grasby et al., 2012, Li and Lior, 2015)

Hydraulic fracturing is the other crucial factor for HDR systems application, which increases the permeability of rock formations by providing cracks to ease fluid circulation. The pressure required for fracturing varies for different sites, based on the formation and location of the reservoir. For depths more than 500 meters, the fractures growth will be aligning to the highest stress or perpendicular to the least stress; therefore, cracks will be expanding vertically more than horizontally (Fisher and Warpinski, 2012). Besides, by increasing the fractures volume, more pressure is required to maintain the cracks open. As a result, a large volume of fluid must be granted for hydraulic fracturing.

Although induced fractures increase the efficiency of applied systems in HDR fields, some concerns regarding earthquake activities limit the application for specific regions with seismic potentials. Any earthquake hazards from geothermal applications or development would result in ceasing the project e.g. the case in Basel, Switzerland, in which incentive of the reservoir caused a 3.4 magnitude earthquake (Karvounis et al., 2014). Considering potential seismic reactions

requires knowledge regarding the fractures size and openings at the geothermal field. Therefore, operating geothermal plants at HDR fields required determination of appropriate locations where the chemical properties, permeability, and potential seismic criteria are met. Based on these criteria, the regions with recent volcanism, high heat flow, and localized radiometric heat source, are the most obvious regions where HDR systems can be used (Gupta and Roy, 2006).

1.2.3 **Direct applications and electricity production**

The most important factor in power generation for any geothermal field is related to the stored heat in the reservoir. In HDR systems and hydrothermal systems, the stored heat is depending on the depth of reservoir. The stored heat at depths of 3.5 and 10 km was estimated in several studies (e.g., Roberts, 1978, Rowley, 1982, Tester, 2005). At depth of 3 km, 42.67×10^{6} EJ stored heat was estimated for continental regions, including 34.14×10^{6} EJ (80%) from HDR and 8.53×10^{6} EJ (20%) from hydrothermal resources (Roberts, 1978). The stored heat increased exponentially by the depth and at 10 km it was approximated as 403×10^{6} EJ (Rowley, 1982). Although the stored heat can provide considerable energy for various applications, only a percentage of it is accessible due to technical difficulties and high drilling costs.

Temperature of the reservoir defines the application of a geothermal system. Based on the temperature, geothermal sources are classified into three categories. Low, intermediate and high temperatures, which cover ranges less than 80°C, 80-150°C and more than 150°C temperature. Electricity production requires intermediate to high temperature; hence, the minimum of 80°C is required within geothermal fields to be considered for electricity power generation. Lower temperatures cannot provide adequate energy for electricity production; however, they still can

be used for direct applications such as heating/cooling systems and heat pumps (Grasby et al., 2012).

Enhanced Geothermal Systems (EGS) are designed for HDR systems where no fluid exists and the reservoir is impermeable or has low permeability. It is anticipated that for most of the geothermal fields using HDR systems, EGS will provide more than 100,000 MW electricity for each field within the next 50 years (Ghosh and Prelas, 2011).

In this research, the study area is located in a sedimentary basin and the thermal reservoir is comprised of low permeable rock; therefore, EGS was applied in this study, which is going to be discussed in Chapter 3.

Although electricity generation has been the main concern of geothermal applications, nowadays, direct applications of low thermal sources are increasing. Hot water from low temperature resources can be directly used for various purposes such as residential regions' heating and cooling system operation to heating of greenhouses for growing vegetables and flowers (Ghosh and Prelas, 2011). Geothermal heat pumps are the most functional direct application of low temperature geothermal sources for home heating and air conditioning purposes. The principal of the heat pumps is transferring heat from the house to the warmer outdoor during the summer and spring (warming seasons) and vice versa for the cold seasons (Ghosh and Prelas, 2011). The ground heat pumps (GHPs) are electrical utilities that transfer heat from the cool place to the warm one that makes the warm place warmer and cool space cooler. The GHPs are installed in the buildings and they consist of several plastic or metal pipes, which are placed for several hundred meters into the ground. For the application of GHPs at extremely cold conditions, anti-freezing additives need to be added to the heat exchange fluid.

1.2.4 **Open/close loop systems**

Open and close loop systems both are used for direct applications of geothermal energy; however, they have some initial differences. Open loop systems circulate hot water directly from the geothermal source in which plenty of vertically accessible space is required. For close loop systems, a combination of vertical or horizontal pipes would be applied to the outdoor space. The pipes orientation is in proportion to the amount of available space outside of the building, and the geothermal heat exchanger is placed inside the building (Ghosh and Prelas, 2011, Grasby et al., 2012). The most significant reason for applying the closed loop system for a building is the chemical property of the groundwater. Close loop systems require a minimum 1-2 m depth trenches for installing the system in contrast to 20-120 m requirements of vertical space for open loops. This system of closed loop are designed for the lowest temperature of 0°C, for colder environments more excavation is required to place the loops in deeper elevations. The direct use of geothermal systems is economically beneficial specifically for residential locations (Ghosh and Prelas, 2011).

1.3 Geothermal potential of Canada and Manitoba

Canada has a large potential for geothermal energy production (Grasby et al., 2012). High thermal resources are recognized at the volcanic belt within the Canadian Cordillera due to difference between the oceanic and the continental heat flux which creates a border with high heat flow (as high as 150°C/km) along the volcanic belt (Meer et al., 2014, Lewis and Hyndman, 1976). The Canadian Cordillera covers the west ocean shore of the British Columbia from US border to Yukon. At the center and in the north-west of Canada, the Western Canadian

Sedimentary Basin (WCSB) covers most of the territories from Alberta to north-east British Columbia (BC), southern Saskatchewan and south-west of Manitoba.

Despite the low to medium thermal gradient within sedimentary basins, they are recognized as great sources of geothermal energy due to the vast accessible data regarding the basins' geological formations and temperature, which have been gathered through years of oil and gas industrial operations. The minimum required temperature for intermediate enthalpy thermal reservoirs for electricity production purposes was 80°C, which could be found at a minimum depth of 3 km within the WCSB (Grasby et al., 2012).

The Williston Basin is an epicratonic Phanerozoic basin with 800 km diameter covering south-west Manitoba (Osadetz et al., 2002). As a sedimentary basin, it develops low thermal gradients of 25-40°C/km. The studies on geological formation and lithology of Williston Basin showed the presence of halite, potassium salts and carbonate wedges within the Prairie Evaporite Formations (Bezys and McCabe, 1996, Nicolas and Barchyn, 2008). Halite is the mineral form (salt) of sodium chloride (NaCl) which decreases thermal resistance providing paths of heat transfer to the surface and has 2-3 times higher thermal conductivity comparing to other types of minerals (Kent and Christopher, 1994). Additionally, in contrast to most types of rocks, increase in temperature would increase the thermal conductivity of single crystalline halite as well (Abdulagatova et al., 2009). Considering the capabilities and thermal properties of the Williston Basin, the objective of this study is presented in the following section.

1.4 Objective

As a part of the WCSB, the Williston Basin demonstrates high geothermal potential within its halite formation. Halite is a suitable thermal reservoir due to low thermal resistance and higher thermal conductivity in comparison to other types of rock at the same depth, which decrease the length and time of drilling and increases the economic efficiency of the geothermal system. Besides the economic advantageous, less environmental impacts like carbon dioxide emission and groundwater contamination and the sustainability nature of geothermal resources improve the environmental efficiency of these systems.

Geothermal systems have been used in Manitoba for direct applications; however, electricity production within these systems is still untouched, and a comprehensive investigation regarding its electricity generation potential is appreciated. Therefore, the focus of this study is to determine the geothermal feasibility of halite as a thermal reservoir to provide adequate energy for electricity production in the Manitoban part of the Williston Basin using EGS.

In addition of the primary objective, the effect of depth on the thermal potential of halite is going to be investigated by developing a Generic model, which is a vertical extension of the primary model.

Chapter 2. Literature Review

Overview

The hot dry rock system of the Williston Basin leads to the use of an enhanced geothermal system for geothermal application with determination of its feasibility. Enhanced/engineered geothermal systems are defined as systems, where the aperture size of the existence fractures is increased by injection of high-pressure fluid, which consequently results in higher hydraulic conductivity of the reservoir. In this chapter, previous applications of EGS for sedimentary basins and temperature simulations are introduced. Then the importance of the saline formations as thermal reservoirs is explained, and difficulties in the process of simulation and real life application are discussed.

2.1 EGS application for HDR systems

Engineered or enhanced geothermal systems are the most efficient geothermal systems that do not require hot water in place or high permeable reservoir's rocks. EGS is applicable to regions with medium to low enthalpy e.g. northern territories of Canada, where the high price of electricity could be effectively decreased by the usage of any amount of geothermal energy (Majorowicz and Grasby, 2010).

Enhanced geothermal system is the main technology of producing energy from the hot subsurface rocks of the earth. The application of EGS has been expanded through recent decades by targeting the sedimentary basins as thermal reservoirs. Besides, the fractures patterns, density, and porosity of the hosting rock affect the development of EGS systems proportionally (Stober and Bucher, 2013). Within most HDRs, the fractures are filled with hot fluid that is mainly a saline brine which results in the injection of water with high pressure in order to increase the permeability of the host/reservoir rock (Stober and Bucher, 2013). The feasibility and productivity of EGS depend on various factors e.g. heat flow, fractures aperture, flow rate, fluid type, fluid pressure, and pumping duration.

In the 1980s, the feasibility of the EGS concept was evaluated for the first time by the ground backing of the "Fenton Hill" project. In this research, the well system was able to provide the constant temperature of 234°C at the depth of 3500 m for 11 months, using hydraulic stimulation as a heat exchanger (Duchane and Brown, 2002). Despite the high temperature production, this

case was economically inefficient due to a low flow rate and pumping pressure, which led to the partially opened fractures.

The Fenton Hill project provided information regarding the nature of fractures within the reservoir's formation. Based on this study, crystalline rocks' formations are mainly impermeable and mostly dry (no fluid). Natural fractures in crystalline rocks cannot provide adequate permeability for fluid circulation that was assumed to be impermeable. For the crystalline basins, the volume of the natural fractures was increased by injection of the high pressure fluid without the creation of any extra fractures. These expanded fractures were displaced due to the applied shear stresses, which conducted into the improvement of fractures average size and hydraulic conductivity. For the sedimentary basins, the hydraulic fracturing includes the creation of extra fractures along with the expansion of existence fractures (Pine and Batchelor, 1984, Stober and Bucher, 2013). The high pressure of the injection fluid is not only expanding the fractures aperture but is avoiding the fluid blowout within excavations as well for hydrothermal systems.

The production rate could be estimated by seismic techniques which are used to determine the reservoir growth and its approximate dimension (Grasby et al., 2012). In addition to the production rate, the fluid's type is critical in using EGS. An EGS includes a single or multiple sets of wells, which are targeting the thermal reservoir. At the production well, a considerable amount of hot water or steam is produced to provide adequate energy for power production at the power plant. Then the cooled fluid is re-injected into the reservoir at the injection well. The re-injection fluid has approximately constant temperature; however, its concentration could be varied due to the dissolution of the reservoir's rock into the fluid; thus, selection of the transfer fluid is significant in applying EGS.

Brown (2000) introduced carbon dioxide brine mixture as a transfer fluid instead of water for EGS for the first time at the Los Alamos National Laboratory, Fenton Hill. The feasibility of using any transfer fluid instead of water had been investigated, and the results demonstrated the positive consequences of using selected transfer fluid considering the reservoir chemical properties. Further investigations provided information regarding electricity production and efficiency of the EGS using mixtures of CO_2 and brine as transfer fluids (Mohan et al., 2013, Spycher and Pruess, 2010). In Mohan et al. (2013) research, the process of CO_2 sequestration was facilitated along with the geothermal energy production. Four fluids were used to simulate the Organic Rankine Cycle (ORC) performance. The most appropriate fluid, which developed the least environmental and greenhouse effect with the highest efficiency, was neopentane. This system was capable of producing 49 MWe and demonstrated an efficiency of 23%. Use of a second Rankine cycle improves the efficiency of the system for fluids at even lower temperatures. Therefore, the appropriate selection of transfer fluid would affect the efficiency and even the feasibility of EGS directly. In a case study from the North Eastern German Basin, water opted as the injection fluid for a saline basin. The extracted water after cooling must have been re-injected to the basin for circulation due to high salinity of the extracted water and for sustainability issues (Ondrak et al., 1998). However, the water was re-injected into the ground, but the environmental effect of reservoir dissolution is not negligible.

Due to high costs of EGS design, operation and tests, the best way to examine and design a geothermal plant is numerical modeling. The accuracy of numerical models depends on the available data and their accuracy. Following proposed some of the numerical models that had been developed for estimation and design of geothermal fields and plants.

2.2 Temperature and pressure simulation for EGS

2.2.1 **Temperature estimation of doublet well**

Determination of temperature within injection or production well is an effective procedure in designing the well system and the selection of a production fluid. Valberg (2005) determined the final derived temperature of a doublet EGS well using two steady state and one non-steady simulations. The outcome of his research proposed the similarity of the steady equation and non-steady model results. He proposed two case studies, considering one actual well at the Ormen Lange gas field (outside of the western parts of Norway) and one imaginary well with 4000 and 6000 m depth for each of the cases. Based on the simulation results, the higher flow rates lead to lower final derived temperature due to higher transfer velocity and shorter transportation time. Besides, the injection fluid with the constant temperature demonstrated larger temperature increase through the first simulation days. This temperature increase shortened after longer time periods which was the result of approaching the steady state. In contrast, at the production well, the final derived temperature was increased by time due to less heat loss along the well. One of the temperature drops caused the pressure drop at the production well, including the expansion of the fluid and lowering the hydrostatic pressure (Joule-Thompson cooling). Therefore, Valberg (2005) exposed the effect of flow rate and heat loss on the temperature and pressure of the transport fluid at short time periods (1 day) to longer periods (16 years).

2.2.2 **Temperature simulation in the North Eastern German Basin**

In a case study in the North Eastern German Basin (NEGB), a numerical model was established to determine the effect of various geothermal driving processes of an open loop system on

thermal structure and fluid system within the sedimentary basin. The main aim of Franco and Vaccaro (2014), was establishing a geologically consistent model of the NEGB considering the present temperature in full lithospheric scale. The interesting feature of their case study was the presence of rock salt at sedimentary deposits (Franco and Vaccaro, 2014).

A three-dimensional (3D) geologically consistent conceptual model with 13 sedimentary layers from the Lower Permian to the Cenozoic Strata was set up based on conduction energy equation at steady state from Fourier's Law. The layers classification is based on the information gathered through 40 years of hydrocarbon explorations which demonstrate the location and thicknesses of various rock types (Scheck and Bayer, 1999). For this case, Dirichlet condition as fixed temperature for the upper boundary and Neumann condition as heat flow for the bottom boundary conditions (BCs) were set. The main aim of this deep open loop system was to determine the derived temperature from deep formations. However, they did not demonstrate the presence of saline formations and specific effect of this low thermal resistant layer on the thermal gradient.

2.2.3 **Groß Schönebeck reservoir (Germany)**

Blöcher et al. (2010) worked on simulations of an EGS for a deep geothermal system in the Groß Schönebeck reservoir in north-east Germany. The geological formation of the region provided information regarding the reservoir's depth and formations. The reservoir is located 3-4 km beneath the sea level and six geological formations configured within the study area. The target layers for electricity production are two sandstone layers at 4 km depth.

A numerical model was set at FEFLOW (Diersch, 2002) and run for both steady state and transient condition. Based on the steady state, the initial condition of hydraulic head and temperature were obtained for dynamic model considering EGS wells operation. For steady state, the initial conditions were defined as the reservoir's temperature (137.5°C) and constant hydraulic head (-185 m) for the entire model. The constant temperature and heat flux were applied as upper and bottom BCs as well.

The temperature gradient derived from the steady state simulation was used as an initial condition for the transient model. The top boundary condition was removed, and a system of doublet well including one injection and one production well designed for this geothermal field with pumping rate of 75 m^3/h at 150°C and injection of the same rate but 70°C was assigned to the model. Artificial hydraulic fracturing through injection of high-pressure fluid enhanced the efficiency of the system. This method was used for increasing the efficiency of impermeable or low permeable rock formations by inducing fractures through high pressure pumping fluid (Stober and Bucher, 2013).

The model was run for 30 years, according to the life cycle of geothermal utilities. The results from FEFLOW simulations demonstrated the higher hydraulic head at the injection well within the reservoir that decreased on its path towards the production well. The final temperature derived from FEFLOW simulation showed approximately the same sequence as the study of the well doublet which was proposed at 2.2.1. The temperature in the fractures decreased after 30 years of operation by 25°C, and the final derived temperature was 150°C within the simulation time.

In Table 2.1, the similarities and differences between the Williston Basin case study and German case study at the Groß Schönebeck reservoir are presented. A comprehensive understanding of geothermal systems behavior as the effect of saline formations and working fluid on the final derived temperature is worth to be investigated.

Table 2.1. Similarities and differences between the Groß Schönebeck reservoir and Williston Basin case study.

Similarities	**Differences**
Modeling process	Hydrothermal vs. HDR
Initial and boundary condition identification	Sedimentary vs. Saline thermal reservoir
Assumptions made for transient state modeling and parametrization	Water vs. brine

2.2.4 **Saskatchewan geothermal studies**

A study at the University of Regina investigated the feasibility of geothermal water. In this study, a set of injection and production well at depths of 2,044 and 2,088 m were drilled through the sedimentary formations with high salinity (Jessop and Vigrass, 1989). To vanish the potential environmental hazards, the production water with a high salinity of 4-5 times of seawater, was reinjected to the target formations. The temperature at the target layers located at the Winnipeg Formation and the Deadwood Formation were 72-74°C. However, the achieved temperature was less than expected value of 80°C.

Based on Vigrass et al. (2007), a production of 100 m^3/hr at 60°C is possible considering 131 m drawdown after seven years. The lower depth formations were introduced in this research as possible shallower reservoirs, which could provide temperatures of 60°C or less.

The recent DEEP project focuses on an open loop geothermal system for electricity production at Saskatchewan part of the Williston Basin within a hot aquifer of 150 m thickness at 3 km depth (DEEP, 2014). The geothermal field is located in the south-east Saskatchewan with 5920 acres area. The electricity generation potential of this site was estimated as slightly over 50 MW in near future. DEEP project had been designed for 10 MW gross geothermal energy production with an expected output of 5 MW. Each 1 MW produced electricity, will remove 1200 houses from carbon based power system which is approximately equal to the omission of 5600 tons of carbon dioxide from the atmosphere each year (DEEP, 2014). There are similarities and differences between the DEEP project and this research, in DEEP project, the geothermal system is based on the extraction of brine from the reservoir (hydrothermal system); however, in this research, the EGS system was used. EGS is more accessible and environmentally friendly, due to its independence to the hot aquifer existence and selective production fluid.

2.3 EGS potential in Canada and Manitoba

EGS could be applied to regions with medium enthalpy where the temperature of 150 to 200°C could be achieved at depths of approximately 10 km. Majorowicz and Grasby (2010) proposed exponential functions (Eq.1 and Eq.2) of cost and depth for single and doublet well systems.

$$\text{Single well cost} = 3.23 \exp(0.2359\ z) \quad \text{Eq.1}$$

$$\text{Doublet well cost} = 7.81 \exp(0.22\ z) \quad \text{Eq.2}$$

Based on these equations, the cost of drilling a 5 km well is 1.65 times of a 3 km well. The maps of heat flow for depths of 3.5, 6.5, and 10 km within Canada were developed by Grasby et al. (2012). These maps demonstrated the high EGS potential for the sedimentary basins at middle and western territories of Canada. For deep formations where no measured data are available, an analytical method Eq.3 was established by (Lachenbruch, 1970). This equation is based on the geological and physical properties of the main four formations within Canada (Craton, Canadian Shield, Atlantic and Cordillera).

$$T_{(z)} = T_b + Q_r\ z\ \lambda^{-1} + A_0\ D^2\ \lambda^{-1}\ \left(1 - e^{(-z/D)}\right) \quad \text{Eq.3}$$

T_b is the temperature of crystalline basement surface (°C), Q_r the reduced (deep) heat flow (W/m^2), z is the depth (m), λ thermal conductivity (W/mK), A_0 is the surface heat generation of the crystalline basement ($\mu W/m^3$), D is the slope of the empirical/statistically derived heat flow Q vs. heat generation and relation A_0 (km).

The Western Canadian Sedimentary Basin provides the appropriate heat flow for EGS application and electricity production. In south-west Manitoba, within the Williston Basin, large halite deposits with potash inter-beds and a minor amount of anhydrite were found (Chapter 4). As it was mentioned in section 1.30, the saline formations provide paths of lower thermal resistance that would lead to a higher temperature at lower depth. The cost of drilling increased exponentially by depth; thus, shortening the drilling length would increase the efficiency of EGS

incrementally (Grasby et al., 2012). The heat flow within this region was estimated at 70-90 mW/m^2 that equals to a thermal gradient of 30°C/km.

2.4 Saline formations as thermal reservoir

The management and development of thermal reservoir require exact estimation of reservoir behavior which could be only achieved by investigations regarding rock properties and structural features (Chen et al., 2015). As it was mentioned at introduction (1.3), saline formations provide paths of lower thermal resistance and develop high thermal conductivities (2-3 times more than other rock types) that enhance the thermal efficiency of saline formations as geothermal reservoirs. The temperature of the sediments surrounding the saline formations is higher than the sediments far from the salts apexes (Petersen and Lerche, 1995). Hence, the saline formations are potential to be considered as a thermal reservoir.

A disadvantage about saline reservoirs is the high solubility of the formations with water, as the most common transfer fluid, and its environmental impacts. Plummer et al. (1988) presented a computer program for calculation of geochemical reactions in various brines. The saturation index is the representation of the mineral status e.g. SI of zero means the equilibrium condition achieved and the mineral is totally saturated, negative SI is the under saturated and positive SI values demonstrating the supersaturated condition. Based on Plummer et al. (1988), for halite, $MgCl_2$ has the smoothest slope of SI variation with temperature comparing to carnallite, kainite, sylvite, brucite, and bischofite. Based on his study, within 90°C temperature difference, the SI varied between -0.5 to +0.5.

In addition, of the reservoir solubility, the minerals precipitation must be studied as well. The extracted fluid with high pressure and the temperature is under saturated condition, after losing the absorbed temperature and pressure at the surface, the cooled low pressure brine is reinjected to the reservoir as super saturated brine which results in precipitation of its minerals (Petersen and Lerche, 1995).

Therefore, saline formations are introduced as great geothermal resources with considerations regarding the selection of the production fluid type. In this research, the capability of energy production and fluid and heat transfer from the saline formation will be reviewed. Further investigations, to opt the most efficient fluid are recommended for future studies.

Chapter 3. Methods

Overview

This chapter introduces the methods to locate the most appropriate geothermal field in the Williston Basin. The geology and morphology of the Williston Basin from late Paleozoic formation to the surface formation are investigated to demonstrate the sequence of sediments and rock formations. The specific physical properties of the Manitoban part of the basin are determined using Geographic Information System (GIS) maps. Following the geological characterization, the applied methods to determine the generic temperature data set and hydraulic and thermal properties of the selected site at the ambient condition and by considering the effect of pressure and temperature are explained. Then the governing equations for heat and fluid transfer along the wells and reservoir are proposed. In the last section of this chapter, the principals of numerical modeling with FEFLOW and the defined mesh systems, thermal and hydraulic initial and boundary conditions are introduced.

3.1 Study area

A geothermal potential was recognized within the Williston Basin in the south-west of Manitoba (Nicolas and Barchyn, 2008). As it was mentioned in the introduction, the geothermal potential of any specific region depends on its geological formation and thermal gradient. In this section, the potential of the Williston Basin as a geothermal field was evaluated based on previous studies and history of the basin's heat flow.

3.1.1 **Geology and lithology of the Williston Basin**

Kent and Christopher (1994) exposed the subsidence and geographical positioning of formations as the primary origins of the Williston Basin creation. Subsidence occurred due to the initial erosion of lithospheric layers, thinning rock layers, densification of metamorphic rocks and excess horizontal stress. Initial erosion of the lithospheric layer was determined as the primary cause of the subsidence. Through this purely thermal process, heated uplifted layer contracted within the cooling period which resulted in subsidence of the lithospheric layer (Kent and Christopher, 1994). The positioning of the formations developed the composition of the Williston Basin's basement (Meek, 1958).

The basement was categorized into three structural compositions as Archean in the east, Wyoming and Churchill in the west and collision zone of the lower Proterozoic as a separator between east and west (Kent and Christopher, 1994). In each section, various structural features and geographical positioning occurred due to different periodic activities, especially in the Cambrian, Mississippian and Jurassic-Cretaceous of the Phanerozoic eon.

Six high stratigraphic reliefs and various ages within the Basin's formation based on the early Paleozoic events in the Williston Basin have been introduced in literature (Osadetz et al., 2002, Kent and Christopher, 1994).

The first temporal interval in the issued sequence is the Middle Cambrian to Upper Ordovician Sauk, in which the first sedimentation records were investigated due to cycles of contraction and expansion. Sandstone and shell comprise the principal formation of this interval which has been determined as the first reflection of the Williston Basin by the curvature of their isopach (Kent and Christopher, 1994).

Following the Cambrian interval, Ordovician and Silurian, Middle Devonian-Mississippian, Triassic- Jurassic and Jurassic to Cretaceous and Quaternary comprise the other five sequences of the Williston Basin (Osadetz et al., 2002). Each of these sequences developed individual geological formations that resulted in identical thermal behaviour. For example, the Devonian-Mississippian interval rock formation includes halite, potassium salts and carbonates wedges as its main components. Based on the introduction, halite provides lower paths of resistance and has 2-3 times higher thermal conductivity which would increase heat flow which is one of the primary criteria of geothermal field identification as mentioned in the introduction.

Bezys and McCabe (1996) studied the formations of the Williston Basin within Manitoba. In their studies, a range of thicknesses and possible components of each formation were proposed along with regional and geological maps from Middle to the Lower Paleozoic era. Ordovician strata had been divided into three sub formations, Lower and Upper units of Ordovician, Red River Bed and Stony Mountain. The Lower Ordovician consists mainly of shale in the south and changes to sandstone in the northern area. The Upper Ordovician contains impermeable

anhydrite. This impermeable bed along with Gunn Shale of the Red River strata affected later dolomitization and evaporate solutions. The Red River Bed thickness is varying from 170 m in the south to 40 m in the north. The southern section comprises mainly of dolomitic limestone, which transforms into dolomite in the northern parts. The Stony Mountain formation is mainly constant and provides shale formations. Silurian carbonates have the approximately same thickness and lithology within the Williston Basin, which comprises the tectonic stability of this stratum. The main component of this formation is dolomite, surrounded by argillaceous sand. Devonian strata have the highest significance in this study due to the presence of halite within its Prairie Evaporite Formation in the Elk Point group. The Dawson Bay formation, which comprises of four units, is one of the most significant formations within this period. Unit 1 is the lowest unit containing highly oxidized dolomite and grey-green silty shale while unit 4 is the upper unit containing siltstone, dolomite, and dolomitic siltstone. The oxidization percentage decreases from unit 1 to unit 4 and the potential of reservoir performance increases (Karasinski, 2006). The Devonian formation had been underlying by collapsed evaporates (mainly halite) of the Prairie Evaporite within the Elk Point time. The estimation of the salt thickness was challenging due to a cover of the Devonian reef, underlies about 60-100 m of salt within the western sections of the Williston Basin in Manitoba and Saskatchewan (covering southern Manitoba to Lake Manitoba). The Prairie Evaporite had been dissolved from the entire surface and large area of the subsurface, following the burial of Dawson Bay. The salt solution commenced from the late Paleozoic to Mesozoic period. The brine outflow of numerous salt springs along Devonian outcrop belt shown the continuity of salt decomposition (Bezys and McCabe, 1996). Multiple horizontal zones due to salt collapse (with various causes) complicated

the configuration of the salt thicknesses. Thus, Bezys and McCabe, considering the dominant salt and potash inter-beds and some minor anhydrite, have suggested the thickness up to 128 m for this formation.

The Target Geoscience Investigation (TGI) project investigated the architecture and hydrocarbon potential in the Williston Basin. The study area of this project is given in Fig. 3.1. This region contains the Williston Basin and the WCSB which is located between Lake Winnipeg until the Saskatchewan border east-west and is restricted by US border in the south (coordinates: 49°- 96° N and 49°-101.4° W).

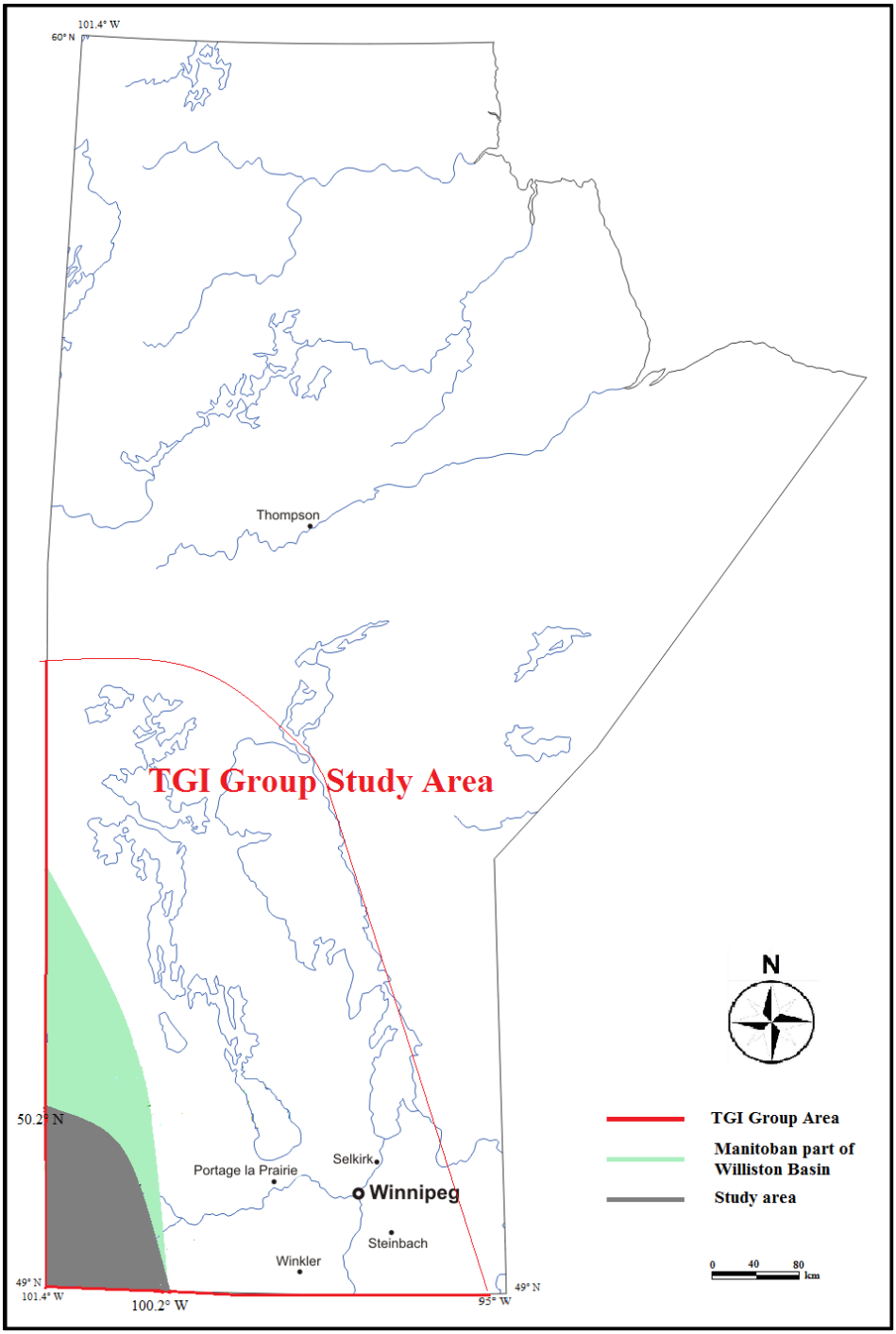

Fig. 3.1. Study area of the TGI project (within red border) and Manitoban part of the Williston Basin (green area)

The result of the TGI project provided essential data regarding structural and isopach maps, hydrocarbon maps, the hydraulic regime and hydrogeology considerations. The data provided from the TGI project was used to create shapefiles within ArcGIS 10.1 (McCoy et al., 2001) to discover the thickness of all formations that compose the basin. These shapefiles were converted to raster maps in order to allow the use of geostatistical methods, which is ordinary kriging in this study. The ordinary kriging assumes that the distance or direction between sample points are reflecting a spatial correlation that can be used to explain variations in the surface. Detailed information on the kriging method can be found in Royle et al. (1981). The tool Kriging of ArcGIS 10.1 fits a mathematical function to a specified number of points, or all points within a specified radius, to determine the thickness for each location (Law and Collins, 2013).

Eq.4 demonstrates the kriging formula, where $\hat{Z}$ is the measured value of the *i*th location, ω is the unknown weight for the *i*th location, S_0 the prediction location and N the number of measured values.

$$\hat{Z}_{(S_0)} = \sum_{i=1}^{N} \omega_i \, \hat{Z}_{(S_i)} \qquad \text{Eq.4}$$

The thickness of each layer (ΔA) was found using the tool Raster Math of ArcGIS 10.1 in which the distance between the formation of interest ($\dot{A}_n$) and the formation located below the formation of interest ($\dot{A}_{n-1}$) will result in the thickness of the formation.

$$\Delta A = \dot{A}_n - \dot{A}_{n-1} \qquad \text{Eq.5}$$

Finally, the maps were clipped to exclude territories that were not in the remaining context of the Manitoba surface and classified into subsections to visualize the thickness of the layers on an adequate scale (Amaral, 2014).

TGI data contain 44 geological formations from the surface to the Precambrian formation, which is located at the bottom of the sedimentary deposits in the Williston Basin within Manitoba and Saskatchewan (Table 3.1). These formations contain six main geological periods and some subsections to establish a comprehensive demonstration of depth and thicknesses of the formations. For simplification, only subsections of the Devonian period were considered during the map development. GeoCando (Feigie et al., 2008), which is a computer program to allow for 3-dimensional visualization of geodata and geomodels, was used to generate final maps of formations' thicknesses. Input data of this analysis were the processed ArcGIS data based on the TGI group preliminary data sets (Nicolas and Barchyn, 2008). Fig. 3.2 shows the plan view of the study area based on processed data.

Table 3.1. Sequences of geological periods and formations used to generate thickness maps of the Williston Basin within Manitoba and Saskatchewan

Era	Period	Formation
Cenozoic	Quaternary	Glacial draft Turtle Mountain
Mesozoic	Cretaceous	Belly River Manville
	Jurassic	Amaranth
Paleozoic	Mississippian	Lodge Pole Bakken
	Devonian	Torquay Birdbear Duperow Souris River Dawson Bay Prairie Evaporate Winnipegosis Ashern
	Silurian	Interlake
	Ordovician	Stonewall Stony Mountain Red River Winnipeg
Precambrian		

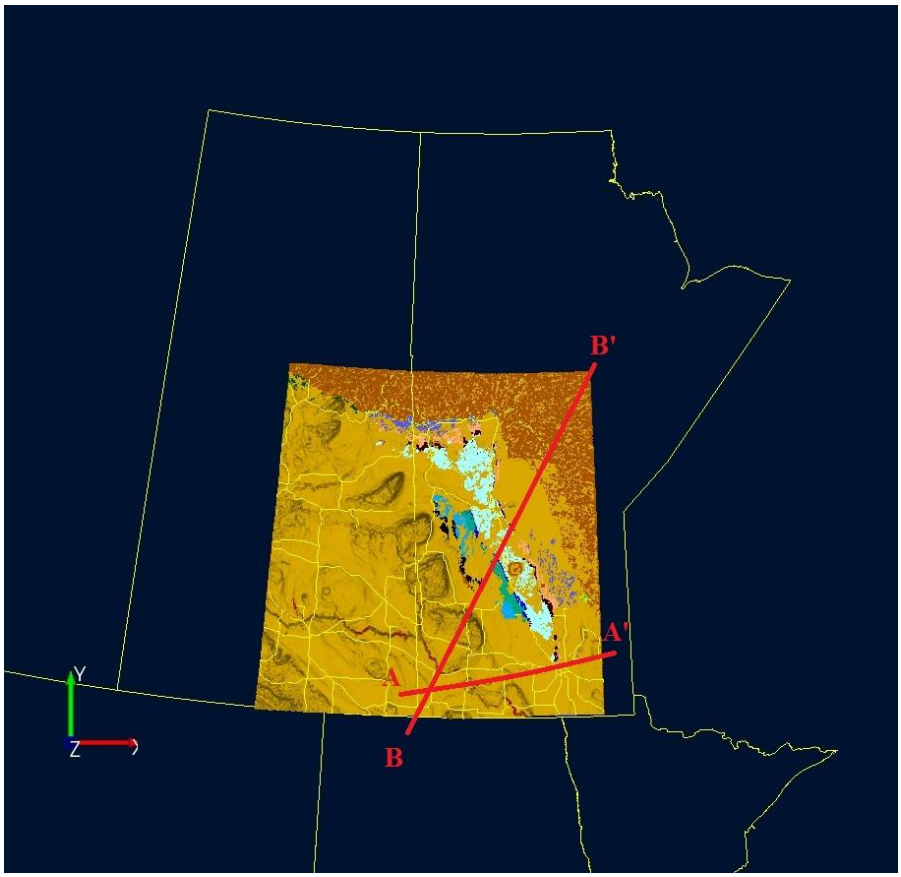

Fig. 3.2. Plan view of the study area considered by the TGI group showing the top view (surface formation) and two locations of cross sections A-A' and B-B'.

Cross sections A-A' and B-B' were used to identify each formation's location, depth, and thickness. Fig. 3.3 and Fig. 3.4 show the 3-dimensional and 2-dimensional views of the cross sections A-A' and B-B'. The depths of the formations are increasing from north to south and east to west. Higher temperatures can be found at deeper elevations; in this case study, the deepest elevations were at the most south-west region of the study area. Therefore, these locations are expected to have a high potential for geothermal applications specifically considering the saline components within the Devonian period.

a) b)

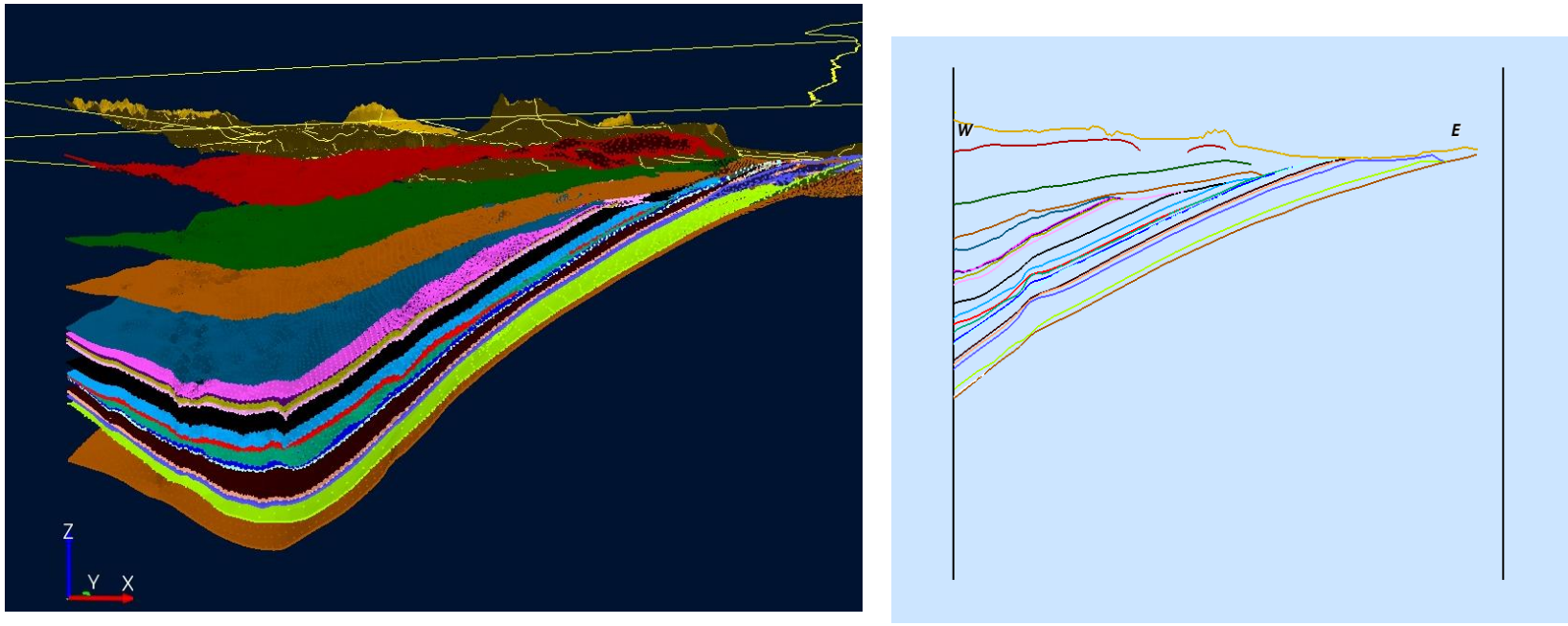

Fig. 3.3. (a) 3-dimensional (3D) view of the Williston Basin along cross section A-A', all the layers and formations are based on data presented in Table 3.1. (b) 2-dimensional (2D) view of cross section A-A’ demonstrates the deepening of the formations from east to west.

a) b)

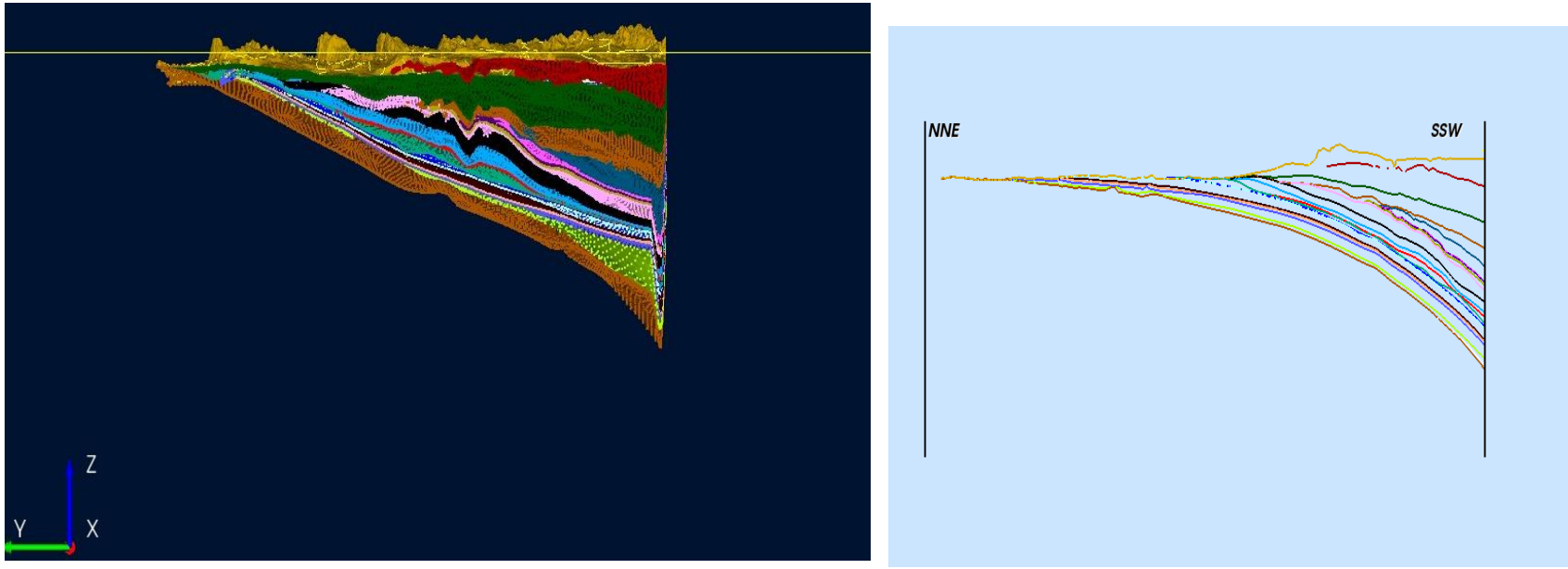

Fig. 3.4. 3D view of study area along the cross section B-B', all the layers and formations are based on data presented in Table 3.1.

(b) 2D view of cross section B-B’ demonstrates the deepening of the formations from north-north-east to south-south-west.

3.1.2 **Thermic**

Temperature data

Drilling log reports from gas and oil companies are the main sources of actual temperature measurements within most of the sedimentary basins. However, in most drilling operations, the temperature had not been recorded along the borehole and only the maximum temperature of the bottom hole was archived. Additionally, the longest drilling operation with recorded temperature attributed to the depth of 1200 m and no further data was found for deeper formations.

Therefore, a generic temperature data set was prepared as a combination of accessible temperature data from various wells at different locations for lower formations and the calculated values from the analytical method (Eq.3) for the formations with more than 1200 m depth.

The borehole logs and temperature resources are from Government of Manitoba gas and petroleum website and TGI group project data (Government of Manitoba and Manitoba Mineral Resources, 2014, Nicolas and Barchyn, 2008). For the analytical method, Grasby et al. (2012) showed D, Q_r, A_0 and λ parameters for the four main geological formations of Canada which are presented in Appendix (a). Between the four major formations, Craton was opted which covered the middle territories of Canada. Then, by having the constant Q_r and D, different λ and A_0 were used to estimate the temperature with analytical method. The selected parameters led to the minimum error between the measured and calculated data within the lower depths. These parameters were further used to calculate the temperature of the deeper formations.

Thermal Gradient

As a sedimentary basin, the Williston Basin provides a thermal gradient of 25-40°C/km within its formation (Grasby et al., 2012). The temperature of the Williston Basin's basement surface is increasing from the north-east to south-west align with increasing the Paleozoic succession thickness. Basement temperatures for out rising regions, which are in contact with the surface's cold temperature, are around 5°C, which gets to the highest point of 100°C for regions with 3.5 km thicknesses. This demonstrates the relatively low temperature of less than 70°C for most of the basement's surface within the depth of less than 2.4 km (Osadetz et al., 2002).

Thermal gradient and heat transfer within rock formations depend on the lithology, the thermal and hydraulic properties, and the heat transfer mechanisms. Rock properties including porosity, thermal conductivity, thermal diffusivity, specific heat capacity, and specific heat storage as a function of pressure and temperature were investigated considering the formations of the proposed geothermal field.

The heat transfer mechanisms are known as advection, conduction, and radiation. Radiation only affects the surficial soils' temperature, which is influential for shallow systems operations, but has a minor effect on the subsurface soil's heat absorption. Therefore, it was neglected in the simulation of heat transport within deep formations. Advection and conduction are the main heat transport mechanisms for sedimentary basins. Advection is based on water circulation through the permeable aquifers and absence of water within most of the sedimentary rocks, led to having conduction as the main heat transfer mechanism (Cacace et al., 2010). Conduction is an internal energy, which transfers by microscopic diffusion and collisions of particles due to a temperature gradient. The calculation of the transferred heat is based on Fourier law (Eq.6), which is a 3-

dimensional time-dependent formula and can be applied in rectangular, cylindrical or spherical coordinate systems.

$$\frac{\partial T}{\partial t} - \alpha \nabla^2 T = 0 \qquad \text{Eq.6}$$

Eq.6 is the general expression of heat transfer where α (m^2/s) is the thermal diffusivity which is a function of thermal conductivity, pressure, thermal capacity and density and T (°C) is temperature difference as a function of time and space. Based on the type of reservoir and conditions within the geothermal field, Eq.6 was used for a rectangular system.

Thermal conductivity

Thermal conductivity is the ability of rocks to conduct heat through their formations. The thermal conductivity of the rock formations has a critical impact on the thermal gradient and efficiency of a geothermal system. Higher thermal conductivity leads to lower resistance and less temperature loss. The thermal conductivity is a function of rock type, pressure, and temperature. The thermal conductivity of each formation based on their most common composition was determined at ambient condition based on previous studies (Grasby et al., 2012, Jessop, 1990). Then, the effective thermal conductivities as the function of pressure and temperature were calculated. Table 3.2 demonstrates the effective thermal conductivities of typical sedimentary rocks for various ranges of temperature and pressure. For dolomite, thermal conductivity would not change as the effect of temperature within the specified range; however, by increasing the pressure, thermal conductivity would increase linearly in the beginning and then passes to saturation in the regression of pressure P = 80 MPa. A general equation for sedimentary rocks

within a temperature range of 0-300°C was introduced as well to consider the effect of temperature on thermal conductivity of other types of sedimentary rocks.

Table 3.2. Effective thermal conductivity of various rock types considering temperature and pressure variation.

Rock Type	Temperature Range, T (K)	Pressure Range, P(MPa)	Effect Of Temperature	Effect Of Pressure	Reference
Siltstone	275-523	0-250	$\lambda(T,P) = C(P)T^{n(P)}$ [1]		(Ramazanova and Emirov, 2012b)
Sandstone	273-523	01-400	$\lambda(T,P) = C(P)T^{n(P)}$ [2]		(Ramazanova and Emirov, 2012a)
Dolomite	275-523	0-250	No impact	$\begin{cases} \lambda = 0.02P + 3.14 \ \ Linear \\ \lambda = 3.243P^{0.0677} \ Regression \end{cases}$	(Ramazanova and Emirov, 2012b)
Salt	0-353	-------	λ (T)= a_0+a_1(T) [3]	-------	(Eppelbaum et al., 2014)
Limestone	0-1073	0-70	$\lambda(T) = A + \frac{B}{350+T}$ [4]	$\lambda(P) = \lambda\,(1 + b * P)$ b=319e4 1/MPa	(Arora et al., 2011, Robertson, 1988)
Shale	0-318	0-70	-------	$\lambda(P) = \lambda\,(1 + b * P)$ b=145e4 1/MPa	(Robertson, 1988)
General equation for sedimentary rocks	0-573	-------	$\lambda(T) = \frac{\lambda(0)}{0.99+T(a-\frac{b}{\lambda(0)})}$ [5]	-------	(Vosteen and Schellschmidt, 2003)

[1,2] C = 0.14 W/mK^2 and n = 0.47 under normal conditions (Ramazanova and Emirov, 2012b).

P (MPa)	0.1	50	100	150	200	250	300	350	400
n (Sandstone)	0.47	0.22	0.13	0.12	0.12	0.11	0.47		
n (Siltstone)	–0.28	–0.23	–0.20	–0.20	–0.20	–0.19	–0.19	–0.19	–0.19

[3] λ is the thermal conductivity at ambient temperature and a_0 and a_1 are the constant values of the experiment.

	a_0 (m °C/W)	$a_1 \times 10^{-4}$(m/W)
Salt	0.1605	7.955

[4] A and B for limestone at proposed temperature are equal to 0.13 W/mK^2 and 1073 W/m respectively.

[5] $(T) = 0.54\lambda(25) + \frac{1}{2} * \sqrt{1.16(\lambda(25))^2 - 0.39\lambda(25)}$, a = 0.0034$\pm$0.0006 and b = 0.0039$\pm$0.0014.

Specific heat capacity of solids

Specific heat capacity is the ratio of heat capacity to unit mass ($c = \frac{Q}{M\Delta T}$). Heat can be stored and transferred as sensible heat or heat required by phase change. The required energy would be a function of f (degree of freedom), Avogadro's number (N_a=6.0221409× 10^{23} 1/mol) and Boltzmann constant (b=1.38064852 × 10^{-23} J/K) (Eq.7). For solids, f = 6 attributed to the three degrees of freedom for potential and kinetic lattice vibration energy in three dimensions.

$$Q = \left(\frac{M}{m}\right)\left(\frac{f}{2}\right) b\,\Delta T = \frac{f}{2}\, b\, N_a \Delta T \qquad \text{Eq.7}$$

Specified heat capacity of substances would be equal to the heat capacity divided by mass (M). This property is directly influenced by temperature, pressure, porosity, and saturation. Various statistical and steady state and transient calorimetric methods were introduced by researchers to investigate the most accurate value of effective specific heat capacity (Arora et al., 2011).

Eq.8 is a statistical approach to determine the effective specific heat capacity of various rock types and minerals considering temperature variation and its compatibility to be rescaled (Waples and Waples, 2004). In this equation, the temperature effect is estimated by the application of the normalized specific heat capacity ($c_{p,n}(T)$)

$$c_{p,n}(T) = 0.716 + 1.72 \times 10^{-3}T - 2.13 \times 10^{-6}T^2 + 8.95 \times 10^{-10}T^3 \qquad \text{Eq.8}$$

Eq.8 is adaptable to all kinds of minerals and nonporous rocks at any temperature. Eq.9 demonstrates the value of specific heat capacity at a temperature T_2 by having the value of specific heat capacity at T_1.

$$c(T_2) = c(T_1)\frac{c_{p,n}(T_2)}{c_{p,n}(T_1)} \quad \text{Eq.9}$$

In this study, $c\,(T_1)$ was assumed to be the specific heat capacity at ambient condition and T_2 represented the temperature of each formation based on temperature data. The unit of specific heat capacity for this equation is cal/g°C that further was transformed into J/kg K.

Specific heat capacity of a brine

The transfer fluid for EGS was selected as a brine of 6% NaCl due to its higher volumetric heat capacity comparing to water. The specific heat capacity of brine of as the selected transfer fluid does not demonstrate significant variation due to temperature increase. The effective specific heat capacity for brine was calculated based on Fasina et al. (2002) at the proposed temperature of the target formation (halite of the Prairie Evaporite).

Volumetric heat capacity of solids

Volumetric heat capacity (VHC) or thermal capacity is the ratio of heat capacity to the unit volume instead of mass ($J/m^3°C$). This parameter could be representing as the product of density and specific heat capacity or thermal conductivity and diffusivity. In this research, the volumetric heat capacity was estimated as the product of effective specific heat capacity and density Eq.10.

$$VHC = \rho c = \lambda/\alpha \quad \text{Eq.10}$$

The thermal volumetric expansion coefficient of rocks and minerals are considerably very small (~ 10^{-5} 1/K) which leads to a minuscule variation of density with temperature. Thus, the effect of temperature on density could be readily ignored (Eppelbaum et al., 2014).

Note: diffusivity is another important parameter in modeling the heat transfer and geothermal systems that equal the ratio of thermal conductivity to volumetric heat capacity.

Expansion and compression of a brine

The thermal properties of the production fluid in response to the pressure and temperature were determined at the maximum applied temperature and pressure (reservoir's location) by estimation of the expansion and compression coefficients. Eq.11 and Eq.12 are representing the volume thermal expansion (γ) and compressibility (β) of any fluid as the function of pressure and temperature (Eppelbaum et al., 2014).

$$\gamma = \frac{\left(\frac{\partial V}{\partial T}\right)_p}{V_0} \qquad \text{Eq.11}$$

$$\beta = \frac{(\frac{\partial V}{\partial T})_T}{V_0} \qquad \text{Eq.12}$$

The density, thermal expansion and coefficient of the brine NaCl 6% (production fluid) were derived at the temperature equal to the target formation's temperature based on Engineered Solution Guide report of Tetra Technologies (2014) charts.

Porosity

Porosity is a fraction of void space (V_v) to the total volume (V_T) ($\varphi = \frac{V_v}{V_T}$.). Void space attributes to air and liquid phases at unsaturated condition; and liquid phase for saturated medium. The porosity of various rock formations was estimated based on the literature review at ambient condition (Grasby et al., 2012).

By evaluation of the expansion and compression factors of saturated rocks, the effective porosity was estimated. The expansion factor of the solid phase is considerably low and due to increasing compression (by enhancing the pressure) and resistance force against volume expansion from surrounding rocks, rock formation would not encounter volume changes as the effect of pressure and temperature. Hence, the liquid phase has the only impact on porosity (Eppelbaum et al., 2014).

Due to negligible effect of expansion on volume of the solids' phase, the effective porosity was estimated as the function of fluid's expansion. Eppelbaum et al. (2014) provided graphs of volume change versus temperature and pressure for water which follows an approximately linear function. Although the production fluid was opted as brine NaCl 6%, due to similar density and thermal conductivity, the water volume expansion was used for the production fluid.

3.1.3 **Hydraulics**

Hydraulic head

In a study from Palombi (2008), 19 aquifers and 13 aquitards were identified across the Manitoban and Saskatchewan parts of the Williston Basin. Chemical dissolution and properties

of flow within this region conducted into four hydrochemical categories. Vertical and horizontal flows were distinguished within the basin, and the hydraulic pressure of each formation was provided individually.

The pressure sampling at various locations (Palombi, 2008) and comprehensive maps with detailed information on the bedrock topography and Manitoba's geology (Klassen et al., 1970) were used to estimate the hydraulic head based on Eq.13.

$$h_h = h_p + Z \qquad \text{Eq.13}$$

h_h represents the hydraulic head (m), h_p pressure head (m) and Z the elevation of groundwater from the specific datum (m).

The hydraulic head considering the hydrostatic head at each depth and pressure depth would be equal to -10 m by having datum at the surface and minus Z direction from top to bottom of the formations for steady and transient models within Williston Basin.

Hydraulic fracturing

Hydraulic fracturing is the technique to develop new and to increase available fractures and thus the conductivity of the reservoir rock by injecting high-pressure fluid. The high-pressure fluid would extend the fractures of thermal reservoir towards the highest stress directions. For deep wells (more than 600 m depth), the largest stress is attributed to the vertical direction, and the maximum horizontal stress is aligned with the fluid direction from injection to the production well. Therefore, fractures must have an empirical shape with the highest porous volumes at injection and production wells' bottom holes which gradually decreasing by flow pressure reduction (Fisher and Warpinski, 2012). The constant increase in the pressure enhanced the

porous volumes around the wells bottom holes which created more fractures and kept the previous fractures open. The effect of fracturing on hydraulic conductivity can be estimated using Dehkordi et al. (2014) assumptions on fractures' openness, connections, and frequency. Table 3.3 is the categorization of the fractures considering their openness. Most of the fractures assumes to be of the very tight category for this research with the openness of less than 0.1 mm. For laminar fluid flows, Hagen-Poiseuille equation (Eq.14) is used to estimate the flow rate Q (m^3/day) in a cylindrical tube (well) as a function of the head drop along the well's axis (m). The effect of fractures on the fluid flow was derived based on Eq.15 by assuming the laminar flow between two parallel surfaces.

$$Q = \frac{\pi r^4}{8\mu L}\Delta P \qquad \text{Eq.14}$$

$$Q = \frac{\rho g}{12\mu L} s^3 \dot{h} \Delta P \qquad \text{Eq.15}$$

Where Q is the flow rate (m^3/day), ΔP is the pressure drop (MPa), L is the fluid's path (m), r is the well radius (m), ρ is the density (kg/m^3), g the gravitational constant (m/s^2), ν the kinematic viscosity of the fluid (m^2/s), s the fracture width (m) and the $\dot{h}$ fractures' height (m).

Considering Eq.14 and Eq.15 and the significance of apertures on hydraulic conductivity is more than the hydraulic gradient, the hydraulic conductivity of the fracture (K_{fr}) would be as following (Dehkordi et al., 2015):

$$K_{fr} = \frac{\rho g}{12\mu} s^2 \qquad \text{Eq.16}$$

There is limited information regarding fractures geometry. Bruno and Nakagawa (1991) determined the impact of pore pressure on rock fractures in sedimentary rocks. Based on their theoretical analysis and experimental results, the fractures orientation is a function of pore pressure magnitude at the local scale and pore pressure gradient at a global scale. The fractures were distributing as spherical shapes with higher magnitude at the highest pore water pressure sources (wells' location). The fractures' volumes were decreased by reduction of pore water pressure.

Table 3.3. Fractures classification based on aperture size (Dehkordi et al., 2014, Lim et al., 2007, Barton, 1973).

Category	Aperture (mm)
Non-Permeable	0
very tight	<0.1
tight	0.1-0.25
Partly open	0.25-0.5
Open	0.5-2.5
Moderately wide	2.5-10.0
Wide	>10.0

3.1.4 **Pressure data**

The solid pressure and fluid pressure affect the thermal properties of rock formations and the fractures efficiency directly. The solid phase pressure was estimated as total stress, the accumulative weight of formations from top to the bottom of the model, which affect the effective thermal properties of each formation. The pressure within each formation is a function of depth and density of the above formations. For each depth, the total vertical stress (weight) of above formations was considered as the pressure on the formation. Palombi (2008) proposed the hydrostatic pressure of various locations in the Williston Basin within Manitoba and

Saskatchewan. He estimated the hydrostatic pressure for various rock blocks within the Basin. For Manitoban section, a linear gradient between depth and hydrostatic pressure represented the hydrostatic pressure from 400 to 1600 m depth. For south parts of the basin, the hydrostatic pressure was estimated as approximately 16 MPa at a depth of 1600 m.

Densities of formations were presented at Applied Geothermic by (Eppelbaum et al., 2014) and were presented in Appendix (f). The pressure at the bottom of each layer was estimated as the density of the main component multiply by the thickness of the layer.

The fluid's pressure is the function of hydraulic head that was constant in the steady state model and variable at transient due to wells' operation that is going to be explained in section 3.4.3. The hydraulic head drop and rise, as the function of wells operation, is the fluid phase pressure which affects the final derived temperature of the extracted fluid and efficiency of the system.

The hydraulic head calculations have been completely described in section 3.1.3, and the pressure drop/ rise was calculated based on Harrison et al. (2013) considering a doublet well. In the transient state model, the total pressure drop in the production well was estimated considering the surface overpressure (ΔP_0), static formation pressure (P_{op}), frictional pressure (ΔP_{fp}), and dynamic pressure (ΔP_{dp}). The effect of well interface pressure (ΔP_{ip}) came into consideration if multiple productions were designed for the field and the skin effect was neglected for simplicity.

Appendix (b), Eq.37, Eq.38, Eq.39, and Eq.40 show the frictional pressure and dynamic pressure calculations for the production and the injection wells.

3.2 Governing equations for heat transfer

The principal of EGS is based on the fluids circulation along the wells and through the reservoir from the injection to the extraction point. The injected fluid absorbs heat on its path from the injection point at the surface to the filter screen at the bottom of the production well. The heated fluid provides energy for electricity production at turbines. The heat transfer of the soil and fluid phase were estimated by continuum laws of mass, momentum, energy and entropy at the macroscopic level within the reservoir and along the wellbores (Diersch, 2013). For HDR systems due to the absence of fluid phase, the key transfer process is conduction through the solid phase at the beginning of the system's operation, and the only fluid phase of the system is attributed to the production fluid.

Reservoir heat transfer:

For a saturated non-deforming media at the macroscopic level, the heat flow can be calculated using Fourier law and Eq.17 considering constant density and viscosity for the reservoir (as solid phase).

$$\frac{\partial}{\partial t}[(1-\varphi)\rho_s c_s T_s] - (1-\varphi)(\lambda_s \nabla T_s) = 0 \qquad \text{Eq.17}$$

The heat transfer of the fluid phase can be described by Eq.18.

$$\frac{\partial}{\partial t}[\varphi \rho_f c_f T_f] + \nabla(\rho_f c_f T_f q) - \varphi \nabla(\lambda_f \nabla T_f) = 0 \qquad \text{Eq.18}$$

Where, s indicates the solid phase and f the fluid phase; so, T_s and T_f are the temperature of the solid and fluid phase (K), φ is the porosity (-), ρ is the mass density (kg/m^3), c is the specific heat capacity (J/kgK), and λ is thermal conductivity (W/mK) (Saeid et al., 2013). Note that for liquid phase the density and viscosity were changing. Density of a liquid was a function of pressure and temperature (3.1.2).

By defining a local volume average for thermal conductivity and volumetric heat capacity considering the thermal equilibrium and energy balance law for porous media, the heat transfer equation was proposed as Eq.19:

$$\frac{\partial}{\partial t}[\rho cT] + \nabla.(\rho_f c_f Tq) - \varphi\nabla(\lambda\nabla T) = 0 \qquad \text{Eq.19}$$

Wellbore heat transfer:

Wellbore heat transfer is a conductive-convective process; however, in this study, the heat transferring between fluid and pipe material (casing) and pipe materials and surrounding soil were neglected, and only the fluid and soil heat transfer has been considered in order to minimize the heat loss and simplify the calculations. The indices "i" and "p" indicate injection and production well representations. Eq.20 and Eq.21 are governing equations for heat transfer of the production fluid at the injection and the production wells (Saeid et al., 2013):

$$\rho_f c_f \frac{\partial T_i}{\partial t} dv_i - \lambda_f \frac{\partial^2 T_i}{\partial z^2} dv_i + \rho_f c_f u_i \frac{\partial T_i}{\partial z} = 0 \qquad \text{Eq.20}$$

$$\rho_f c_f \frac{\partial T_p}{\partial t} dv_p - \lambda_f \frac{\partial^2 T_p}{\partial z^2} dv_p - \rho_f c_f u_p \frac{\partial T_p}{\partial z} = 0 \qquad \text{Eq.21}$$

In the above equations, ρ_f and ρ_s are the fluid and solid densities (kg/ m^3), λ_f is the fluid's thermal conductivity (Wm/K), T_i and T_p related temperature of the injection and production fluid (°C), ν_i and ν_p kinematic viscosity of the injected and pumped fluid(m^2/s), c_f the specific heat capacity (J/mK), and u_i and u_p the average fluid's velocity at injection and production well (m/s).

3.3 Governing equations for fluid flow

For EGS, the fluid transfer is mainly attributed to the production fluid circulation within the wells and the reservoir. As discussed earlier, the maximum pressure at the bottom hole of the production well for EGS must be less than the minimum required pressure for the fluid's phase change. Therefore, no steam or vapor is produced at the EGS and the flow transfer is calculated based on the mass, momentum, energy and entropy equations for single-phase liquid.

The governing equations for the fluid flow within the reservoir and along the wellbores are presented in the following sections.

Reservoir fluid flow:

For a single-phase liquid, the fluid flow at the reservoir was estimated using Eq.22 where q is the Darcy flow velocity (m/s).

$$\varphi \frac{\partial \rho_f}{\partial t} + \nabla(\rho_f q) = 0 \qquad \text{Eq.22}$$

$$q = -\frac{k}{\mu}(\nabla P - \rho_f g \nabla z) = 0 \qquad \text{Eq.23}$$

In Darcy's flow, Eq.23, k is the intrinsic permeability (m^2) of porous media, which is the property of the solid phase to conduct water. Hydraulic head is defined as a function of intrinsic

permeability k (m^2), g as gravity (m/s^2), ρ_f as the density (kg/m^3), μ dynamic viscosity($N\text{-}s/m^2$) and P hydraulic pressure (MPa) (Saeid et al., 2013)

Wellbore fluid flow:

To determine the flow behavior within the phase changes and energy/momentum/ mass exchange, continuity, momentum and energy equations were used (Kjartansson, 2011). For a single phase liquid along the injection and production well, the continuity, momentum, and energy equations, considering constant pipe diameter, are provided as Eq.24 to Eq.26 (Pálsson, 2011):

$$\frac{d}{dz}(\rho u) = 0 \qquad \text{Eq.24}$$

$$(\rho u)\frac{du}{dz} + \frac{dp}{dz} + \rho g + \frac{\rho \tilde{f}}{zd}|u|u = 0 \qquad \text{Eq.25}$$

$$(\dot{m}u)\frac{du}{dz} + \dot{m}\frac{dh}{dz} + \dot{m}g + \dot{Q} = 0 \qquad \text{Eq.26}$$

Where, u is the velocity (m/s), $\dot{m}$ is the total mass flow in the well (kg/s), $\dot{Q}$ heat loss (W/m) and, $\tilde{f}$ is the friction factor. The momentum equation consists of inertia terms, pressure change, hydrostatic pressure and head loss due to friction. Eq.27 is the Blasius equation which was used to determine the head loss due to friction for smooth pipes where Re is the Reynolds number and, $\tilde{f}$ is the friction factor.

$$\tilde{f} = (100\ \mathrm{Re})^{1/4} \qquad \text{Eq.27}$$

Eq.26 corresponded to the kinetic, enthalpy and potential energy of the porous media considering the heat loss per unit of pipe's length. The final wellbore fluid flow would be the system of all three equations (Eq.24, Eq.25, and Eq.26) through the length of z.

3.4 Numerical modeling with FEFLOW

The efficiency of geothermal energy relies on a well-designed power plant suited to the specific geothermal system (Franco and Vaccaro, 2014). In this research, a numerical model was designed to simulate and predict the outcome of the EGS operation. A conceptual model for a saturated porous media, considering the hydraulic and thermal properties, geological characteristics, and restrictions of the selected site were designed. The numerical scheme of conceptual model was produced by mathematical representations, and the modeling process was finalized using simulation software.

Finite element method (FEM) opted as the numerical method to represent the conceptual model due to its flexibility and accuracy of boundary conditions assignment to the model. Additionally, FEM is known as a better representation of the conceptual model's characteristics in comparison to finite difference and finite volume methods (Diersch, 2013).

FEFLOW is capable of modeling coupled flow, mass and heat transport at complex conditions including variable saturation, free surfaces, multispecies reaction kinetics, non-isothermal flow, and multi diffusive (thermohaline) effects (Diersch, 2013). In this research, FEFLOW was proposed as the simulation software to solve the coupled flow and heat transport equations in a three-dimensional condition for saturated porous media.

The numerical analysis of the geothermal system consisted of steady state and transient analysis. The simulation results of the steady state model provided the initial condition of transient modeling. Additionally, the calibration of the thermal gradient of the simulation results vs. the

generic temperature data set after steady state decreases the misstatement of the preliminary parameters.

In the following part, a brief description of the FEFLOW meshing systems, the initial and boundary conditions for fluid and heat transfer and simulation's error tolerance and time steps is provided.

3.4.1 **FEFLOW meshing system**

A finite element mesh is a fine representation of the domain including numbers of nodes, which are creating triangular, tetrahedral or rectangular elements. The nodes are selected to form dense, but not overlapping sets of elements, which assure the computational efficiency, and robustness of the model (Diersch, 2013). The appropriately refined mesh would enhance the accuracy of the numerical analysis.

Three main characteristics have been defined to distinguish the mesh systems, which provide specific information regarding the positioning of the nodes and element's shapes within the system.

1) Conformity: the adoption of the edges and faces of neighboring elements,
2) Alignment: the matches of boundary and elements' surfaces, and
3) Topology: defines the structured or unstructured mesh system, considering the surrounding points' indexes of each individual system.

In FEM, most of the meshes are unstructured, conforming, surface aligned meshes to represent dense, but not overlapping, numerical approximations of the model with the highest accuracy of

the computational approximation. In this research, Advancing Front Method was opted to generate the finite element mesh.

Advancing Front Method (AFM):

AFM generates unstructured triangular meshes in 2D. The numbers of generated elements vary based on the complexity of the model and the geometry of the boundary condition. The discretization process commenced from the initial front (super mesh) and followed by three main patterns which are corresponding to the angle (δ) between two consecutive parts of the supermesh (George, 1992). Based on these patterns, two edges with the angle of $\delta \leq \frac{\pi}{2}$ would create a single triangle. Two triangles would be generated with an internal point and two segments while the angle between sections is between $\frac{\pi}{2}$ and $\frac{2\pi}{3}$. For a single retained segment, a triangle would be generated with an internal point while $\delta > \frac{2\pi}{3}$ (George, 1992). The most appropriate internal point is inside the model and in the position to generate an equilateral triangle. The discretization of the domain continues until the domain completely fills up with triangles (Diersch, 2013).

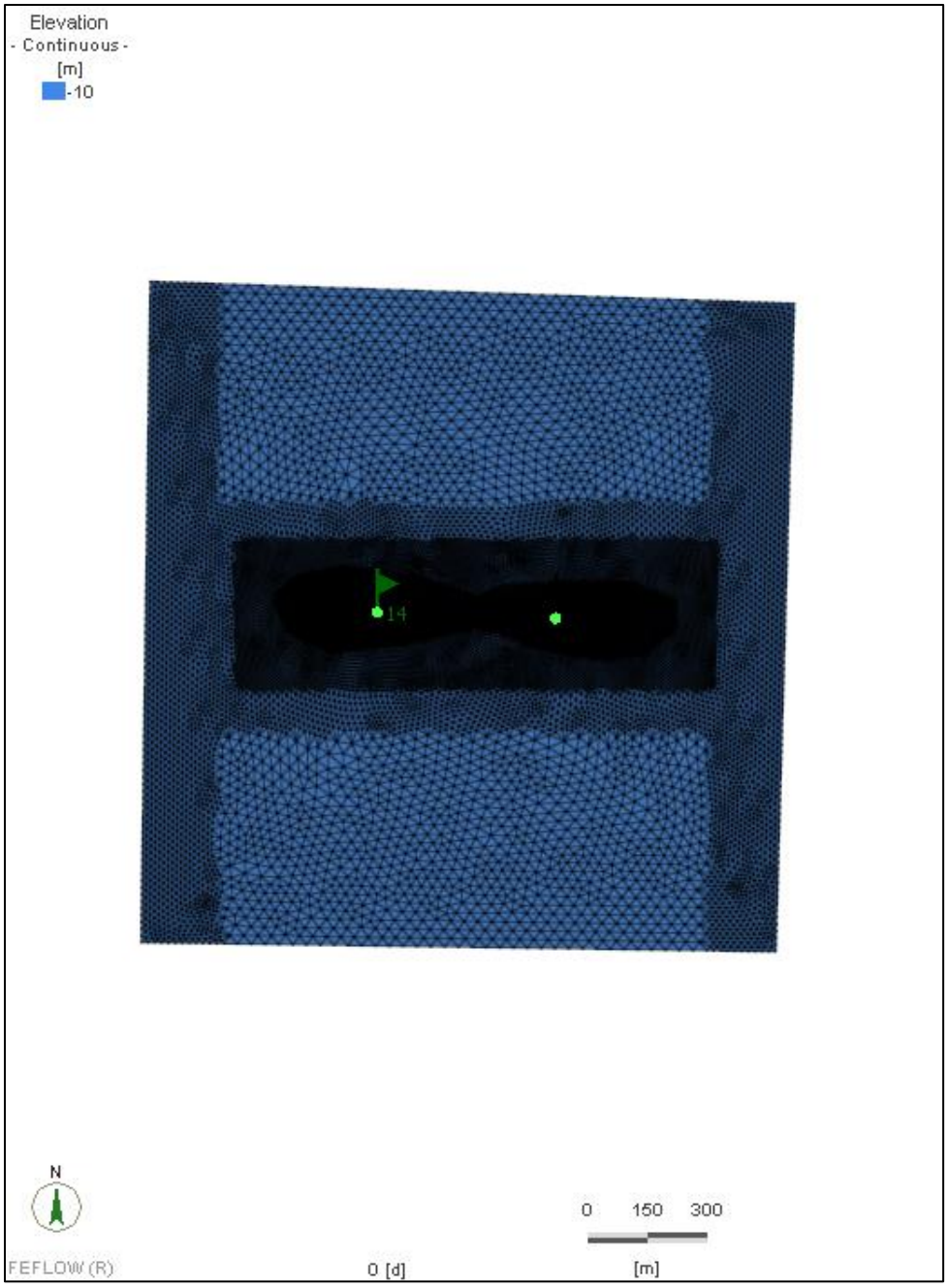

Fig. 3.5. Top view of the mesh system for Tilston site. The finer meshes are regulated to the wells' locations and hydraulic fractured areas. The flags represent the wells locations.

3.4.2 **Initial condition**

Pressure distribution, thermal gradient, and hydraulic head are the fundamental initial conditions in temperature and flow transfer simulation. By adding constraints on acceptable minimum and maximum values of the initial conditions, the range of the simulation results will be restricted (Franco and Vaccaro, 2014). The thermal gradient is one of the most significant initial conditions in heat transfer modeling. As it was discussed in 3.1.2, the heat transfers of the HDR systems are based on conduction and can be calculated by Eq.6.

The initial condition for the hydraulic head in the transient model was the result of the steady state simulation. The steady state model used the summation of pressure head and hydrostatic pressure, which was constant while no extraction or injection occurs. The fluid transfer simulation results at the steady state condition is expected to show constant values due to no flow condition and no well operation.

3.4.3 **Boundary conditions**

Boundary conditions are set to define the model interactions with the fluid, mass or heat flow system (Franco and Vaccaro, 2014). For geothermal models, it presents the flow and heat entering the reservoir.

Four types of boundary conditions are introduced to numerical models. First kind or Dirichlet condition assigns fixed values to specific locations within the boundary and borders. Second kind or Neumann condition defines specific flow or flux across the boundary. Third kind or Cauchy condition introduces transfer coefficients, which reduce the inflow/outflow into/out of the domain, and well boundary condition defines a single point source, usually as injection or production wells in hydrogeology. For each specific site, one or all of the mentioned boundary conditions can be applied.

The hydraulic head and constant temperature boundary conditions were applied to the model. Both of these conditions are from the first kind or Dirichlet conditions. The thermal boundary condition for the steady state was assumed to be the constant temperature of 6°C at the top and a constant temperature of the Precambrian layer at the selected sites. The constant hydraulic head

of -10 m applied to the west and east sides of the model from top to the bottom of the model (Fig. 3.6).

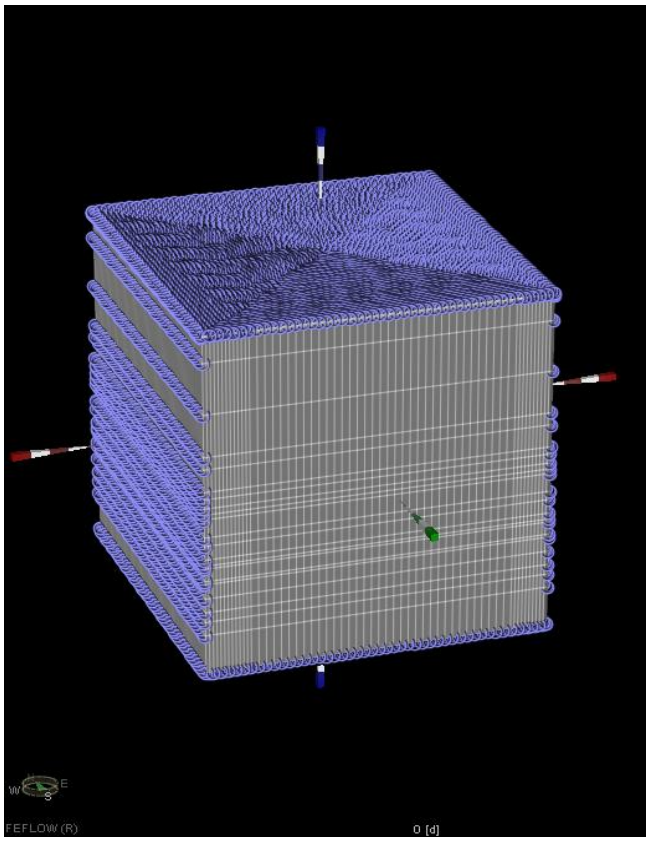

Fig. 3.6. 3D view of the model showing the hydraulic head boundary condition at the top, bottom and edges of the model.

For the transient state, the same hydraulic and upper thermal BCs were applied. The only difference between the BCs at the transient state and steady state was related to the application of single nodes as wells and heat flux, from simulation results at steady state, as the bottom thermal BC. A doublet well was applied to the EGS in order to simulate the flow and heat transfer within the geothermal field. To design the well BC, appropriate flow rate, well distance and well diameter were estimated based on the following section.

Flow rate

The power generation is mainly based on the flow rate of the EGS wells operation. As it was mentioned in the introduction, the geothermal power plants have varieties of production rates. In this research, the power plant was designed to provide the minimum 10 MW electricity considering a reservoir life time of 30 years. To estimate the required flow rate to provide this capacity, Eq.28 was used (Agemar et al., 2014).

$$\dot{C}\,(e) = \rho_f(c_f)Q\,(T_{in} - T_0) \qquad \text{Eq.28}$$

In this equation, $\dot{C}$ is the electricity production capacity (W), ρ_f is the fluid density (kg/m^3), c_f specific heat capacity of the fluid at constant pressure (J/kgK), Q is the flow rate (m^3/s) and T_{in}, T_o input and output of the plant (K).

Well distance

The assignment of multiple wells reduces the pressure and temperature drop at the bottom hole of the production well. For this research, a doublet well including one injection and one production well were designed for the simulation of the heat transfer.

The appropriate distance between injection and production well/wells based on the reservoir lifetime would provide vital information regarding thermal breakthrough of cold water from the injection to the production well(s) (Ferguson and Grasby, 2014). Gringarten and Sauty (1975) determined the well distances using equation (Eq.29) which is the analytical solution of a differential equation for heat transport including enthalpy and internal energy estimations. For this equation the densities are ρ_f and ρ_s (kg/m^3), specific heat capacities c_s and c_f (J/kgK), the thickness of aquifer (for hydrothermal systems) or reservoir h (m), injection/production rate Q

(m^3/day), the thermal conductivity of reservoir λ_s (W/mK), and life time of the reservoir or the time before the thermal breakthrough Δt (years).

$$D_w = \sqrt{\frac{2Q\Delta t}{[(\varphi+(1-\varphi)h+(\varphi+(1-\varphi)\frac{\rho_s c_s}{\rho_f c_f})^2 h^2+2\frac{\lambda_s \rho_s c_s}{(\rho_f c_f)^2}\Delta t)^{0.5}]}} \qquad \text{Eq.29}$$

Well diameter

Well diameter values for EGS systems could be varying from 20 to 34 cm (Polsky et al., 2008). The well diameter does not affect the capacity and production rate of the wells significantly. In an example from Handbook of groundwater development (Roscoe Moss Company, 1990), doubling the well size, increased the specific capacity by only 9% . However, with the same flow rate, by decreasing the well's diameter, the velocity of the fluid transfer increases, which results in less heat loss at the production well.

3.4.4 **Simulation**

In addition to the defined parameters and boundaries, FEFLOW has some default assumptions, which control the simulation. These assumptions are surrounding the groundwater behavior, aquifers status, numerical parameters, anisotropic and transport parameters, equation solve and field line computation.

To control the time stepping and the iteration of non-linear problems, the dimensionless error was calculated at FEFLOW using error tolerance. This method is the average absolute error divided by the maximum value of initial condition or boundary condition and is equal to 0.001 for the primary variable. Euclidian L2 integral (root-mean-square) norm was applied to calculate

the average of absolute error (Eq.30), where x is the primary variable (temperature) and n indicates the number of steps (Diersch, 2013).

$$|x| = \sqrt{\frac{1}{n}\sum_{n=1}^{n} |x_n|^2} \qquad \text{Eq.30}$$

If the error of the simulation exceeds the defined maximum number of iteration, the simulation will be stopped without convergence.

In addition to the mentioned simulation assumptions, the solver type, and time series selection are highly important. Between the direct and iterative methods, the iterative methods are superior to large systems (Diersch, 2013).Among the iterative solvers, Preconditioned conjugate gradient (PCG) for symmetric and Preconditioned Lanczos BiCGSTAB for nonsymmetric linear systems are preferred as the solver types by FEFLOW for less complex problems with lower simulation time.

In FEFLOW, the system of simultaneous linear algebraic equations after simplifications is given as Eq.31, where R is the system's matrix with N_{eq} (number of equations) rows and columns, ξ is dimensional solution vector, and b_c is the corresponding Dirichlet BC terms.

$$R \times \xi = b_c \qquad \text{Eq.31}$$

A *preconditioning* term defines a transformation type, which reduces the number of iteration required for convergence by leading the ratio of maximum to minimum eigenvalues to one (ε (R) $\rightarrow$ 1) (Diersch, 2013). If the number of iterations which are required to minimize the error by factor of a is $\dot{S}$ (a), the smaller ε values, decrease the iteration steps as shown at Eq.32.

$$\dot{S}\,(a) \leq \frac{1}{2}\sqrt{\varepsilon(R)}\,\ln\left(2/a\right) + 1 \qquad \text{Eq.32}$$

Conjugate gradient, as an iterative method with enhanced convergence, which is used for deriving the numerical solution of a symmetric system of linear equations with positive defined matrix (Herbert et al., 1988). The limited number of iterations required for convergence (proportional to the number of equations) makes CG a preferred method for solving linear symmetric systems. An alternative method was introduced by applying the precondition transformation to CG method and enhancing the convergence pace (PCG).

Conjugate Gradient Square CGS method is an iterative method for solving linear non-symmetric equations, which is based on squaring the residual polynomials. On one hand, the advantage of this method is rounding the errors due to squaring the polynomials; on the other hand, it lacks in decreasing the error within simulation progress (Diersch, 2013). The Preconditioned Lanczos BiCGSTAB is an alternative robust and high efficient technique, which requires a small storage demand and low computational cost (Diersch, 2013). BiCGSTAB shows superior behavior comparing to (CGS) at systems breakdowns (where R is not positive) which led it to become the first priority as a non-symmetric system solver (Diersch, 2013).

After selection of the method for fluid (symmetric) and heat (non-symmetric) transfer systems simulation, the appropriate time series for transient state modeling opted.

The automatic time step defines the temporal discretization of the simulation in this research. To use the automatic time series, the initial time step length, final simulation time, growth factor and time step size were required to be defined for the model. Predictor-corrector method (GLS) is a time integration method used to control the time stepping based on monitoring the solution

process by estimating the error reduction at specific time, in which, the time step length varied according to the temporal accuracy requirements (Diersch, 2013) which consequently results in increase or decrease of the time steps length when is necessary.

The accuracy of time steps at automatic time series was controled with two defined schemes at FEFLOW. GLS 1st-order Forward/Backward Euler (FE/BE) and GLS 2nd-order forward Adams-Bashforth/ Trapezoid rule (AB/TR) are defined to solve the simplified system of temporal equations. The 2nd-order AB/TR method shows a higher probability of oscillation error when large time steps are used. Therefore, FE/BE was used to diminished the error possibility from time step section. The initial time of 1E-5 day was opted to avoid long periods and quicker convergence, which was increased after several days of wells' operation to 0.1 day.

The simulation was run with the following assumptions with the mentioned simulation factors:

1. Free upper layer and confined formations from layer 2 to the end of the model.
2. Constant mass
3. Variable viscosity and nonlinear density as a function of temperature.

The temperature effect on the density and viscosity of water at atmospheric pressure is shown in Fig. 3.7. It was assumed that density changes proportionally to the temperature when the temperature difference between the fluid at the ambient condition and the final derived temperature is below 30°C. However, for higher temperature differences comprehensive relation between temperature and the viscosity and/or density were required.

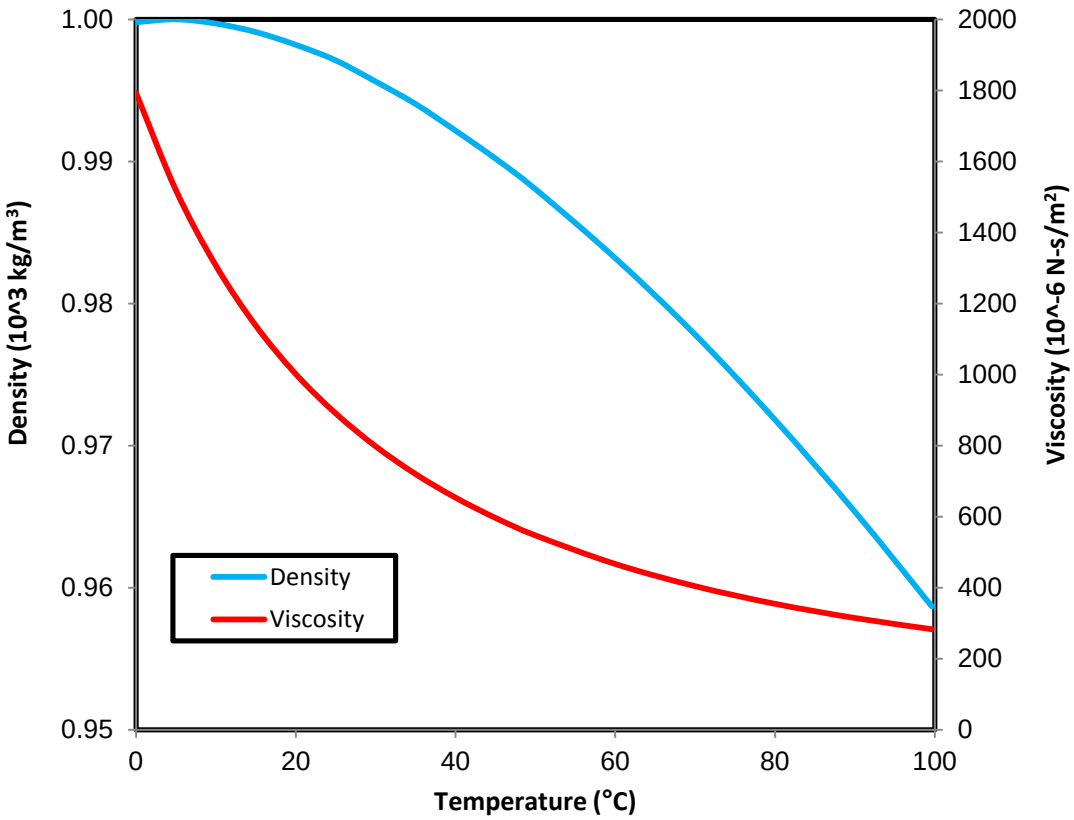

Fig. 3.7. Temperature dependency of density and viscosity at a constant pressure of 10 MPa.

At FEFLOW variable viscosity has been introduced as Eq.35. τ and τ_0 are demonstrated at Eq.33 and Eq.34 which represent the temperature of the fluid at the ambient condition and as the function of derived temperature at each time step.T_0 is the temperature at ambient condition (°C), and μ_0 is the dynamic viscosity at ambient condition (N-s/m^2).

$$\tau_0 = \frac{T_0 - 150}{100} \qquad \text{Eq.33}$$

$$\tau = \frac{T - 150}{100} \qquad \text{Eq.34}$$

$$\frac{\mu}{\mu_0} = \frac{1 + 0.7063\,\tau_0 - 0.04832\,\tau_0^{3}}{1 + 0.7063\,\tau - 0.04832\,\tau} \qquad \text{Eq.35}$$

The fluid's density assumed to have nonlinear relation with temperature as well. FEFLOW estimates the temperature-dependent fluid density of water by a 6th order accuracy as Eq.36:

$$\rho(T) = a_1 + a_2 T + a_3 T^2 + a_4 T^3 + a_5 T^4 + a_6 T^5 + a_7 T^6 \qquad \text{Eq.36}$$

The effect of pressure and mass fractions on the fluid's density were neglected to simplify the simulation and considering the temperature as the main factor in density variation. The constant coefficients are given at Appendix (i).

3.4.5 **Calibration**

The simulation results of the steady state were based on assumptions made for deriving the thermal properties e.g. thermal conductivity, porosity, and volumetric heat capacity of the selected site. These assumptions increased the uncertainty of the simulation and consequently enhanced the error of the results. Thermal properties of the formations were calibrated to diminish the error possibility. The RMS method (Eq.30) was used to calculate the error of thermal gradient between the simulation results and the generic data set.

Target formations with the highest uncertainty were chosen for data calibration. For some rock types, an increase in temperature increases thermal conductivity, and for other types the opposite is true; therefore, new sets of thermal conductivities were estimated, by taking the rock types into consideration. At first, the thermal conductivity at ambient condition (temperature of 20°C and 1

atmosphere pressure) were re-estimated. Then the effective thermal conductivity was recalculated and applied to the model for several times.

Each new data set was generated by trial and error, with a focus on the target formations and considering thermal conductivity sensitivity analysis. For the layers with higher simulated temperatures than the measured data, thermal conductivities were decreased, and for layers with lower temperatures, it was increased. Higher thermal conductivity resulted in lower temperature differences between layers, and vice versa. The final calibrated data was used for the transient state modeling.

Chapter 4. Parametrization

Overview

In this chapter, the appropriate site at the Tilston area is selected using well logs and provided map from 3.1.1. The site shows a halite formation at a depth of 1499 m having 118 m thickness. Based on the geological formation of the Tilston site, the thermal and hydraulic properties are determined at ambient condition and by considering the effect of pressure and temperature. After completion of the formations' parametrization, a numerical model is set up using FEFLOW for both steady state and transient simulations. Following the Tilston site, a Generic model is set up to determine the depth impact on the final derived temperature of the EGS considering halite as thermal reservoir.

4.1 Tilston site selection

Considering the Prairie Evaporite as the thermal reservoir for this study, the appropriate location for the geothermal application required a thick halite formation at low depths. The geology of the Williston Basin was introduced in 3.1.1. Halite, potassium salts, carbonates wedges and layers of Evaporite have been recognized within the Devonian-Mississippian and the Elk Point group (Nicolas and Barchyn, 2008). The Hubbard Evaporite was found within the Dawson Bay formation in the middle of the Devonian period, which overlies the Neely member of the Manitoban part of the Williston Basin (Fig. 4.1). This formation is comprised of dolomitic mudstone at its base overlain by fossiliferous limestone capped by anhydrite and dolomite. The thickness of the formation is rather uniform from -40 to -50 m from the outcrop in Manitoba to west-central Saskatchewan; however, the thickness of salt varies between 0 and 18.9 m (Amaral, 2014).

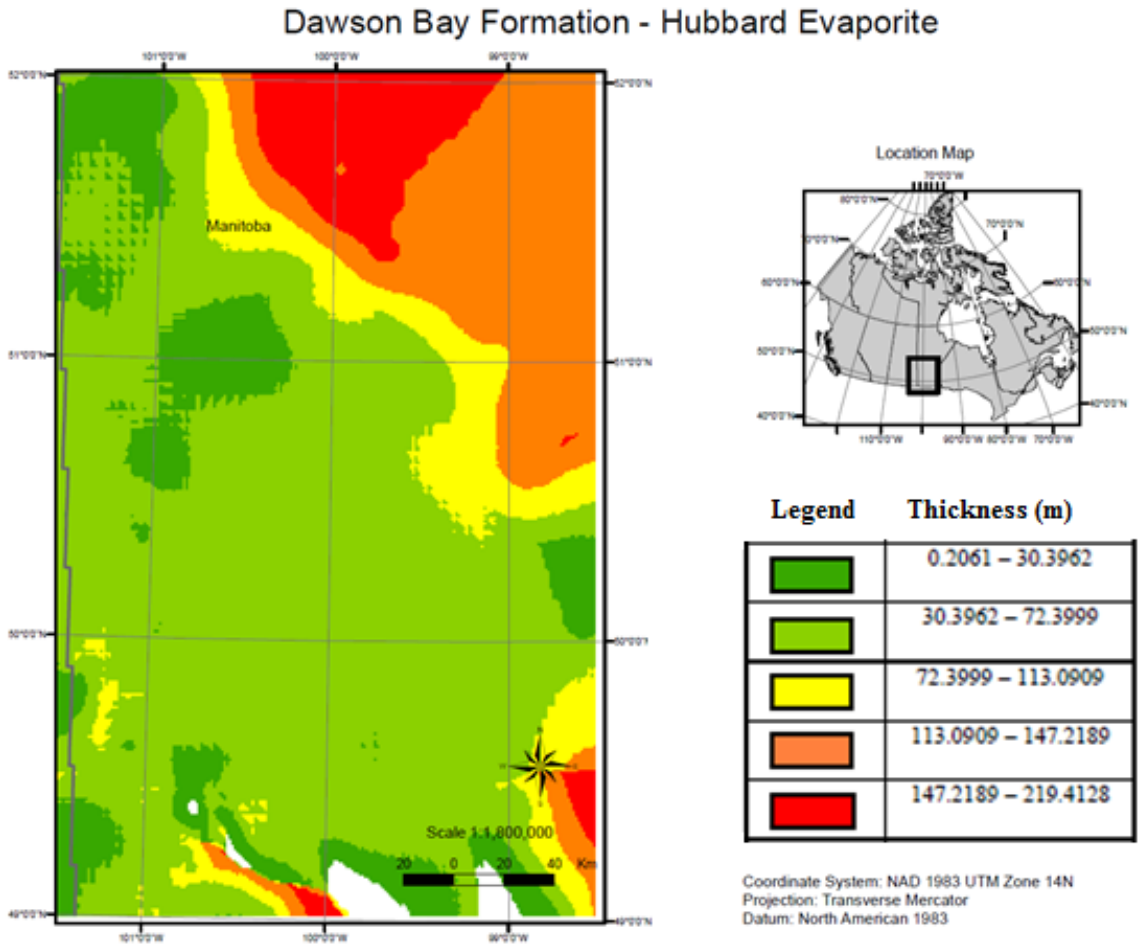

Fig. 4.1. Thickness of the Hubbard formation within the Dawson Bay formation; the formations' thicknesses increase from green to red colour.

At the lower part of the Devonian period, thick halite beds containing occasional potash zones at the top and minor anhydrite at the bottom exist within the Prairie Evaporite (Nicolas and Barchyn, 2008). Thin layers of potash have been recognized at the border of Manitoba and Saskatchewan at the most south-west regions. Considering the dispositioning and dissolution procedure of salt formations, the maximum recent thickness of Prairie Evaporite is 140 m near the boundary with Saskatchewan, which is decreasing to 10 m along the border of the formation.

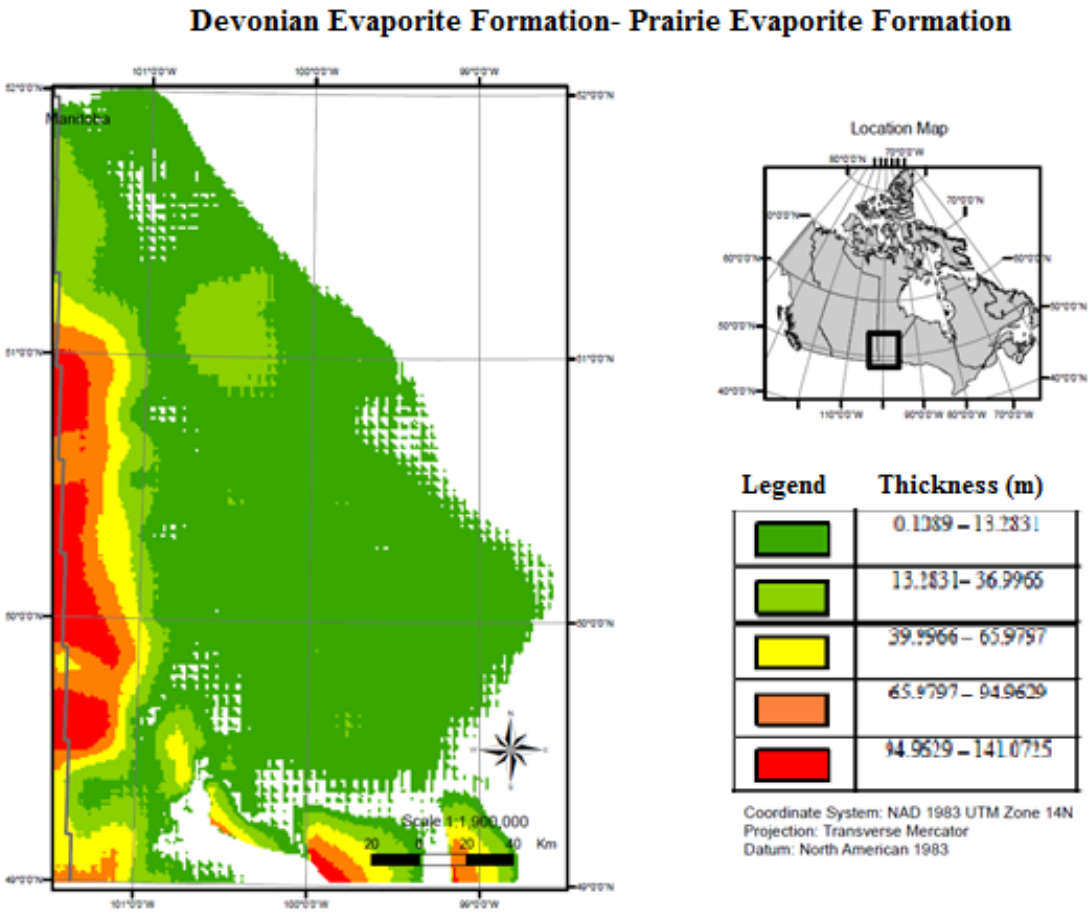

Fig. 4.2. Thickness of the halite within the Prairie Evaporite Formation; the halite`s thicknesses increase from green to red colour

Based on the map provided in Fig. 4.2 and the depth of Prairie Evaporite in Fig. 3.2, Fig. 3.3 and Fig. 3.4, two preliminary regions opted at the south-west of Manitoba for further investigations regarding geothermal potentials, which are presented in Table 4.1 and Fig. 4.3.

Table 4.1. Coordination of region 1 and region 2

	COORDINATES
Section 1	49° 0' 0" N-101°0 ' 0 " W, 49° 43' 35" N-101° 34 ' 8 " W
Section 2	49° 43' 35" N-101 ° 0 ' 0 " W , 50° 36' 15" N-101° 34 ' 8 " W

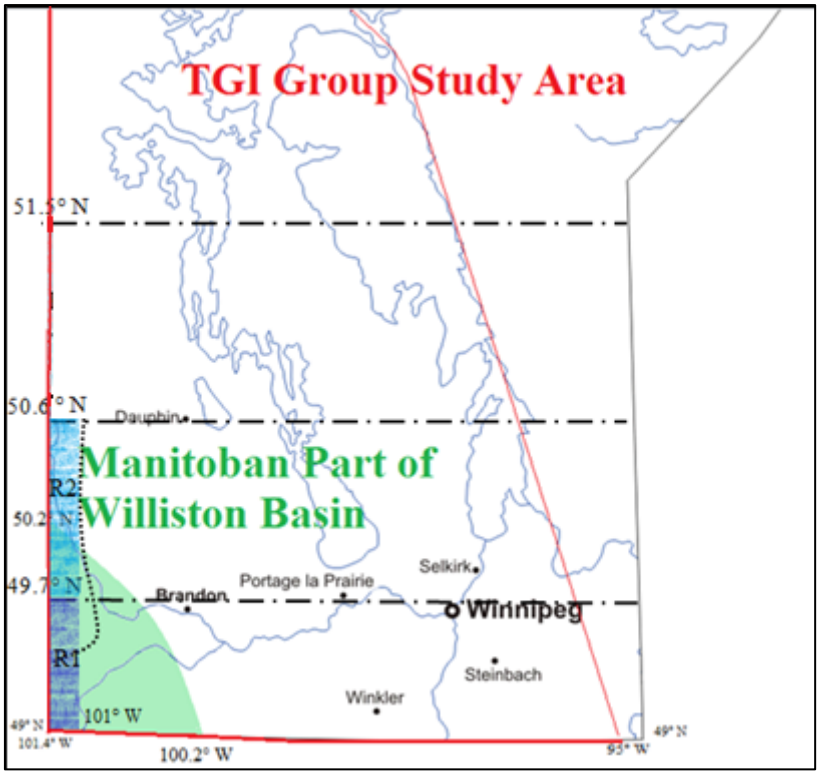

Fig. 4.3. Appropriate regions for geothermal application investigations are shown as R1 and R2 within south-west of Manitoba.

The most appropriate location for the site selection attributed to the region with the maximum recorded temperature for its lowest formation. The drilling reports of the wells with lower bottom hole elevations than the Prairie Evaporite layer was used to achieve the temperature data. Table 4.2 represents the wells information regarding the bottom hole temperature (BH), total vertical depth (TVD) and regions (R1 and R2).

The drilled wells have identical license number following the drilling and production regulations set by the government of Manitoba and Dominion Land Survey (DLS), which demonstrates the wells location. The DLS method is widely used to divide fields in Western Canada into one square mile areas for various purposes. DLS comprises of the meridian, township, range, section, and east or west section representations. For example, SE 20-12-05-

W4 is the location of a field at the south-east of township line 12 and range 5 at section 40 on the left side of meridian 4.

Table 4.2. Well log information regarding the highest temperature of wells' BH within the regions.

DLS	Licence number	TVD (m)	BH Temperature (°C)	Region
100/16-33-005-24W1/00	9	1566.1	49	R1
100/16-16-001-27W1/00	486	2084.8	57	R1
100/02-17-018-22W1/00	2502	1172.9	53	R2
100/16-34-006-29W1/00	2523	1955.9	49	R1
100/02-14-018-29W1/00	2534	1332.3	51	R2
100/11-29-001-25W1/00	2543	1947.7	57	R1
100/09-06-002-26W1/00	2610	1986	61	R1
100/01-28-005-24W1/00	2612	1575	52	R1
100/08-13-005-29W1/00	2696	2060	65	R1
100/05-24-002-26W1/00	2766	1950	58	R1
100/01-25-004-23W1/00	4859	1670	53	R1

Finally, the most appropriate geothermal field, satisfying the geological and thermal specifications, along with the actual data accessibility was selected at Tilston from region 1.

4.2 Thermal parametrization

After selection of the geothermal site, the lithology and temperature were estimated using drilled well logs at the site. As it was mentioned in 3.1.2, the generic temperature data set will be set as the site's temperature as a combination of observed temperatures and analytical derived temperature method.

Various technical reports were investigated to derive the most comprehensive information regarding the Tilston region. In the following sections, the geology, temperature, pressure, thermal and hydraulic properties of the selected site are determined specifically.

4.2.1 **Geology & Lithology**

The formation's compositions were identified by the 002523 drilling report, done by Asamera Oil Corporation Ltd (Government of Manitoba and Manitoba Mineral Resources, 2014), to estimate the specific lithology of the selected site. In this report, the formation and their thicknesses were described from the surface to the Precambrian formation. Each formation is comprised of various rocks such as Dolostone, Limestone, Shale to simplify the modeling only the most common component opted as the formation's main composition and thermal and hydraulic properties of that formation were estimated based on that specific component. Appendix (c) shows the Tilston site lithology and formations from the surface to the Precambrian.

4.2.2 **Model discretization**

The mesh system was generated for the Tilston site with 1600×1600 m^2 area, using AFM, and ~0.9 m length between each two nodes. Fig. 4.4 is the representation of the meshing

system and elevation distribution for the Tilston model. The formations' geology, numbers of layers and their thicknesses are presented in Appendix (c).

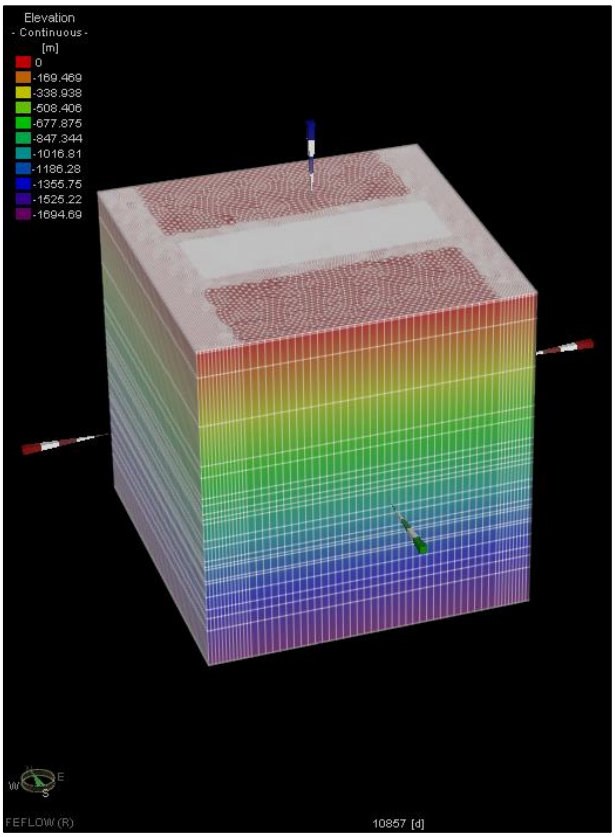

Fig. 4.4. 3D view of Tilston model, the elevation is descending from red to purple.

4.2.3 **Temperature data**

The temperature data set was derived following the method mentioned in section 3.1.2. For the measured section, the actual data was gathered from the drilling reports of wells 007394 and 6705 for depth of 4 to 600 m and 800 to 1200 m respectively. The ground surface temperature was assumed to be at 6°C based on the average annual surface temperature of Manitoba (Government of Canada, 2015). The Precambrian formation was opted as the last layer of the simulation model with a temperature of 60°C based on Table 4.2 and temperature data provided by Nicolas and Barchyn (2008).

Various scenarios were carried out to estimate the formations' temperature based on Eq.3, and the one with the minimum error had been selected. In each scenario, with the same Q and D values, A_0 and λ were changed to improve the calculated temperature

Therefore, the temperature data set for Manitoban part of Williston Basin from the surface to the depth of 1960 m was generated as a combination of actual and calculated temperature data. Fig. 4.5 shows the resulting temperature log and Appendix (d) represents the temperature values for each specific depth at the Tilston site.

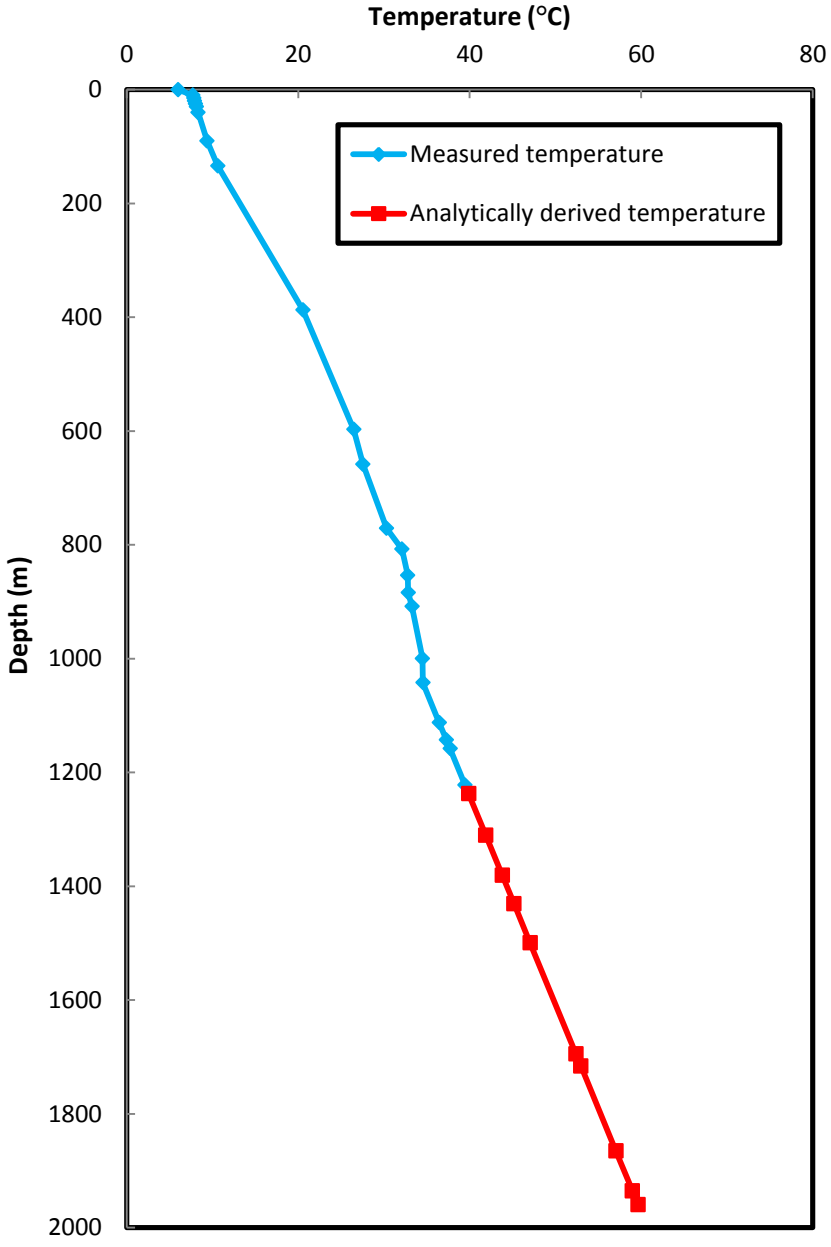

Fig. 4.5. Temperature data set as a combination of measured and analytically calculated data based on selected parameters at Appendix (e)

4.2.4 **Thermal properties of solid phase:**

For each of the layers, thermal conductivity, specific heat capacity and porosity were identified at ambient condition (Grasby et al., 2012). Then, by applying the methods described in Chapter 3 (Table 3.2, Appendix (g)), Eq.8 and Eq.9, the effective thermal properties as a function of temperature and pressure were calculated. The effective porosity had the same value as the porosity at ambient condition due to negligible effect of pressure and temperature on its value. The thermal properties of the Tilston region are presented in Appendix (g) and Appendix (h).

4.2.5 **Thermal properties of the liquid phase:**

Due to the lack of ground water, the only liquid phase was the production fluid, which was selected as brine having a NaCl concentration of 6% (brine NaCl 6%). Based on Chapter 3, the density of the brine at a temperature of approximately 47°C and at a pressure of 31 MPa was 1100 kg/m^3 with a thermal conductivity of 0.54 W/mK. The expansion and compression coefficients for this density were 49.8 kg/(m^3°C) and 9.93 kg/(m^3kbar) respectively. The volumetric heat capacity was set to 4.18 MJ/ (m^3K), which was the product of specific heat capacity of brine at the proposed temperature (3.81 kJ/kgK) and density (1100 kg/m^3).

4.3 Hydraulic conductivity

Hydraulic conductivity is the ability of a saturated or unsaturated area to transfer fluid within its void spaces and fractures. The EGS depends on the fluid circulation between the injection and production wells through the reservoir and the temperature radius around the wells, which are directly related to the hydraulic conductivity of the layers in all directions. In this

research, it was assumed that each formation is homogeneous and anisotropic which led to various values of conductivities in horizontal and vertical directions.

Table 4.3 provided the hydraulic conductivities of the Tilston site formations for their main components from the surface to the bottom of the halite layer (reservoir) based on Domenico and Schwartz (1998). In-situ hydraulic test on undisturbed bedded halite proposed a hydraulic conductivity of 1×10^{-14} m/s for saline formation (Ingebritsen and Ward, 1998) These parameters were attributed to non-fractured rocks only considering the natural porosity of the formation.

Table 4.3. Hydraulic conductivity of the main components of the Tilston site's formations

Formation components	$K_x=K_y$ (m/s)	K_z (m/s)
Clay	1E-11	1E-12
Glacial Draft	1E-10	1E-11
Shale	1E-13	1E-14
Limestone	1E-9	5E-10
Fine Grained Sand	2E-7	2E-8
Sandstone	5E-13	5E-13
Dolomite	1E-9	1E-9
Halite	1E-14	1E-14

4.4 EGS well boundary condition

In section 3.4.3, the well BC was determined based on the flow rate, well distance and well diameter. To estimate the adequate flow rate for generating 10 MW electricity, specific heat capacity of the injected fluid and temperature of injected and extracted fluid were required. The brine was assumed to have constant temperature of 15°C at the injection point and final temperature of 47°C at Tilston site based on the reservoir depth (Fig. 4.5), assuming no heat loss for the fluid from the reservoir to the surface to achieve the maximum capacity. The flow rate considering Eq.28 and the mentioned assumptions were calculated as approximately 7000 m^3/day.

To calculate the most appropriate distance between wells, various life times for the reservoir (from 5 to 30 years before the thermal break through) have been used. Table 4.4 represents the well's distances for a constant flow rate of 7000 m^3/day and various reservoir life time. Well distance was at 253 m for a reservoir's lifetime of 5 years and increased to 620 m at a lifetime of 30 years. In this study, 560 m was opted as the appropriate distance between the injection and production well to simulate the thermal and hydraulic transfer for the Tilston site. This referred to a reservoir lifetime of approximately 28 years; however, the simulation was run for 30 year operation to assess the effect of the geothermal system overuse.

Table 4.4. Doublet well's distance for a constant flow rate of 7000 m^3/day and various thermal breakthroughs.

D_w (m)	Q (m^3/day)	Reservoir life time (years)
253	7000	5
358	7000	10
506	7000	15
566	7000	20
506	7000	25
620	7000	30

The selected distance between the wells must be studied in terms of hydraulic fractures height and length as well. Due to lack of information regarding the fractured salts formations, the fractured Barnett shale mapping, presented by Fisher and Warpinski (2012), was used for the salt formation in this study as well. Based on their measurements, the maximum height of fractures was 600 m and the average value was approximately 400 m. Hence, it is theoretically feasible to fracture 500 m of the reservoir from the injection to the production well.

Considering the insignificant effect of well diameter on the flow capacity, in this research the well diameter was opted as 10cm (half of the mentioned diameter in section 3.4.3). Therefore, the well BC was designed for 30 years of reservoir's life time, with 7000 m^3/day capacity, 10 cm diameter, and 560 m distance between injection and production well which is shown in Fig. 4.6.

The constant lengths for the production and injection wells was assumed from the surface to the center of the reservoir. The location of the bottom hole was selected in the center of the reservoir to simulate the fractures impact that was directed in vertical and horizontal

directions. FEFLOW assigns the well to the nodes at each slice, which restricts the capability of defining the length to the middle of a layer. Therefore, an arbitrary layer was defined in the middle of the Prairie Evaporite layer for wells assignment. The estimated fractured areas have been applied to this layer as well.

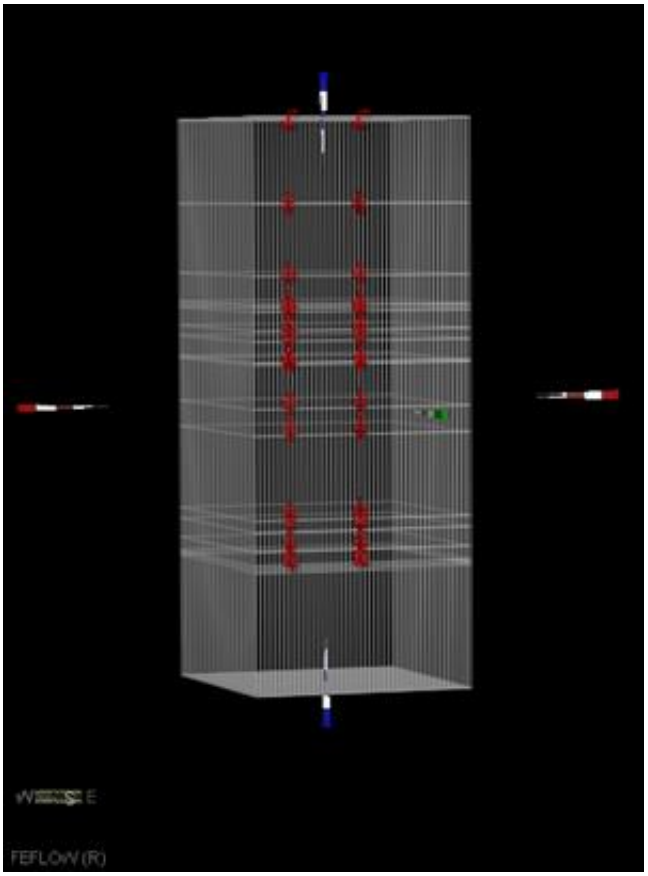

Fig. 4.6. The multilayer wells set up in FEFLOW.

After designing the wells, attributed hydraulic head rise and drop (as pressure changes) were calculated based on Eq.37,Eq.38, Eq.39 and Eq.40 at Appendix (b). The pressure drop is a summation of the surface over pressure, dynamic pressure changes, and friction pressure drop. The surface over pressure was approximately assumed as 0.1 MPa (Harrison et al., 2013). The total pressure drop equaled to the accumulative value of pressure changes mins the static pressure. The static formation pressure for non-artesian wells was negative and for artesian wells positive, considering the effective head at the production well (Harrison et al., 2013). The total pressure drop and total pressure rise for designed wells considering the parameters mentioned in Table 4.5.

Table 4.5. Defined parameters for pressure drop calculation.

D_{Tp}	1430.74 m
μ	0.00108 N-s/m^2
d	0.10 m
k	1E-20m^2
h	118 m
D_{Dp}	0 m

The permeability of uncompacted crystalline salts was determined as 10^{-7} m^2, which decreased incrementally after 500 m of burial to 10^{-21} m^2. This extreme change in permeability is due to the plasticity of salts under deformation and the tremendous propensity of salts to recrystallize under increasing pressure and temperature (Ingebritsen and Ward, 1998). Unfortunately, there is not enough information regarding the exact permeability of the saline formation at 1500 m; therefore, a range of pressure rise or drop with considering the minimum and maximum permeability was estimated. The most appropriate value for permeability considering previous studies opted as 10^{-21} m^2 which led to pressure drop and rise of 0.5 GPa approximately.

4.5 Fractures set up

Hydraulic fracturing due to very low hydraulic conductivity of the halite (10-14 m /s) enhanced the fluid circulation. The accuracy of the fluid flow simulation results highly depend on the spatial discretization and hydraulic head variation at the injection and production wells. Based on section 3.1.3, the hydraulic conductivities values were decreasing from the wells' location to the surrounding area. Therefore, four zones of various hydraulic conductivities have been assumed for the fractured area with finer meshes from zone 4 to zone 1.

Table 4.6. Fluid properties, fractures size and hydraulic conductivities for zones 1 to 4.

Zone	Aperture size (mm)	ρ (kg/m^3)	μ (N-s/m^2)	K_{fr} (m/s)
1	----	1100	0.00108	1E-14
2	1.09E-9	1100	0.00108	1E-12
3	1.09E-5	1100	0.00108	1E-10
4	1.09E-4	1100	0.00108	1E-8

Based on 3.1.3 and the difficulties regarding the identification of the fractures geometry, the fractured area assumed to have approximately empirical shapes with the highest hydraulic conductivity and mesh densities at the wells' locations. The fractures zones at the reservoir, at the arbitrary layer containing the well screens, are given in Fig. 3.2. The largest hydraulic conductivity was at the wells' location which is presented in red colour. The higher mesh density can be observed in the figure as well.

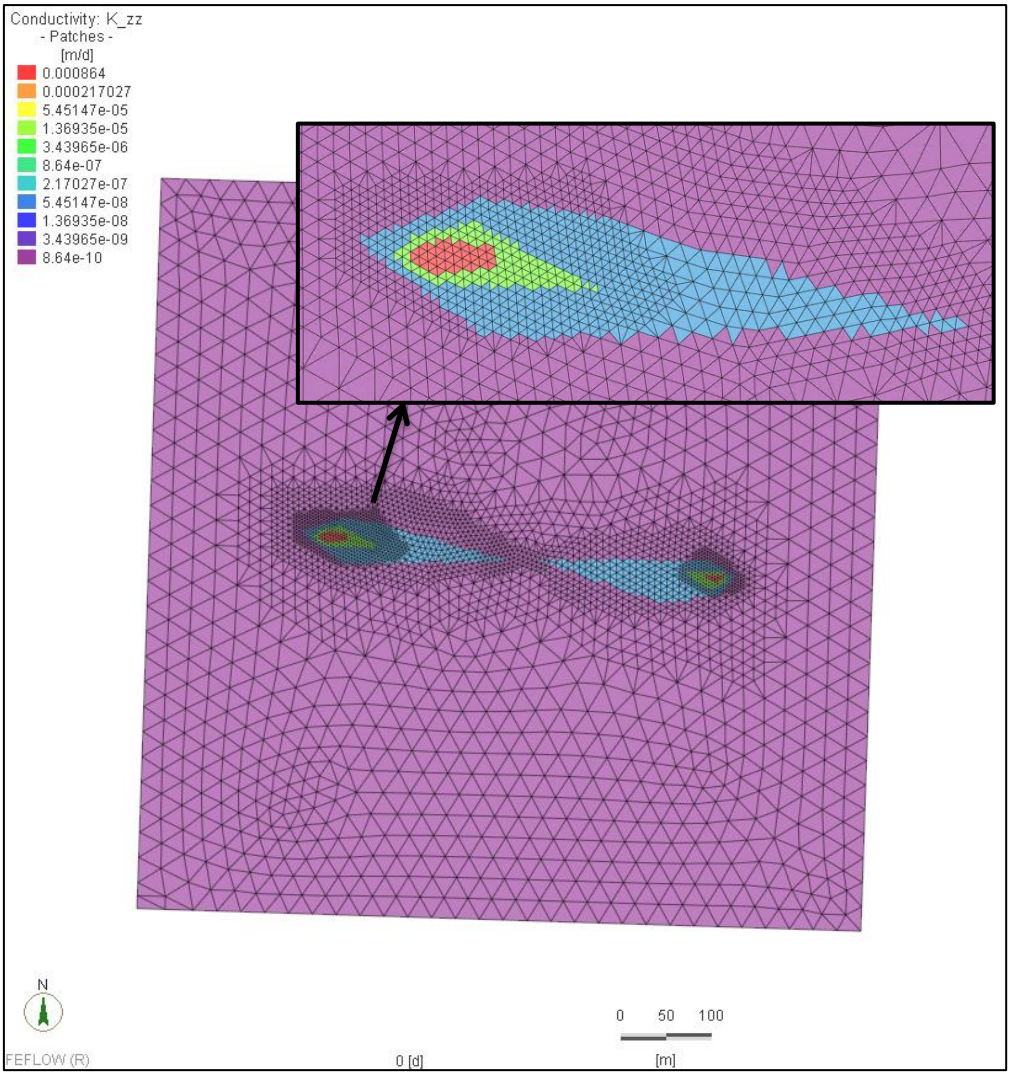

Fig. 4.7. The fractures zones hydraulic conductivities and mesh density of the reservoir of the Generic model.

4.6 Generic model

The reservoir's (Prairie Evaporite) temperature at a depth of approximately 1500 m was estimated at 47.28°C for the Tilston site. Based on the Introduction (Chapter 1), there is a linear relation between depth and temperature. In the Williston Basin, formations' depths are increasing from east to west (Nicolas and Barchyn, 2008)which leads in temperature increase. The lowest depth of the Prairie Evaporite as the reservoir was determined in Saskatchewan at approximately 3 km (Fig. 4.9).

A second model was developed using the approximate location of the deepest point within the Williston Basin to consider the effect of depth on the feasibility of a geothermal application. This model is so called Generic model. On one hand the same formations in the Manitoban and the Saskatchewan part of the Williston Basin led to the same thermal properties and temperature gradient; on the other hand, the provided maps of Grasby et al. (2012) showed a higher thermal gradients of 0.3 to 0.35°C/ m in south-east Saskatchewan. Therefore, a combination of the measured and calculated temperature based on Eq.3 and thermal properties of Craton presented in Appendix (a) was used to estimate the temperature log of the Generic site. As shown in Fig. 4.8, the calculated temperature has good compatibility with the measured data until the depth of 1000 m; however, the higher thermal gradient in Saskatchewan led to lower temperature difference at a lower depth. The final temperature data set for the Generic model is presented in Appendix (m).

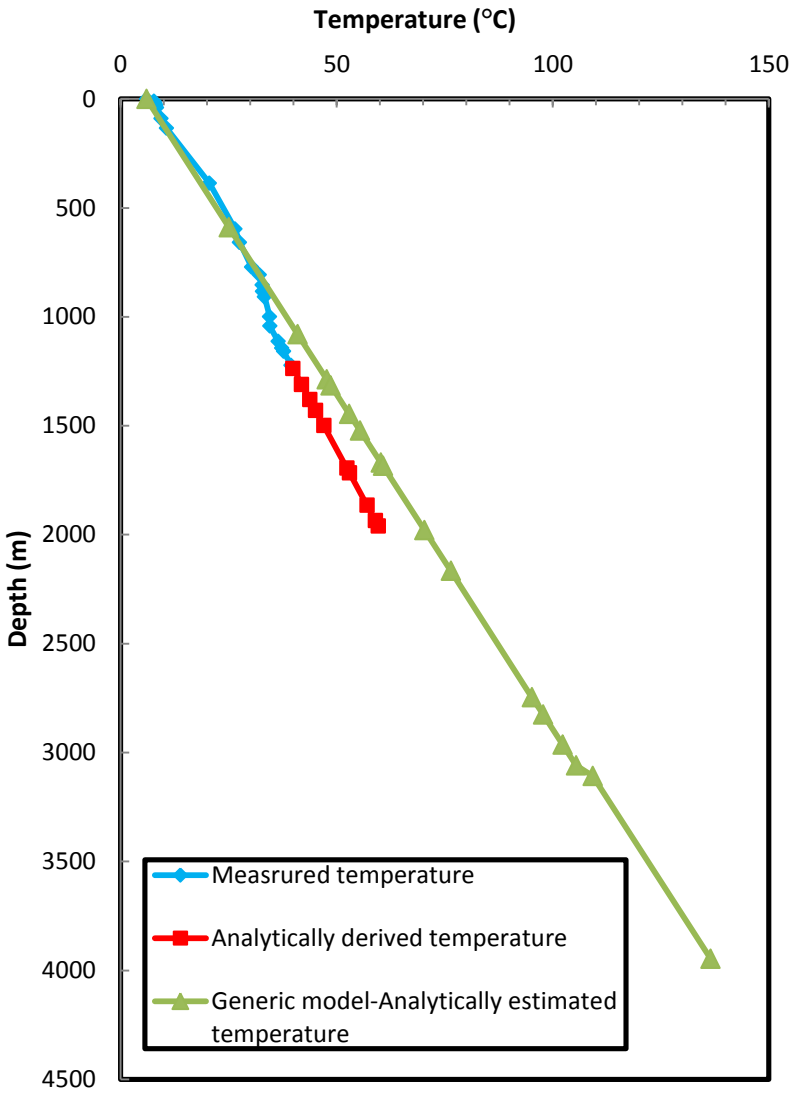

Fig. 4.8. Temperature vs.depth at the Tilston and Generic sites.

Considering the above figure, the temperature of the Generic model proposed as a combination of the measured data in Manitoban part of the Williston Basin and calculated temperature with 0.3°C/m gradient in Saskatchewan. The bottom temperature was 135°C with the surface temperature of 6°C.

BCs and ICs were the same as in the Tilston model (except the bottom temperature) due to presenting the same components in different depth of each formation at steady state

modeling. The thermal properties of solid and liquid phases were recalculated based on new temperature and pressure data sets. The critical part in setting up the Generic model attributed to the thickness, elevation, and temperature of the layers. The formations and their thicknesses were estimated using GeoCando. The number of layers was reduced to 16 since the Duperow formation was represented only by one layer. The comprehensive information regarding the elevation, lithology, and layering are presented in Appendix (l). Thermal properties, temperature, and pressure of each layer were re-calculated using the updated temperature and pressure (Appendix (m), and Appendix (n)).

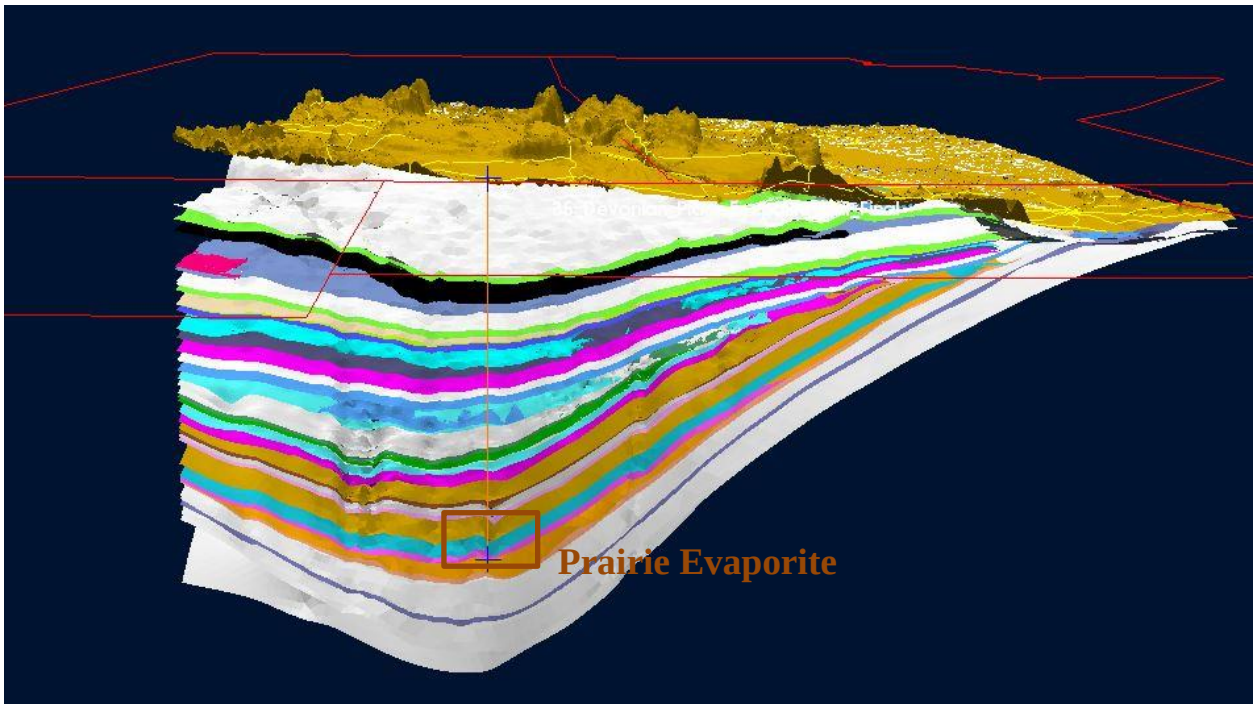

Fig. 4.9. The reservoir's location at the Saskatchewan part of Williston Basin.

This location assumed to be capable of producing a maximum temperature of 110°C at the bottom of the Prairie Evaporite. Therefore, the study area was modeled using FEFLOW at steady state conditions to reproduce the thermal gradient and at transient conditions to estimate the final derived temperature at the wellhead of a production well. The exact same

flow rates, simulation time, simulation equations, error estimation and meshing system were according to the Tilston model as well.

Chapter 5. Results

Overview

In this chapter, the simulation results of the steady and transient state simulations for both Tilston and Generic models are presented, and the calibrated parameters are presented. The fluid flow simulation contained the hydraulic heads over time for the bottom hole of the injection and production well. The heat transfer simulation exposes the final derived temperature of the production wellhead, the fluid temperature along the injection and the production wells, and the increased temperature of the fluid within the reservoir.

5.1 Calibration, Tilston model

The calibration procedure was explained in section 3.4.5. Three sets of calibration were carried out, and the final simulation results were presented at Appendix (j)0. The RMS was calculated between the calibrated simulation thermal gradient and the generic thermal gradient (using the generic temperature data set) with the lowest error of 0.03. The calibrated thermal properties (thermal conductivities) of this set were applied to the transient model containing temperature of each formation and thermal conductivities (Appendix (k)). The calibrated thermal conductivities varied from 1.36 to 7.14 W/mK. The halite formation had the highest effective thermal conductivity of 5.20 W/mK from the surface to the bottom of the thermal reservoir.

Fig. 5.1 shows the generic temperature data set, as a combination of measured and analytically derived temperature, and calibration. The simulated temperature of the halite formation was 1.90°C higher than the generic temperature data set. The fewer temperature differences were observed from 800 to 1000 m depth with approximately 0.29°C temperature. At 1220 m the temperature difference was at the maximum of 4°C which gradually decreased within the next 400 m.

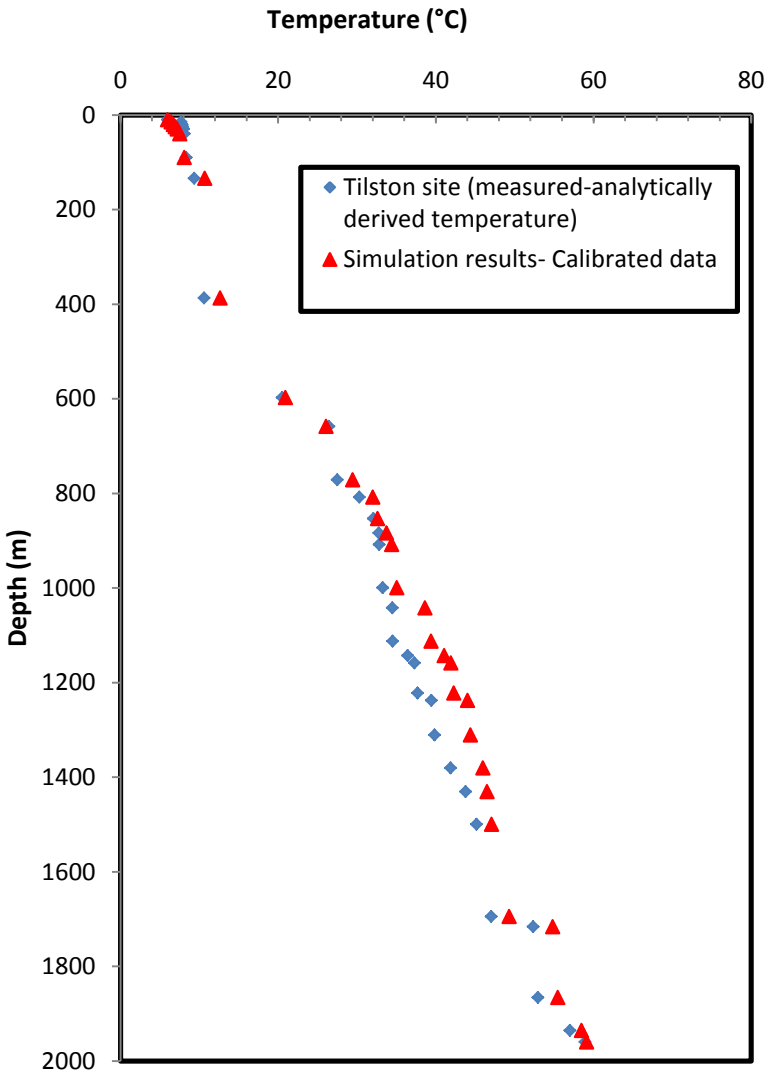

Fig. 5.1. Temperature vs. depth at the Tilston site and the calibration.

5.2 Heat and fluid simulation results, Tilston

The heat and fluid transfer simulation results for the proposed doublet well in section 4.4 are presented in sections 5.2.1 and 5.2.2.

Based on the heat-transfer simulation, the feasibility of the geothermal application for electricity production at the Tilston site was determined. Temperature-depth at the well locations, temperatures at the injection and production wellheads, and the effect of the thermal reservoir on the production fluid's temperature were proposed. The hydraulic heads within the injection and production wellheads and well bottoms were investigated in the fluid transfer section to determine the accuracy of flow circulation within the well systems. Thirty-six observation points were used to track the systems' behaviour along the injection and production wells and at the neighboring nodes within the thermal reservoir. The well screens were located in the middle of the thermal reservoir, and the simulation results were regulated to the observation points at this level. The model was run for 30 years, and the heat and fluid simulation results were recorded after 1, 10, 30, 90, and 365 days, as well as at 2, 10, 20 and 30 years. The intensive changes on hydraulic head and temperature occurred during the first days of wells operation; therefore, the recorded temperature were presented for the smaller time intervals for the first 365 days of operation.

5.2.1 **Fluid transfer**

The fluid transfer results by FEFLOW are the changes in hydraulic heads. At steady state, the hydraulic head was constant and equal to -10 m due to no flow conditions and no well operation. By commencing the wells' operation and pumping in the fluid, the pressure was increased at the surrounding nodes of the injection well, which led to an increase of the

hydraulic head. For the injection well, within the first 90 days of operation, the hydraulic head increased from -10 m to 96 m; then it decreased to 91 m with no further changes. The sharp changes during the first two months of the simulation demonstrated the instability of the system at the beginning of the operation. At the production well, the hydraulic head encountered a sharp drop to -540 m through the first 90 days. After 2 years it reached to the maximum hydraulic head of -428 m and after a short drop of 24 m became constant for the next 28 years (Fig. 5.2). Steady state hydraulic heads of 91 m and -451 m derived after 90 days of operation at the injection and the production wells. The difference between the hydraulic heads at the injection and the production well reached to approximately 544 m after 5 years.

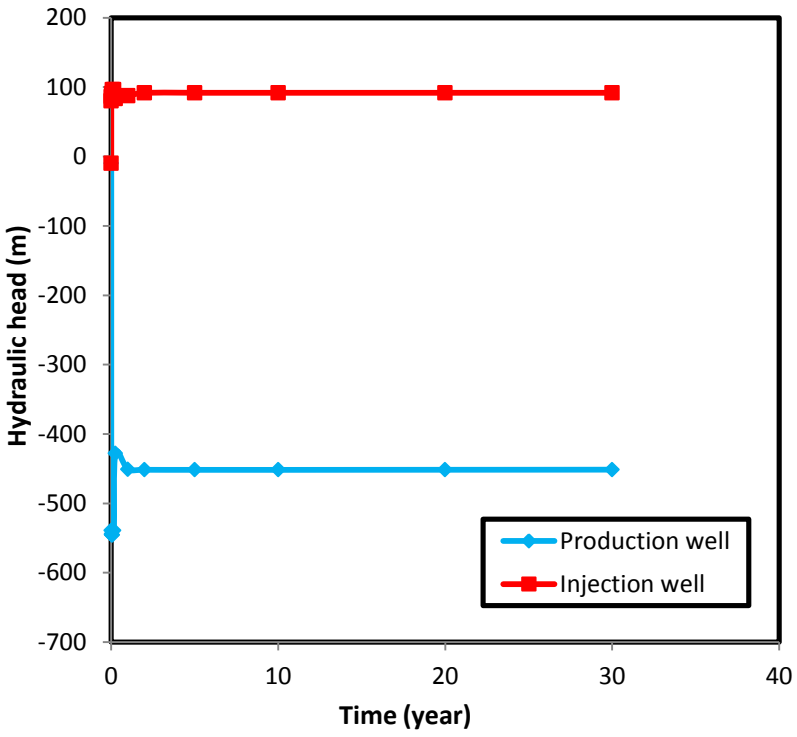

Fig. 5.2. Hydraulic head at the production and the injection wells for the Tilston site for 30 years of operation.

5.2.2 **Heat transfer**

Fluid flow along the injection well

The injection fluid was assumed to have a constant temperature of 15°C throughout the system's operation at the wellhead of the injection well. The temperature of the formations, from the surface to -138 m, was less than the injection fluid's temperature (15°C). Therefore, by injecting the warmer fluid, the fluid loss heat to warm the cooler formations and reached the minimum temperature of 12.9°C at a depth of 30 m after 30 days of operation. By stabilizing the system, the fluid's temperature increased to 14.54°C and became constant afterward. From the second layer to the bottom of the injection well (at the well screen's location), the formations' temperature were greater than the injected fluid and consequently led to increasing the fluid's temperature (Fig. 5.3). The fluid temperature increased to a maximum of 27.45°C at the first day of operation at the well screen; however, this temperature reduced to a temperature of 15°C from day 1 to day 90 and became constant for the rest of simulation.

After 30 years of operation, the fluid temperature at the well screen of the injection well reached to the minimum of 15°C, which is the same value as the injection fluid's temperature at the wellhead.

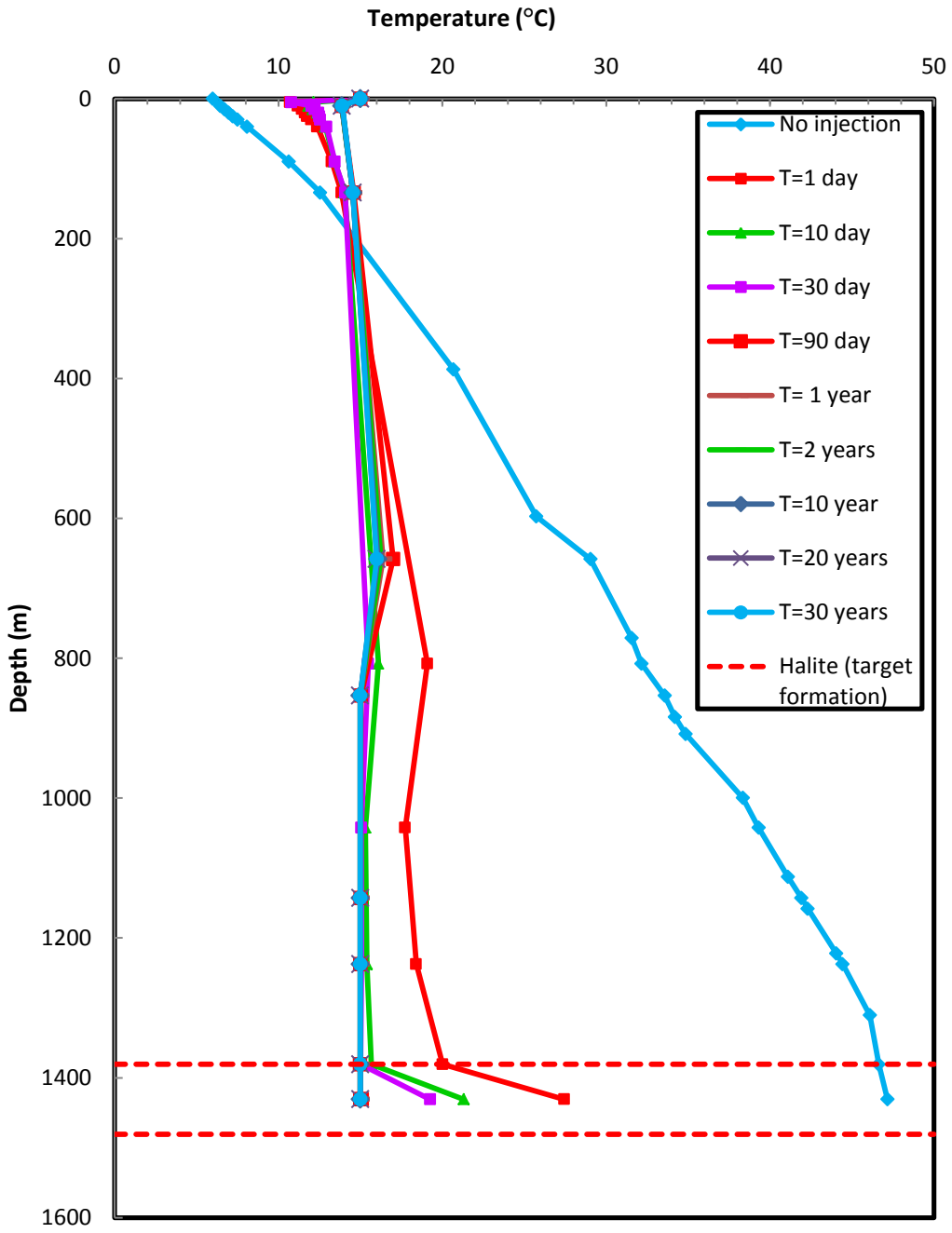

Fig. 5.3. Fluid temperatures along the injection well.

Reservoir thermal effect

Halite as the thermal reservoir had a temperature of 47.30°C. The higher temperature of halite, compared to the injected fluid (15°C) along with its identical thermal properties (low thermal resistance and high thermal conductivity), enhanced the temperature of the injected fluid on its path from the injection to the production well.

The fluid temperature at the injection well screen decreased from the maximum of 27.45°C to 15°C after 90 days of operation. The fluid absorbed heat on its path to the production well and reached the maximum temperature of 46.63°C within the first 90 days of wells operation. After 90 days of the operation, the injected fluid reached to the temperature of 47.28°C with no further changes (Fig. 5.4)

At the production well screen, the fluid's temperature dropped by 0.4°C within the starting time of the operation and then increased to a constant value of 47.28°C after 90 days of operation.

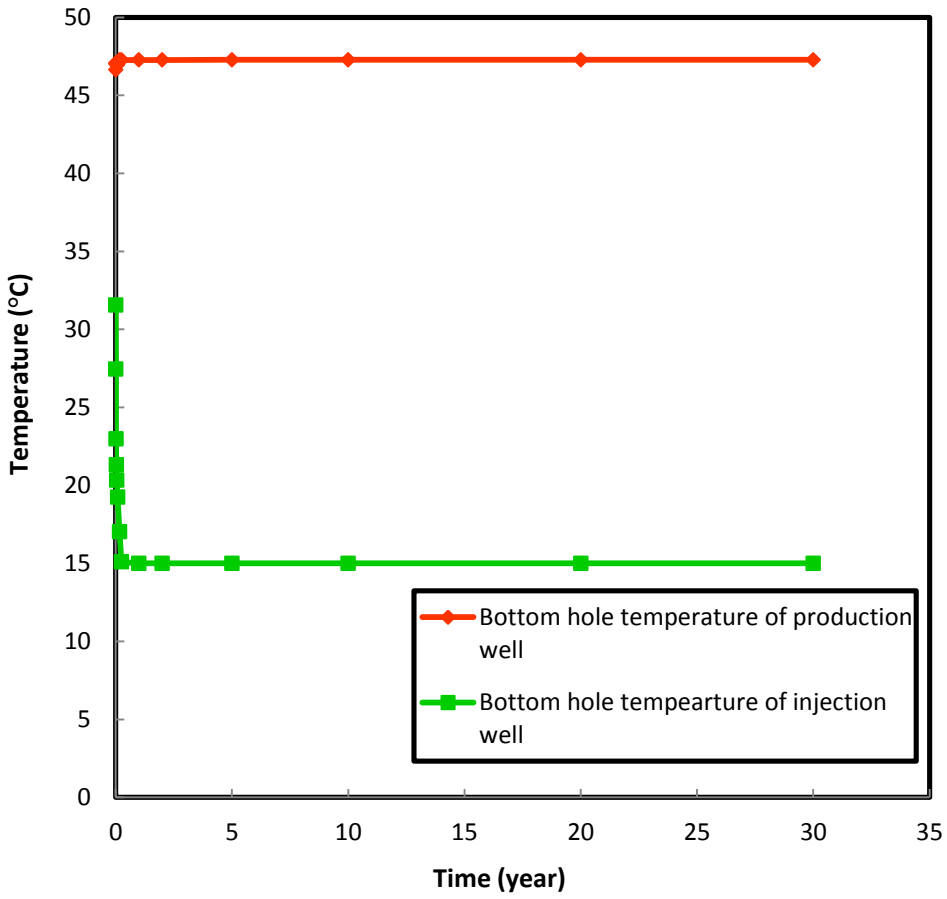

Fig. 5.4. Effect of the thermal reservoir on the fluid's temperature, from the injection to the production well.

Fluid temperature along the production well

The BC at the surface used a constant low temperature of 6°C and affected the simulation results within the first 5 m to 10 m of the surface. Therefore, to eradicate the effect of the boundary condition, the temperature at -10 m opted as the simulation result. Fig. 5.5 shows the temperature losses within the first 10 m of the surface with the maximum temperature loss of 12°C at 30th day of operation.

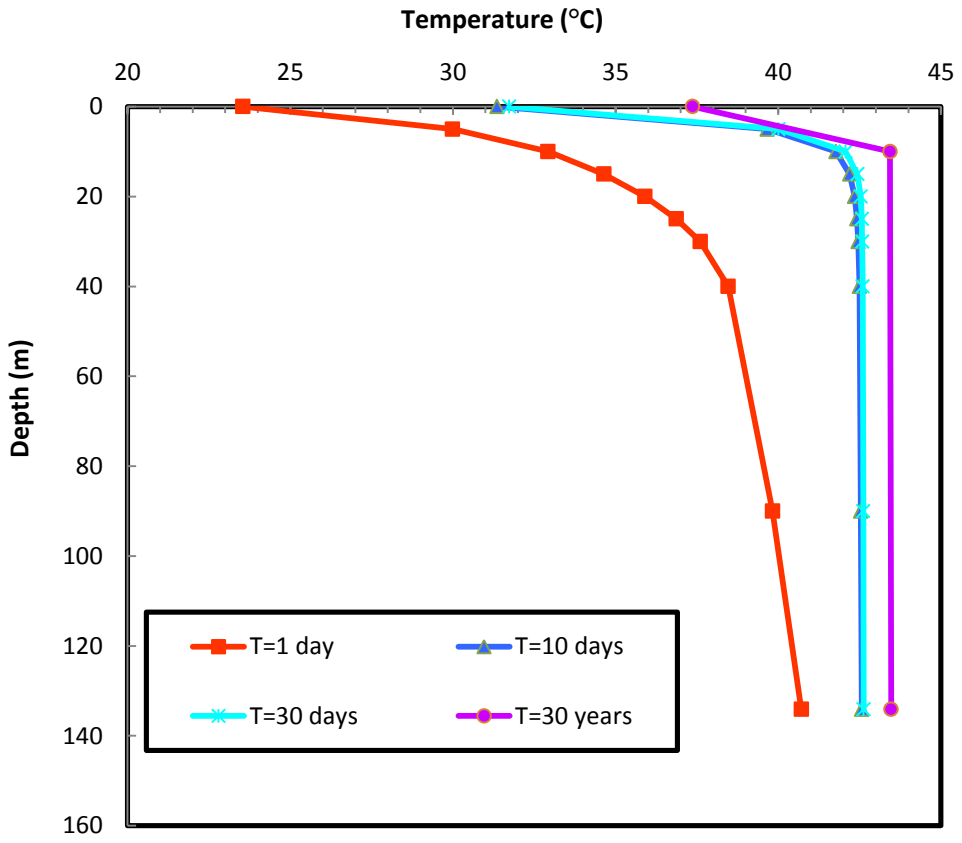

Fig. 5.5. Effect of atmospheric boundary condition on the simulated temperature of the production fluid at various simulation times.

The temperature of the fluid at the production well screen versus time is presented in Fig. 5.4. At the first day of operation, the fluid temperature reached to 46.97°C at the well screen of the production well. Due to temperature losses in the production well during the pumping phase, the fluid temperature reduced to a minimum of 32.92°C at a depth of 10 m below the wellhead, which showed a temperature loss of ~14°C. The heat loss along the well reduced with time and the temperature of the production fluid increased to 42.06°C within 30th day after the start of pumping. From day 30 to 365, the temperature losses decreased to 3.82°C (final derived temperature of 43.44°C) with no further alteration (Fig. 5.6).

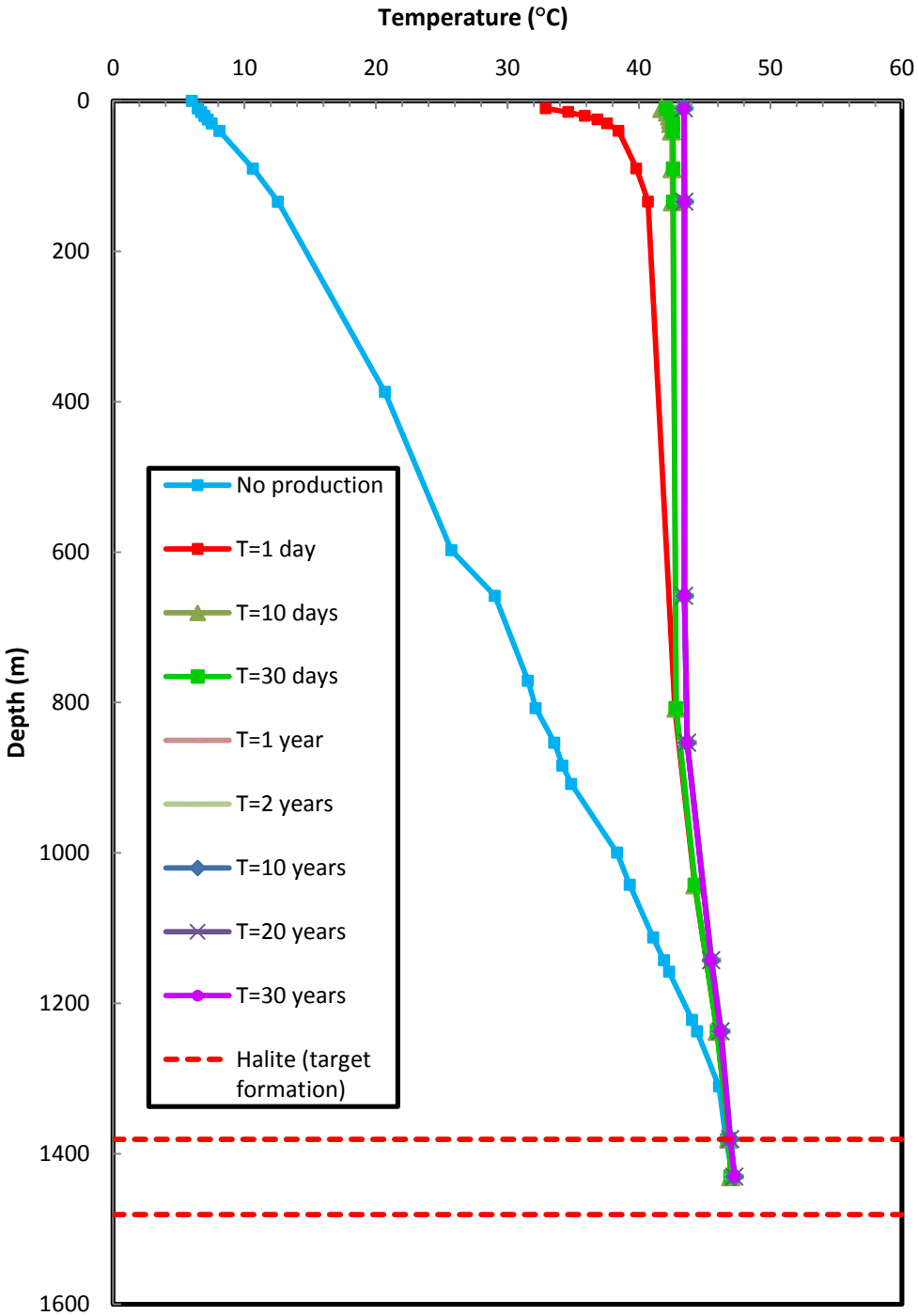

Fig. 5.6. Production fluid temperature log along the production well.

5.3 Steady state calibration, Generic model

The Generic model was introduced as an extension of Tilston model, with the same geological formations, hydraulic head and upper thermal BC, which was located in the Saskatchewan part of Williston Basin. The target formation was at a depth of 3 km having a thickness of 118 m. The method for estimation of the Generic site's temperature vs. depth was introduced in section 4.6. A thermal gradient of the Generic model based on the formations temperature was compared to the steady state simulation results with and without calibration using RMS method.

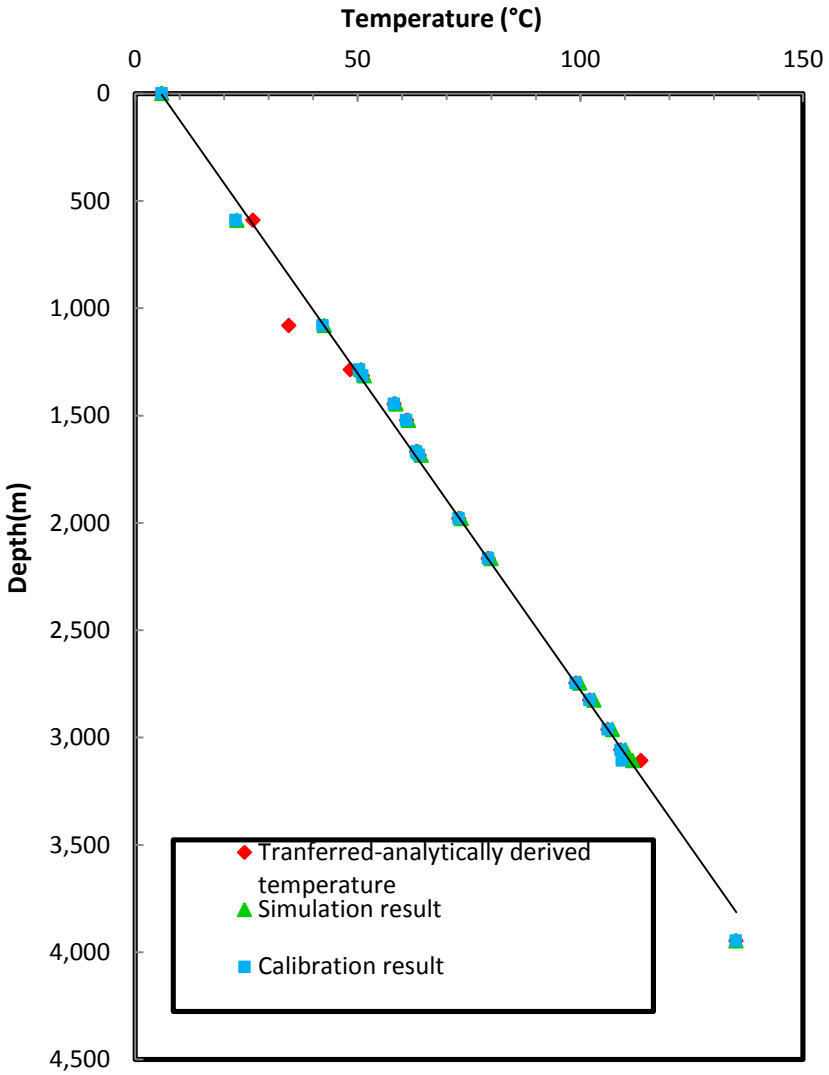

Fig. 5.7. Formations' temperature and simulation results for the Generic model located in Saskatchewan.

The total RMS before calibration was 0.00339 with the maximum error of 4.25E-5 and 1.12E-4 for the clay and shale formations (first and second layers) which are presented in Table 5.1. The thermal conductivities of these layers were the target of the calibration. The thermal conductivity of clay (layer 1) increased to 4.17 W/mK while it was altered to lower value of 2.0 W/mK for the shale (layer 2). The simulation results were improved, and the total RMS decreased to 0.00333.

Table 5.1. RMS values between the Generic model temperature data and simulation results without calibration.

Formations	Generic temperature gradient (°C/m)	Simulated temperature gradient (°C/m)	RMS
Clay	0.029	0.028	4.25E-05
Shale	0.018	0.018	1.13E-04
Shale	0.006	0.006	1.89E-05
Sandstone	0.001	0.001	1.47E-08
Shale	0.005	0.005	3.58E-06
Limestone	0.002	0.002	2.68E-08
Anhydrite	0.001	0.001	2.51E-06
Shale	0.000	0.000	2.93E-09
Anhydrite	0.005	0.005	1.72E-07
Dolomite	0.003	0.003	3.50E-08
Shale	0.007	0.007	5.30E-08
Limestone	0.001	0.001	2.61E-08
Limestone	0.001	0.001	1.97E-08
Dolomite	0.001	0.001	9.71E-09
Salt	0.001	0.000	3.60E-06
Dolomite	0.006	0.006	4.86E-07
Total RMS		0.00339	

The resulting temperature from the calibrated model is presented in Fig. 5.8. The temperature is increasing from top to the bottom of the model following the indicated isolines. The temperature of the reservoir showed 110°C.

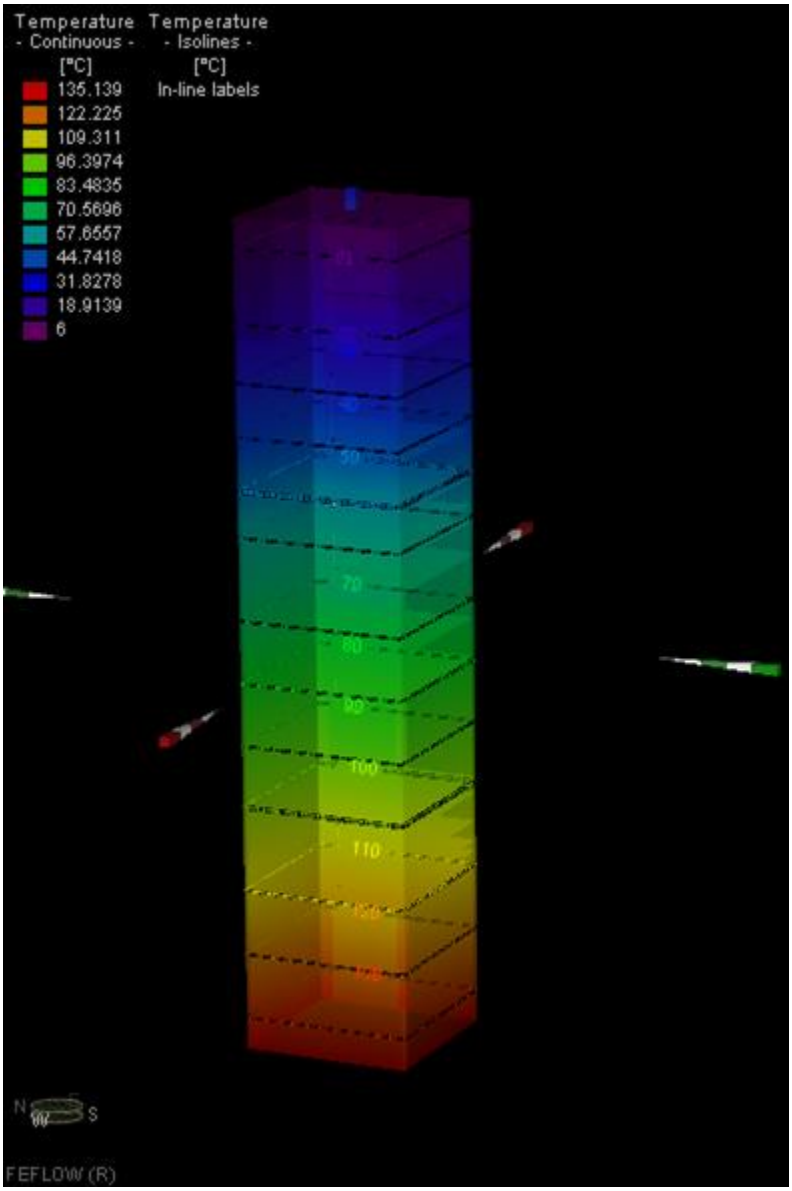

Fig. 5.8. 3D view of the Generic model showing temperatures along the domain.

5.4 Heat and fluid simulation results, Generic model

The results of the fluid and heat transfer simulations are presented in the following section. Results are given at 20 observation points in a distance of 0.93 m to the actual well location (at the neighboring nodes) and they are presented for reservoir lifetime of 30 years, similar to the Tilston site.

5.4.1 **Fluid transfer**

A constant hydraulic head of -10 m, same as Tilston site, was observed from the steady state simulation due to no flow condition. The injection of the fluid raised the hydraulic head, while pumping the fluid decreased the hydraulic head significantly. In the Generic model, injection of maximum 7000 m^3/day into the reservoir raised the hydraulic head to 0.52 m within the first hours of the operation, while at the production well the extraction of the same volume of the fluid led to a head drop of -116 m. By continuing the wells performance, the hydraulic head at filter screen of the injection well raised to the maximum of 0.74 m within the next 10 days and stayed constant. At the production well, the head was constantly dropping to -1730 m after 90 days and dropped to -2970 m by year 1. After first year of operation, the hydraulic head stayed constant at the production well screen. Fig. 5.9 demonstrates the hydraulic head rise and drop at the injection and the production wells screens through 30 years of simulation time.

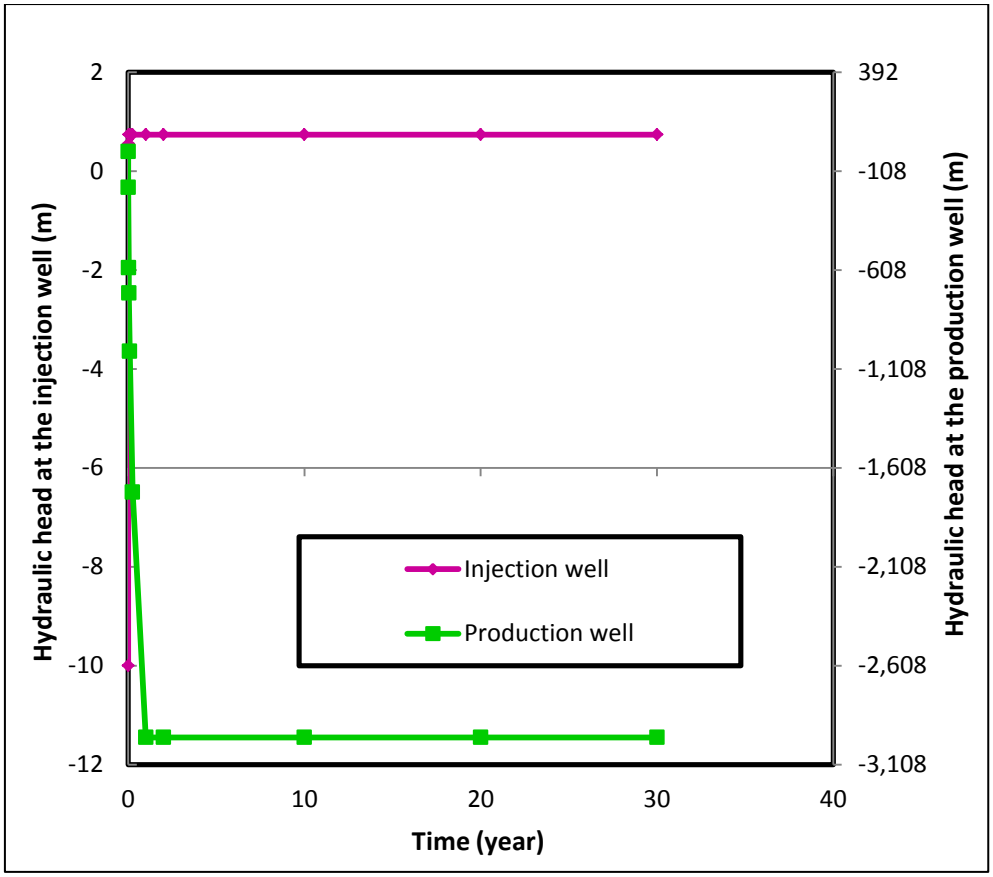

Fig. 5.9. Hydraulic head versus time for 30 years of operation at the injection and the production well screens.

5.4.2 **Heat transfer**

At the beginning of the operation, the temperature of the injected fluid increased from 15°C to 16.8°C within the first layer of the model (Fig. 5.10). The lower temperature of the injected fluid cooled the surrounding formations of the injection well throughout the simulation, which led to less heat absorption and consequently a reduction of the fluid's temperature (Fig. 5.10). After 10 years of operation, the fluid temperature reduced to 38.8°C, which decreased to 36.9°C in the next 10 years and became constant afterward. The fluid lost more temperature within the first year of the operation at the injection well screen than the upper formation. At day 1, the temperature of the fluid was 66.7°C at the upper layer of the well

screen and 66.5°C at the well screen location. This temperature difference increased to 0.8°C after 1 year of operation and decreased to zero through the next 9 years.

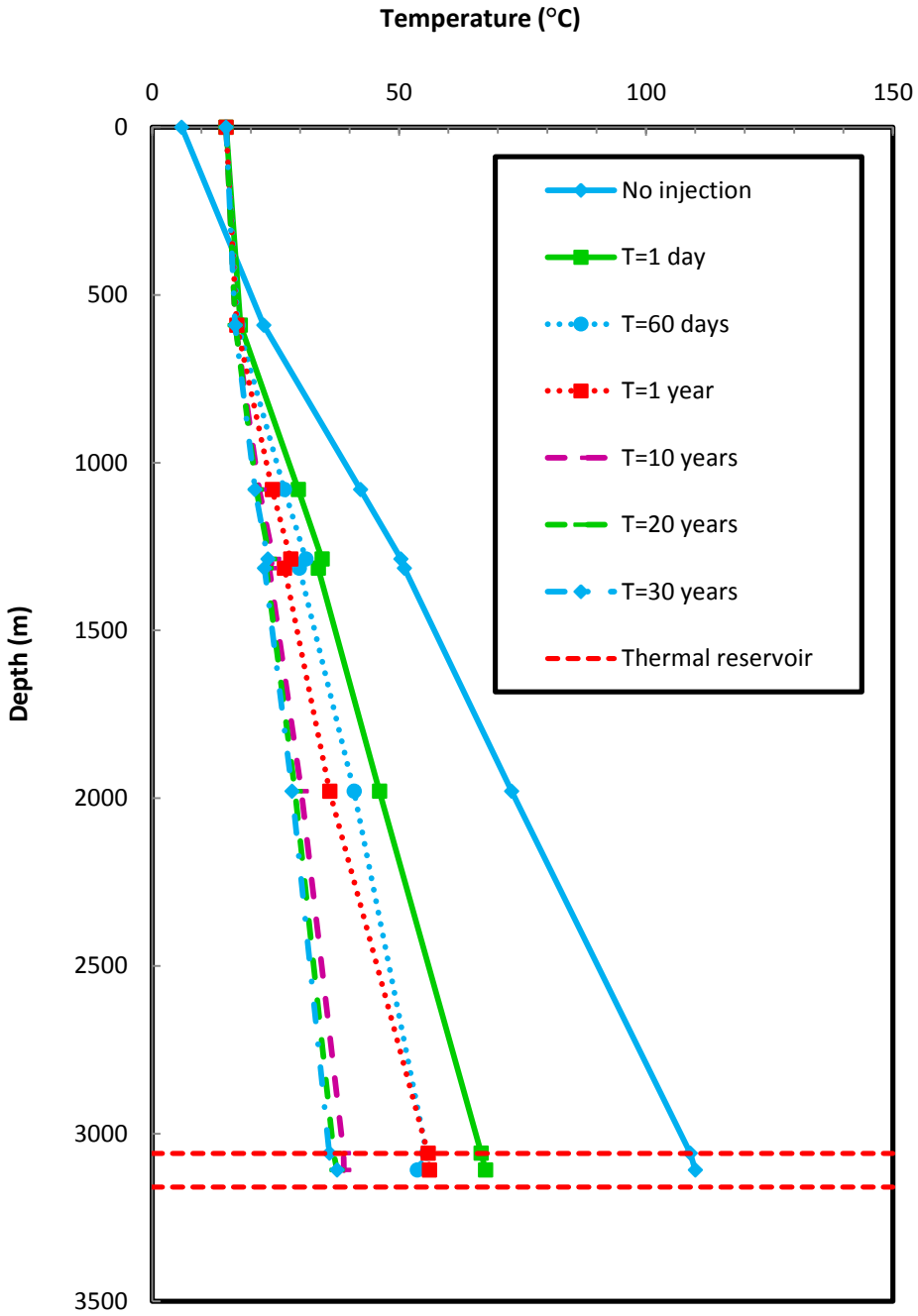

Fig. 5.10. Temperature log along the injection well in the Generic model.

The effect of the thermal reservoir in increasing the injected fluid temperature is shown in Fig. 5.11. The provided temperature logs are attributed to the production and the injection well screens for the lifetime of the reservoir. Through the first year of the operation, the temperature at the production well dropped from 110°C to 53°C due to injection of cold water and then increased to 108°C. Due to the increase of the injected fluid temperature, the production fluid temperature increased as well and became constant (110°C) after 2 years of the operation.

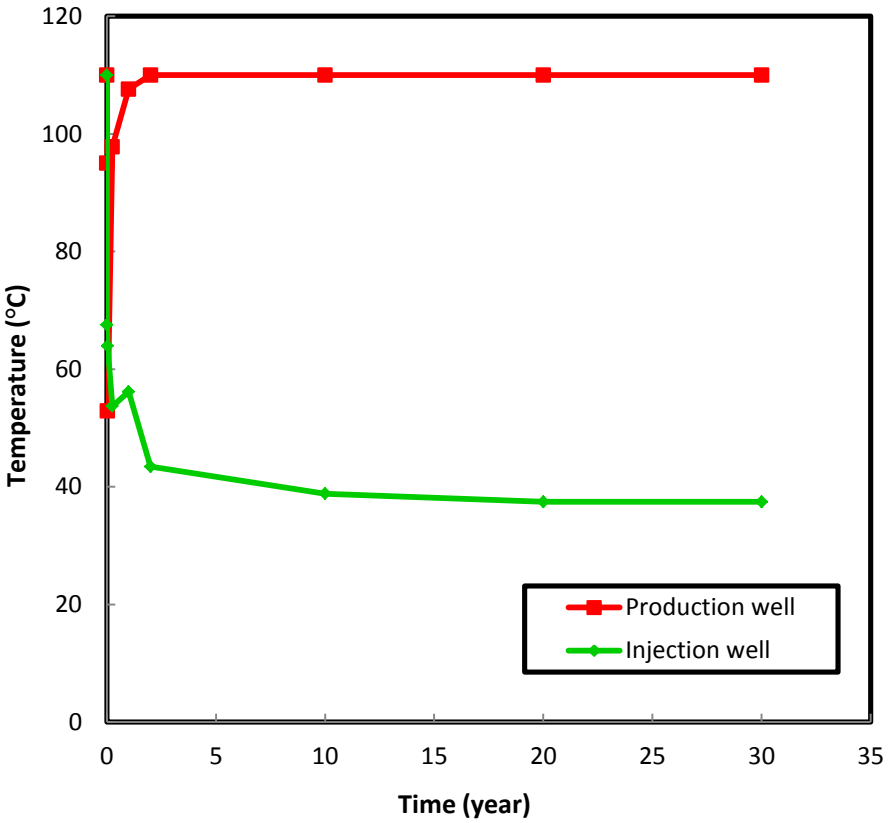

Fig. 5.11. Temperature along the fluid path from the injection to the production well in the thermal reservoir.

At the production well, the extracted fluid lost some portion of the absorbed heat along its path to the surface. This heat loss decreased due to an increase of the production well's surrounding temperature and the high temperature of the fluid at the production well screen. Fig. 5.12 represents the fluids temperature along the production well. A drop within the first 10 days of operation was observed due to pressure drop. The temperature increased from day 10 to 10 years of operation and stayed constant for all the formations. In the halite formation, the temperature increased from 53°C to 110°C and stayed constant with no further alteration. The final derived temperature at the surface within 0.45 m of the production wellhead was 70°C.

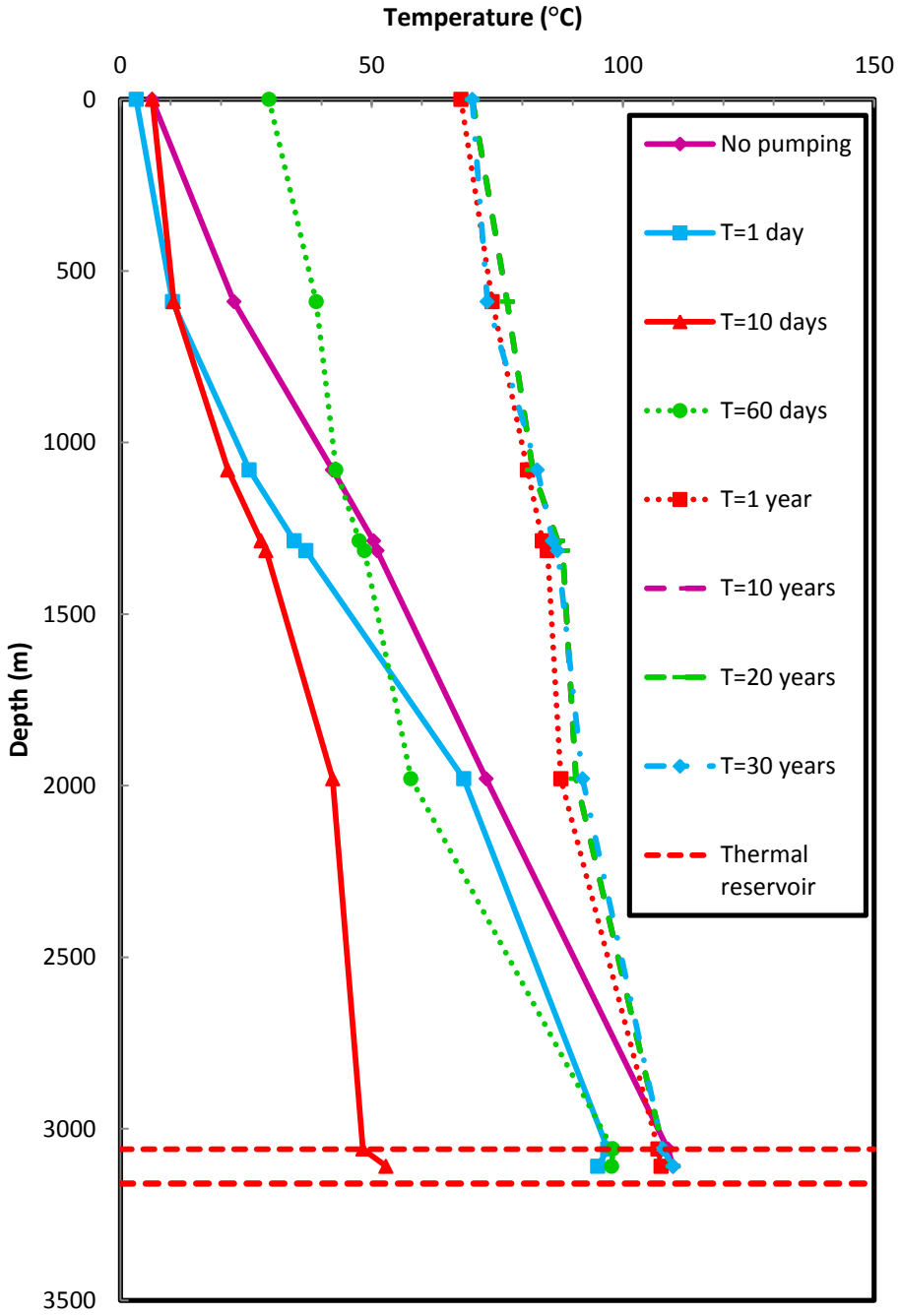

Fig. 5.12. Fluid temperature along the production well for 30 years.

The temperature was decreasing from the wellhead to the surrounding nodes where the observation points were located. At the surface of the model, the wellhead is surrounded by fixed temperature of 6°C, which led to a sharp reduction of the temperature from the wellhead to the neighboring nodes. The temperature at the wellhead of the production well through the simulation time is given in Fig. 5.13. After 2 years of the operation, the maximum temperature of 105°C was derived at the wellhead of the production well and became constant afterward.

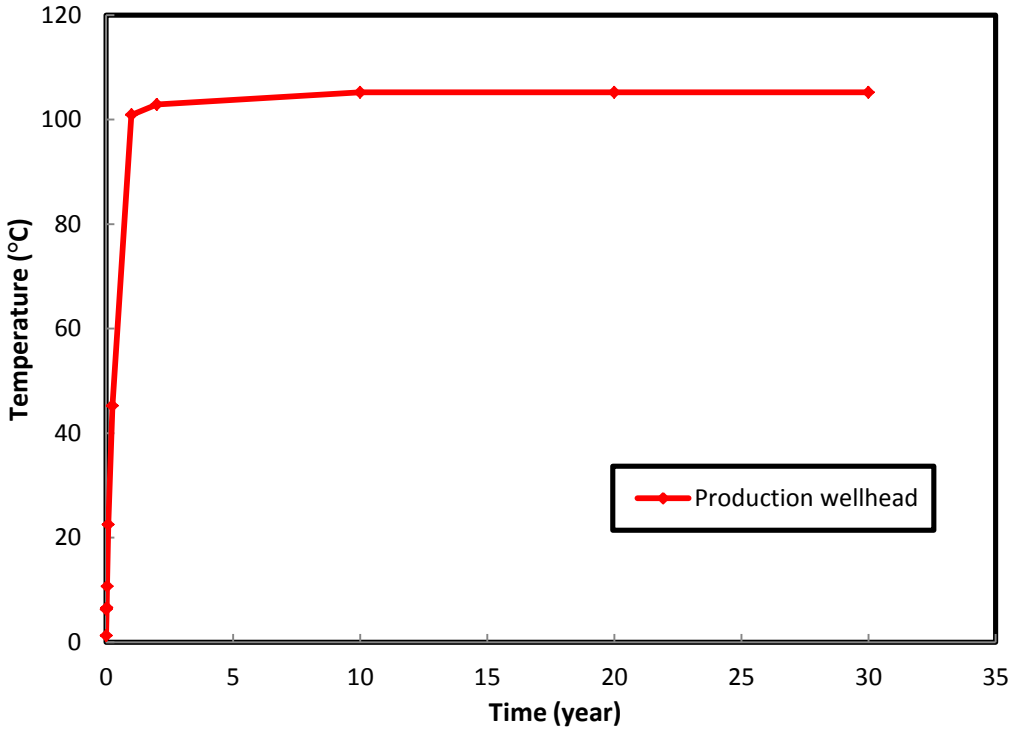

Fig. 5.13. Fluid temperature versus time at the production wellhead of the Generic model.

Chapter 6. Discussion

Overview

In the following section, the mesh consistency, hydraulic head changes, transferred heat along the wells and the reservoir as well as residency time, generated and lost energies, the impact of temperature on density and viscosity, the effect of halite as a thermal reservoir and thermal gradients within the formations being discussed.

6.1 Mesh consistency

The mesh size affected the accuracy of the simulation results significantly. Well distributed meshes, decreased the error of the simulation, specifically for simulation of the hydraulic head during the well performance. The wells operations resulted in the head drop at the production well and rise at the injection well. To determine the consistency of the meshes, the temperature of a selected node at 1.85 m of the injection and 1.66 m from the production wells at the top of the second layer (shale) and the reservoir were compared to the simulation results of a model with refined mesh system with 0.4 m element length. The current mesh was called M1 with an average element length of 0.93 m, and the refined mesh was called M2. The comparison was carried out for the first 3 years of operation due to the higher instability of the system. Table 6.1 shows the comparison between the mentioned nodes' temperatures for M1 and M2. As it can be deduced, the temperatures for both models with various mesh sizes were approximately the same, which approved the consistency of the mesh and accuracy of the results. The highest difference of ~1°C was attributed to the production well's temperature at the reservoir due to severe pressure changes. The error between the fluid temperature at the wellhead of the injection well was 0°C at the first day of operation and the maximum error at this point was 0.01°C. The finer mesh distribution (M2) led to a higher temperature for the fluid at production well screen; however, the temperature differences decreased by time. Thus, the defined mesh was well distributed which consequently led to accurate estimation of the temperature and minimized the simulation error considering the wells operation.

Table 6.1. Hydraulic head and temperature at 1.86 m from the injection and production wells at the top of the second formation of the Generic model.

			T= 1 day	T= 10 days	T= 30 days	T= 60 days	T= 90 days	T= 1 year	T= 2 years	T= 3 years
		Depth (m)	Temperature (°C)	Temperature (°C)	Temperature (°C)	Temperature (°C)	Temperature (°C)	Temperature (°C)	Temperature (°C)	Temperature (°C)
M1	Injection well	590	22.58	22.08	21.48	21.16	21.00	20.56	20.37	20.29
		3108	108.53	98.79	88.35	82.27	77.97	69.88	65.72	64.07
	Production well	590	22.49	21.51	22.72	23.35	24.01	24.99	25.15	25.19
		3108	108.08	94.43	89.19	98.93	104.94	105.01	105.01	105.01
M2	Injection well	590	22.58	22.07	21.48	21.16	20.90	20.55	20.38	20.29
		3108	108.53	98.51	88.31	82.24	76.97	69.59	65.66	63.99
	Production well	590	22.57	22.07	22.82	23.56	24.1	24.58	24.72	24.78
		3108	108.51	95.72	90.19	99.35	105.89	105.89	105.89	105.89

6.2 Hydraulic head and temperature change along the wells

Hydraulic head changes occurred due to wells performance. The wells operation versus time was categorized into three phases from unstable to stable condition.

- Phase 1 (starting phase) is the start-up condition when the wells started operating (between 6 hours to 1 day). Sharp changes in head and temperature were observed within this phase at both injection and production wells.
- Phase 2 (developing phase) is the developing condition, which the injection rate and production rate varied in each time step to achieve the stable condition.
- Phase 3 (stable phase) is the stable condition in which the hydraulic or temperature values are constant with time.

The strong changes in hydraulic head and temperatures observed in phases 1 and 2 were not related to oscillation errors as shown by the mesh consistency. Additionally, the initial time steps had been selected small enough, (1E-6 day for phase 1 and 1E-4 day for phases 2 and 3) to eradicate the probability of the oscillation error. Therefore, the hydraulic head changes within the first years of the production and the injection wells were the results of the instability of geothermal system and not of the numerical simulation.

In phase 1, sharp changes of hydraulic head and the temperature was observed at the production well and injection well screens. The hydraulic head dropped to -530 m and -116 m at production well screen and the temperature reduced to 27.45 and 67.5°C at the injection well screens for Tilston and Generic models during the phase 1.

The first day of the operation or initially start-up phase led to a decrease the fluid temperature from 15 to 13.98°C at the first 10 m depth (for Tilston) and slight increase along the rest of the formations. The sudden decrease of the fluid temperature is due to a larger temperature of the fluid comparing to the surrounding formations. At a depth of 800 m, the observed temperature was ~2°C larger than the below formation which was due to the location of the observation point. The nodes distances from the wells varied from 0.93 to 1 m, which led to small recorded temperature anomalies. The observation points located closer to the injection well, recorded a lower temperature than the ones with further distance due to less heat gain. In phase 2, the injection and pumping rates were varying to stabilize the system. The injection rate increased gradually after the 1st day of operation and reached to the maximum of 91 m after 2 years, which showed the consistent rate of the fluid's injection to the reservoir at Tilston site. At the production well screen, the pumping rate was constant from day 1 to day 30 and decreased within the next 60 days. The pumping rate reduction led to an increase of the hydraulic head at the well screen to -428 m. The higher thermal conductivity and lower thermal resistance of the reservoir was observed for the recorded temperatures of day 10 and 30 (Fig. 5.6). The temperature of the fluid is increased for 6°C and 4°C at the well screen of the injection well. The heat transfer between the warmer fluid in the first 200 m and cooler fluid from 200 to 1430 m with the surrounding formations became constant in phase 3 by increasing the pumping and injection rates after 90 days of operation. At phase 3, the constant temperature of 15°C was derived at the injection well screen from 90 days to 30 years of the operation.

In the Generic model, the hydraulic head reduction occurred smoothly at the production well screen and skipped the sharp changes of phase 1 due to finer mesh distribution at the wells locations. The temperature of the injected fluid was more than the formations' temperature

for the first 400 m at phase 1, phase 2, and phase3. The temperature of the fluid was constantly increasing after 400m and reached the maximum of 67.5°C in the thermal reservoir in phase 1. Phase 2 occurred within the first 2 years of the operation for the production well and first 10 days for the injection well. The finer spatial distribution for the Tilston model comparing to the Generic model led to faster convergence for the Generic model. The heat transfer between the injected fluid and the formations continued in phase 2 and phase 3 for 10 years. The formations' temperature was decreasing due to the injection of the cooler fluid in each time step. The heat transfer between the fluid and the formations became constant due to a constant pumping rate and injection rate in phase 3 after 10 and 20 years of operation with the lowest temperature of 36.9°C, which was almost double the injected fluid's temperature. The temperature of the injected fluid at 1400 m for the Tilston model was 15°C after 30 years of operation and ~32°C for the Generic model. It was deduced that the thermal gradient at the Generic site was slightly higher than the Tilston site.

In addition to the well operation, the hydraulic fractures influenced the hydraulic conductivity and consequently the hydraulic head of the reservoir (containing the well screens) as well. Based on Darcy's law, the head drop was decreased by increasing the hydraulic conductivity of the reservoir. The hydraulic head dropped within an empirical area of the fractured part of the reservoir. In phase 1, the head dropped from -10 to -80 m at a distance of 3.59 m from the production well and decreased to -116 m at the well's location. Within phase 2, by increasing the head drop at the production well, the empirical area diameter expanded from 3.59 m from the production well to 98 m (at day 90) with the highest and the lowest heads of -175 m and -1760 m from the perimeter of the area to the production well as shown in Fig. 6.1. The maximum diameter of the fractures with dropped hydraulic head was 85 m, which was observed after 10 years of operation and became constant afterward. The large hydraulic

conductivity of the fractured area led to developing the empirical area with a lower conductivity that consequently resulted into smooth hydraulic head reduction and diminished the instability of the wells system.

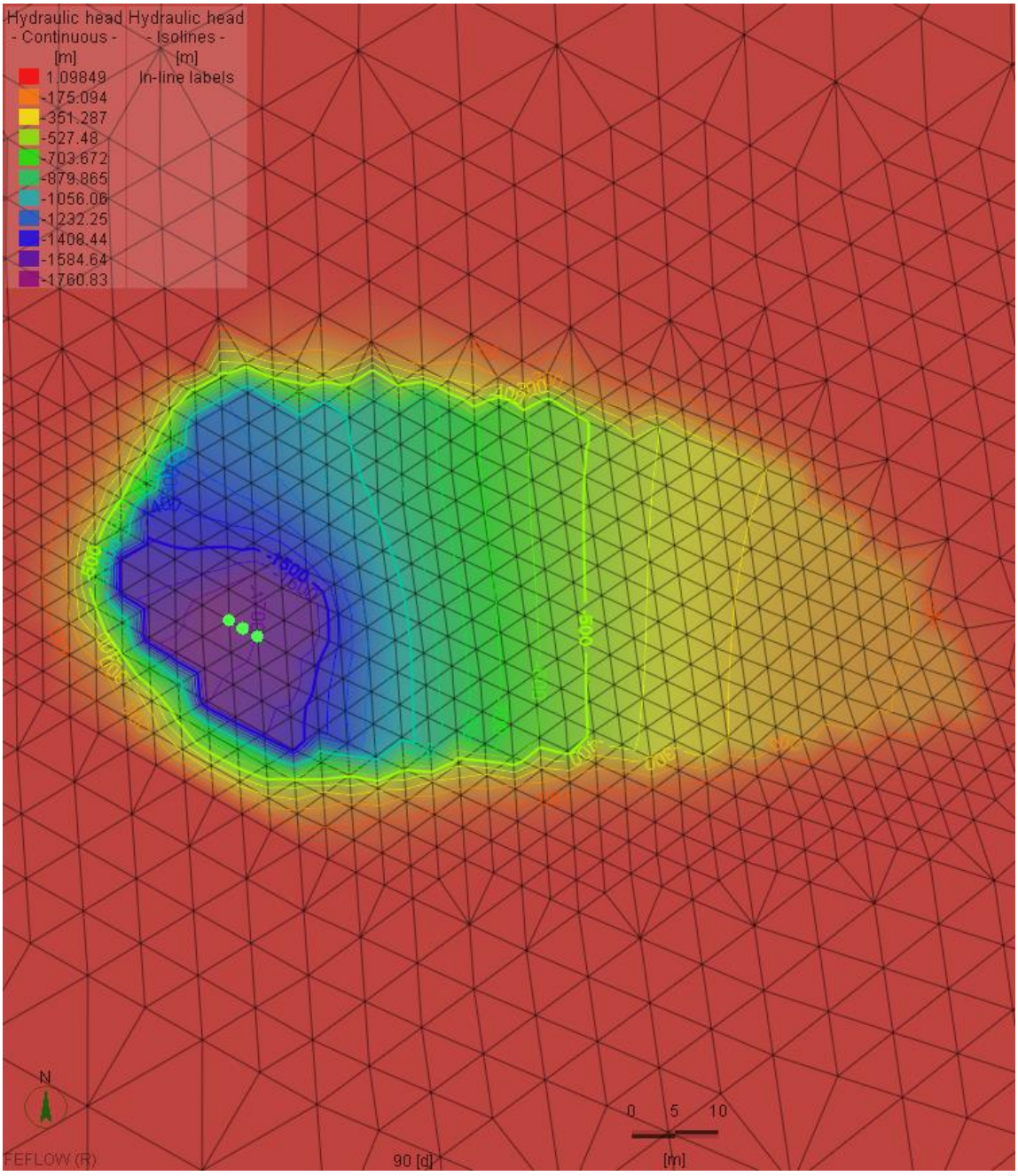

Fig. 6.1. The hydraulic head drops within the fractured area of the reservoir at 90th day of the wells operation.

6.3 Pressure changes in the target formation

The range of pressure rise and drop due to the well operation was introduced in section 4.4. In phase 1, the sharp changes of the pressure occurred due to commence of the injection and extraction of the fluid. The simulation results showed the hydraulic head drop of 500 m for the Tilston and 2970 m for the Generic model at the production wells screens, which led to the pressure drop of 5.5 MPa and 32.67 MPa respectively. The allowed pressure drop for the wells considering the proposed permeability of the reservoir was 0.5 GPa for both sites, which was greater than the maximum drop at the Generic model. The main concern related to the pressure drop was the temperature drop and phase changes at the production well. By dropping the pressure, temperature decreased as well and resulted in a low thermal efficiency of the geothermal system. At the injection wells, the pressure rises were within the acceptable calculated range by showing the maximum increase of ~1 MPa at the Tilston site.

6.4 Heat transfer- Calibration

The temperature data for calibration of the simulation result was the combination of the actual measured temperatures for the first 1200 m and the analytically derived temperature with Eq.3. Although this method was the only way to estimate the temperature of the deep formations, it could not replace the measured data in the sedimentary basins with the same accuracy. In order to limit the error of estimating temperature, the Craton formation opted as the most similar formation to the WCSB for this research. This limitation increased the probability of inaccuracy in the temperature estimation.

At the Tilston site, the simulation results showed a larger estimated temperatures comparing to the measured temperature from 1100 to 1300 m depth, where layers of mainly dolomite and limestone exist. The thermal conductivity of these formations were 4.2 and 2.8 W/mK at ambient condition respectively. The error of the similartion was diminished by decreasing the thermal conductivity of dolomite to 3.1 W/mK. The effective thermal conductivity of limestone depended on the temperature and change of the thermal conductivity at ambient condition did not change the final value. In addition of the limestone and dolomite, the thermal conductivities of anhydrite and shale as main components of formations at depths of 853 m and 884 m were decreased and increased respectively to decrease the simulation error within the first few layers.

The maximum error was at 1200 m due to the substitution of the measured data with the analytical method temperatures. The error within the first 1200 m at Tilston was less than the deeper formations associated with the analytically estimated temperature. As shown in Fig. 5.1, the calibration results were highly compatible with the measured temperatures. This is

due to the assumptions, which were made for estimating the thermal parameters for Eq.3. Therefore, it can be deduced that the calibration results of the models are more reliable compared to the analytical estimations.

For the Generic model, due to the formations similarity with Tilston site and lack of information regarding the measured temperature, it was assumed that the same temperature was derived in the Saskatchewan part of the Williston Basin within the first 1200 m (for clay and shale formations) and for the formations below this depth, Eq.3 was used. The combination of the Tilston measured temperature (transferred data) and Eq.3 used for calibration of the Generic model. The errors between the transferred and the simulated temperatures for the first 1200 m layers had the largest values. E.g for the Generic model at a depth of 590 m the formation consisted of clay; however, for the Tilston site at the same depth the formations main components were clay and shale. Different components led to different thermal conductivity and thermal resistance, which increased the inaccuracy between the transferred and simulated temperature. Thermal conductivity of the first 590 m of the Generic site was assumed to be 1.64 W/mK (clay); however, for Tilston the first 138 m was 1.64 W/mK (clay) and the next 362 m was 2 W/mK (shale). Therefore, by increasing the effective thermal conductivity of the first 590 m in the Generic model to 4.17 W/mK, the error was diminished. The calibrated Generic model represented comprehensive accurate and more reliable temperatures in Saskatchewan part of the basin than derived from Eq.3 due to its specific design for the Williston Basin and its geological formations.

6.5 Heat transfer within thermal reservoir

The recorded temperature of the fluid at the production well screen of the Tilston site was 47°C, equal to the thermal reservoir's temperature, regardless of the injected fluid's temperature to the reservoir for all phases. The lowest fluid temperature was 15°C (phase 3) which reached to the maximum of 47°C in 540 m distance from the injection on its way to the production well. No significant pressure drop was observed at the pumping well screen through phase 1 and 2; however, the well distance can be optimized.

The maximum heat provided from the reservoir at the Tilston site increased the fluid temperature to 32°C. Assuming the design flow rate of 7000 m^3/day and the temperature in combination with Eq.28, this heat could provide enough energy for a 10 MW power plant. The maximum capacity of the Generic model's thermal reservoir was 25 MW, considering the designed flow rate and temperature increase of 74°C for the injected fluid through the reservoir in phase 3. This capacity is 2.5 times larger than the maximum capacity of the DEEP project (section 2.2.4) which is underway in Saskatchewan at this moment. This states the efficiency of a geothermal system targeting the Prairie Evaporate very well. The fractures within the thermal reservoir increased the hydraulic conductivity of the formations that increased the fluid's transport pace from the injection to the production well location. The fluid absorbed heat within the first few meters of its path from the injection to the production well rapidly and reach to the reservoir's temperature due to high thermal conductivity of the halite (5.6 W/mK). However, the required time for the fluid to reach the reservoir's temperature increased with time due to the growth of the cooler zones around the injection well. As shown in Fig. 5.10, the temperature of the injected fluid was lower in the fractured

zone (well screen) than its upper formation in phase 2 due to the faster extension of the cooler zone in the fractured area than outside of the fractured zone.

At the Tilston site, the maximum temperature loss of 23°C occurred in the production well in phase 1. The fluid's temperature drop of 6°C from the target formation to the bottom of the first formation and the sharp drop of almost 17°C occurred at 138 m depth to the surface. This temperature loss provided enough energy for 5 MW electricity generation using the design flow rate. This amount equals the expected energy capacity of the DEEP project in Saskatchewan (section 2.2.4). Since DEEP targets a formation at 3 km depth, this attempt to target the Prairie Evaporate supplies the same energy at a depth of 1400 m. By considering the thermal conductivity of 0.54 W/mK and ΔT = 17°C, the heat flux within the 138 m of the formation (first layer with the highest temperature loss) was calculated as 9.18 W/m. The appropriate time for the fluid to lose 17°C considering the mentioned heat flux was 16 hours, which is 500 times more than the required time for the design flow rate to be pumped out from the reservoir. Therefore, the temperature reduction was simulated by FEFLOW was overestimated. The overestimation of the temperature reduction was due to an BC effect, which is discussed in section 6.6.

The temperature at 10 m depth was assumed to be the final derived temperature at the Tilston site section (5.2.2). The final derived temperature of the simulation in phase 3 was 43°C. The maximum temperature of 32°C was achieved after 1 day, which showed temperature loss of 14°C considering the bottom hole temperature of 47°C. By increasing the temperature of the bottom hole to 47°C (at 90 days), the temperature of the wellhead increased as well and reached to 43°C with ~4°C temperature loss. The wellhead temperature increased slightly to 43°C after 1 year and stayed constant afterward (Fig. 6.2). The heat loss reduction was due to the creation of higher temperature plumes around the production well in phases 2 and 3. The

plumes size increased from the well screen to the wellhead of the production well along the simulation time.

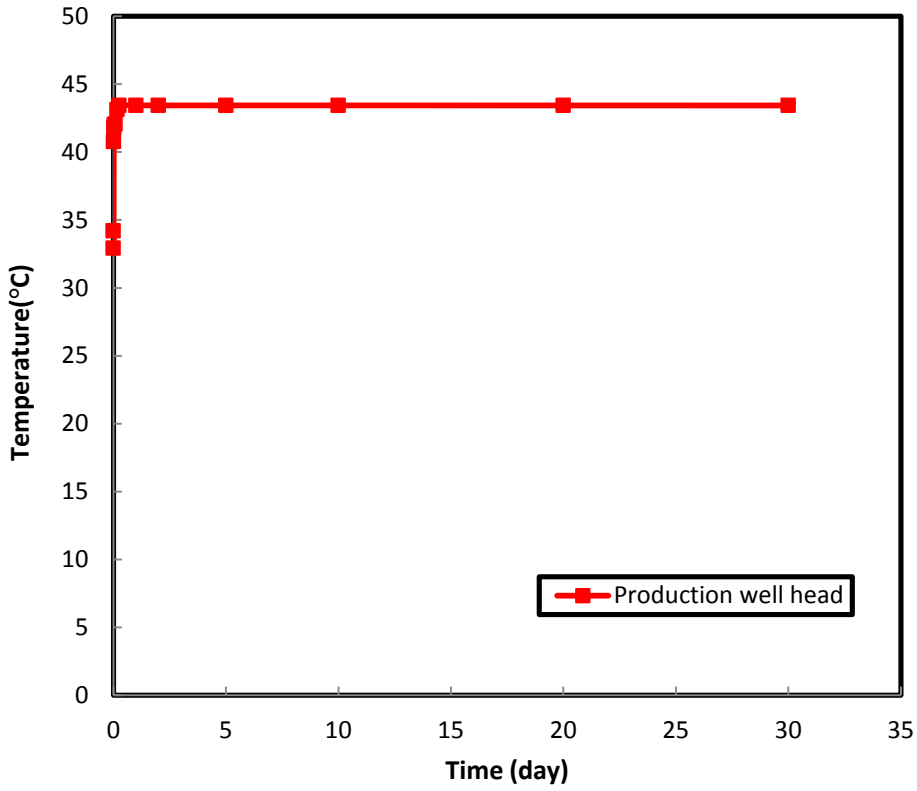

Fig. 6.2. The fluid temperature at the wellhead of the production well at the Tilston site.

The maximum temperature of 105°C was observed in the 2nd year of operation in the Generic Model. Similar to the Tilston site, the temperature loss decreased with time due to higher temperature zones around the well log. For example, at 590 m depth, the horizontal temperature gradient was 23°C/m after one year of operation and 17°C/m at 30 years of operation with almost 90°C at the production well. As presented in Fig. 5.11, the temperature increased after 10 days of operation after a sharp reduction to the maximum of 110°C (year 2) and then transferred to constant behaviour in phase 3. The higher duration of phase 2 of the Generic model in comparison to the Tilston model was due to the larger hydraulic head drop

in the Generic model, which was approximately 5 times of the Tilston site, which led to a strong reduction of the temperature within the first 10 days of the operation.

6.6 Heat transfer- BC effects

The temperature was strongly reduced within the first 10 m depth from the surface of the Tilston site due to the effect of BC on the simulation results (Fig. 5.5). The fluid had high pressure and temperature at the production well screen. By pumping the fluid, pressure dropped due to friction which led to temperature loss. However, the fluid temperature was still higher than the formations surrounding the production well, which increased the formations temperature consequently. Theoretically, by increasing the formations' temperature, the temperature loss will be reduced, and fluid with higher temperature will be derived at the surface. However, at the surface of the model constant temperature of 6°C was embracing the wellhead. The constant temperature BC was applied to each node of the surface; therefore, the low BC temperature was found at 1-2 m distance from the wellhead and induced a large heat flow from the borehole node to the neighboring nodes. At the first day of the operation, the fluid at the depth of 10 m had 30°C, which reduced to 23°C at the surface. By increasing the fluid's temperature, the effect of upper BC became more significant. At 30 years of operation, 6°C temperature difference was observed at the first 10 m depth that was almost twice as the temperature loss from the well screen to 10 m depth.

Besides, the constant hydraulic head BC at the top of the model restricted any flow at the upper bound of the model. Therefore, the fluid's temperature encountered a sharp temperature loss due to pressure loss and head drop. Eight sublayers had been used to represent the first geological layer at the Tilston site in order to minimize the effects of BCs. The average heat loss in the pumping well was 0.002°C/m by considering the fluid temperature at 10 m depth and 0.007°C/m at the surface. By selecting the final temperature at

a depth of 10 m temperature maximum error 0.05°C was accepted. This potential error was much smaller than the final derived temperature from the production well. Thus, determining the final derived temperature at a depth of 10 m instead directly at the surface resulted in negligible errors and strongly reduced the computation times. However, the accuracy of the simulation results was increased using multiple sublayers; the computational time increased incrementally.

In the Generic model, instead of using sublayers, isolines have been applied to the model, which showed the temperature reduction from the wellhead to the surrounding area and the original temperature at the wellhead was observed and reported as final temperature.

6.7 Effect of nonlinear density and variable viscosity

The simulation results of the Tilston model was obtained by considering the constant viscosity and linear density-temperature function due to the low temperature difference between the maximum and minimum temperature of the injected fluid. At Tilston, based in Fig. 3.7 for fresh water, the above assumption was accurate enough considering the minimum effect of temperature on the density and viscosity variation. The underestimation of density would be maximum 1.08 kg/m^3 that equals 0.11% and the overestimation of viscosity would be 74.73 µN-m^2/s that equals 9.56%.

The adaptability of this assumption for the Generic model was examined due to the higher range of temperature variations. Fig. 6.3 demonstrates the derived temperature at the well screen of the injection well at Generic model using constant viscosity-linear density and variable viscosity-nonlinear density. Heat transfer for specific fluid is a function of fluid flow rate, volumetric heat capacity, and temperature variation. If the density of the fluid decreases, considering the constant values for all other parameters, the temperature difference will be increased. As shown in Fig. 4.2, the density-temperature graph was divided into three sections. From 0-20°C, the nonlinear density showed smaller values comparing to the linear function, which led to higher temperature absorption from the surrounding formations. From 20-80°C, the linear calculated density was smaller than the nonlinear calculated density with a maximum difference of 2 kg/m^3 at 38°C. At the last section, the density of nonlinear function was lower than the linear calculated density with a maximum difference of 6.32 kg/m^3 at 100°C. Therefore, the fluid's temperature was higher at the injection well screen of the nonlinear calculated density than linear calculated density as shown in Fig. 6.3. The

temperature difference between the injected fluid at the well screen of the injection well, with and without considering the effect of temperature on density and viscosity, was almost 30°C within first two years of operation that showed the higher rate of temperature absorption for the model with temperature effect.

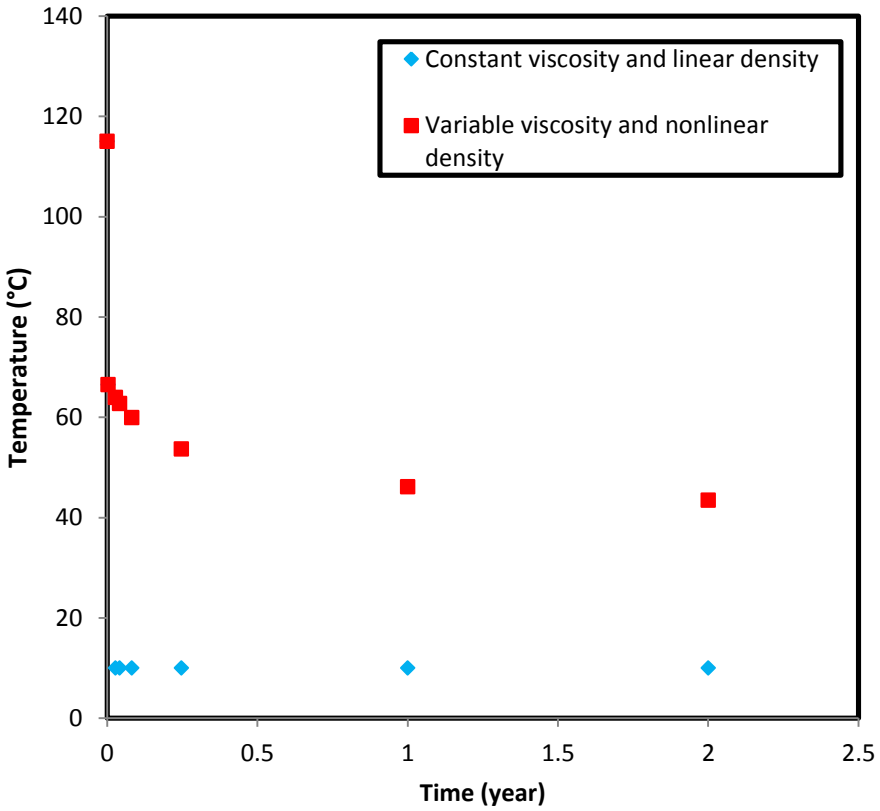

Fig. 6.3. Fluid temperature at the well screen of the injection well in the Generic model using constant and variable density and viscosity.

The viscosity mainly affected the pressure or head drop along the wells. Lower viscosity led to less pressure or hydraulic head drop and increased the final derive temperature. The final temperature at the production wellhead with the constant viscosity of 0.00108 N-s/m^2 and linear calculated density was compared to the final derived temperature of variable viscosity and nonlinear calculated density in Fig. 6.4.

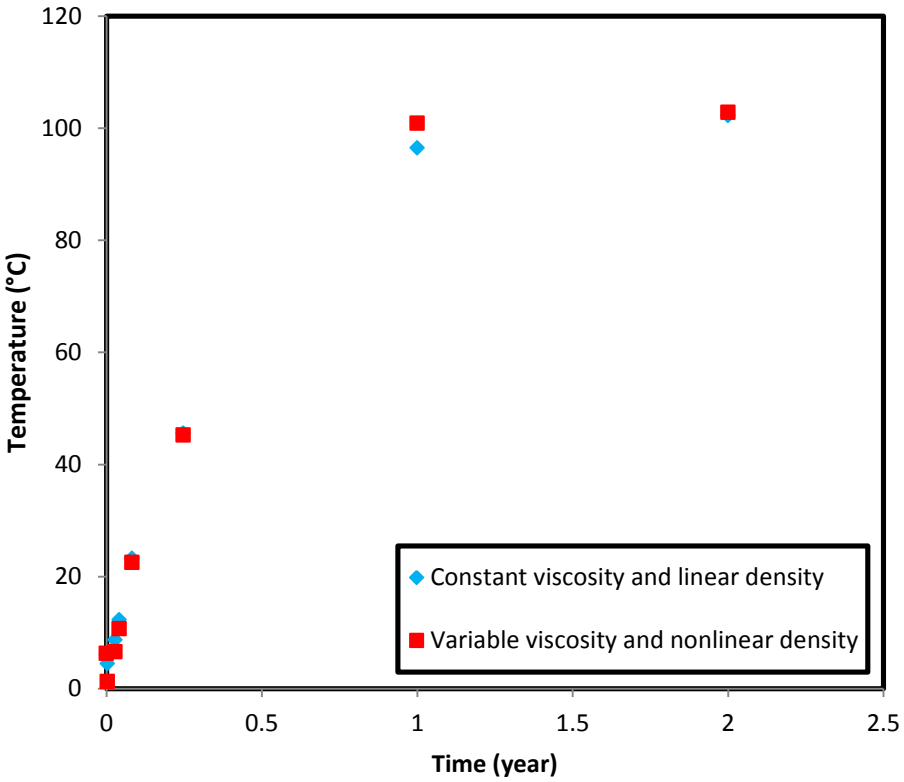

Fig. 6.4. The temperature of the fluid at the wellhead of the production well, for the Generic model in phase 2 (developing phase).

The effect of variable viscosity was observed mostly within 0.5 to 2 years of operation. The production fluid reached to 100°C after 1 year of operation; however, the temperature from the model with the fluid's constant viscosity was 96°C.

Based on the observations, the constant viscosity and variable density cannot be used for the simulation with high temperature differences. Additionally, the above figures demonstrated the higher efficiency of the system by considering the temperature effect on density and viscosity than the other model.

6.8 Halite as thermal reservoir

It was assumed that the lower thermal resistance and higher thermal conductivity of halite within Prairie Evaporite increase the efficiency of the geothermal system by providing higher temperature and lower heat loss. The lower thermal gradient was the results of less temperature difference and lowers thermal resistance, which decreased heat loss and increased the heat absorption at the production well. Therefore, the efficiency of the model was investigated within two approaches. Approach 1 was carried out for the Generic model due to having approximately same (slightly higher) thermal gradients as Tilston along its formations and approach 2 was attributed to both models. The temperature of the Generic site was estimated as a combination of transferred temperature of Tilston site from 0 to 1200 m and analytically estimated temperatures for 1200 m to 3 km depth from Eq.3. Therefore, the Generic model as a vertical extension of Tilston site developed similar thermal as Tilston model after calibration at steady state condition.

In the first approach, the thermal gradient along thermal reservoir was determined using thermal conductivity of halite (5.6 W/mK) and average thermal conductivity of all upper formations (3 W/mK) as the reservoir thermal conductivity. During the first 90 days of operation (phases 1 and 2) the temperature was changing drastically; therefore, the thermal gradient along the reservoir considering halite's thermal conductivity was compared to the average thermal conductivity during for this period and presented in Table 6.2. The thermal conductivity of the model considering halite as the thermal reservoir was less than the other model that led to the higher efficiency of a system having halite as thermal reservoir due to lower heat loss within its thermal reservoir.

Table 6.2. Thermal gradients of the reservoir considering halite and average thermal conductivities for phase 1 and phase 2.

	Halite as thermal reservoir (°C/m)	Average thermal reservoir (°C/m)
Phase 1- 1 Day	0.04	0.06
Phase 2- 90 Days	0.004	0.7
Phase 2-1 Year	0.04	0.74
Average thermal gradient	0.028	0.5

The derived temperatures for both models at the thermal reservoir are presented in Fig. 6.5. As it is shown, the temperature at the surface of the Prairie Evaporite was 2°C higher than the other model. The higher temperature was due to less temperature loss and higher thermal conductivity of the halite comparing to other rock formations. This extra 2°C provided adequate heat for generating 0.6 MW which is 6% of the designed energy of 10 MW.

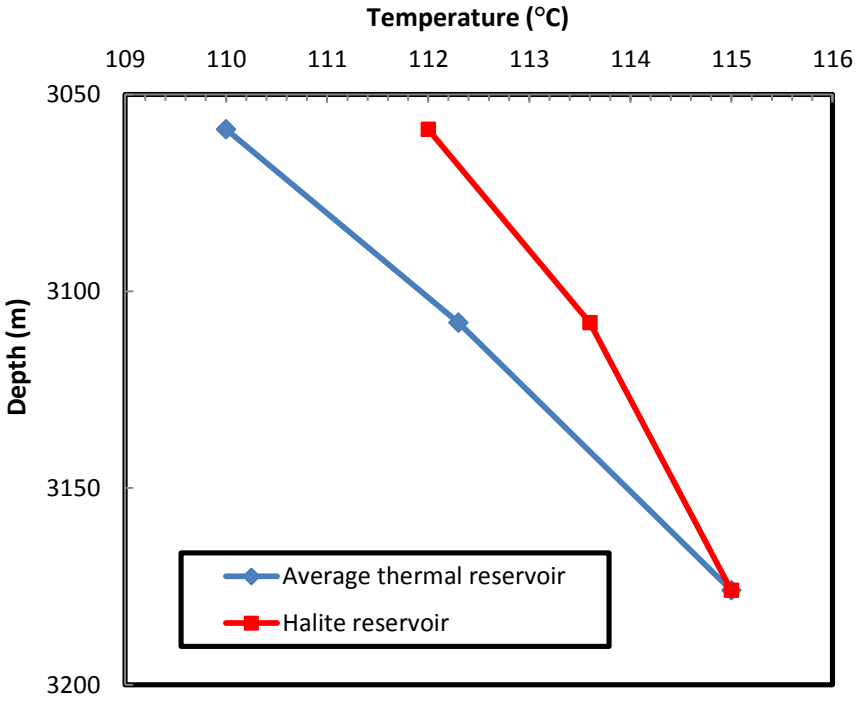

Fig. 6.5. Temperature along the thermal reservoirs with a thermal conductivity of halite and the average value of all upper formations.

In approach 2, the thermal gradients of all the upper formations of the Prairie Evaporite were compared to the reservoir's thermal gradient (Table 6.3). The lowest thermal gradient of 0.008°C/m was derived at the thermal reservoirs of Tilston site. At the Generic model, thermal gradients remained the same from 1200 m to 3 km due to the application of the analytical method in temperature estimation and calibration at steady state. The transferred temperature data for the first two layers showed the thermal gradients of 0.035 and 0.016°C/m. The second layer (shale) and the reservoir showed the lowest thermal gradients of 0.016 and 0.026°C/m. The potential thermal reservoir must develop low thermal gradients and high temperature.

Table 6.3. Thermal gradients of Tilston and Generic models within their formations.

Tilston model		Generic model	
Formations	Thermal gradient (°C/m)	Formations	Thermal gradient (°C/m)
Clay & Sandstone	0.049	Clay	0.035
Shale	0.032	Shale	0.016
Shale	0.024	Shale	0.067
Sandstone	0.054	Sandstone	0.033
Shale	0.022	Shale	0.033
Limestone	0.016	Limestone	0.033
Anhydrite	0.031	Anhydrite	0.033
Shale	0.020	Shale	0.033
Dolomite	0.027	Anhydrite	0.033
Limestone	0.038	Dolomite	0.033
Shale & Sandstone	0.023	Shale	0.033
Limestone	0.025	Limestone	0.033
Dolomite	0.027	Limestone	0.033
Limestone	0.025	Dolomite	0.033
Dolomite	0.027	Salt	0.026
Dolomite	0.025	Dolomite	0.034
Dolomite	0.023		
Salt	0.008		
Dolomite	0.011		

On one hand, the second layer containing mainly shale had the lowest thermal gradient at a depth of 1200 m, but it failed to provide enough heat for electricity production using EGS due to its low temperature (34°C). On the other hand, the Prairie Evaporite exposed low thermal gradient and high temperature at a depth of 3 km that approved the feasibility of this formation to be the thermal reservoir target.

Chapter 7. Conclusion

The main objective of this research was to determine the feasibility of a geothermal application for electricity generation using EGS from the Prairie Evaporite Formations the Williston Basin. Prairie Evaporite contains layers of halite, which has lower thermal resistance and higher thermal conductivity comparing to other types of rocks, which led to lower thermal gradients from the reservoir to the upper formations and lower drilling depth, as well as a reduction in the total cost of the project.

Summary of the research

The thermal reservoir must be able to provide enough energy for heating the production fluid up to at least 80°C, for electricity production. Therefore, the temperature at the head of the production well is the most important result of the simulation, as it determines the efficiency and overall feasibility of the geothermal system. Two sites have been selected within the Manitoban and the Saskatchewan parts of the Williston Basin. The geological maps of the basin demonstrated an increase in depth and thickness of the basin's formations from north-east to south-west. The first study area was at Tilston, due to the high volume of accessible information regarding the measured temperature and thick halite formation (180 m) at a depth of 1.5 km. The second site (called as Generic) was originally a vertical extension of Tilston

site with the Prairie Evaporite Formation at a depth of 3 km and thickness of 118 m. This site was located in the Saskatchewan part of the basin with the same geological formations as Tilston. Two numerical models were set up in FEFLOW to assess the feasibility of the sites to provide adequate heat and flow for a 10 MW electricity production power plant

At Tilston, the Prairie Evaporite's temperature was equal to 47°C in the steady state, which provided heat to increase the fluid's temperature up to 43°C at the surface of the Tilston site within 30 years of wells operation. However, the minimum required heat for electricity production was not derived at this location; the derived energy could be used for other purposes such as direct applications for factories or residential complexes, cooling/heating systems and heat pumps as discussed in section 1.2.3. By considering the insufficiency of the reservoir's temperature in providing the minimum required temperature for electricity production, the Tilston model was run at transient state to simulate the effect of EGS wells operation on the hydraulic head, the fractures impact on the reservoir's hydraulic conductivities, and heat losses through the reservoir and the production well.

The low hydraulic conductivity of thermal reservoir (1E-14 m/s) was increased by hydraulic fracturing method at the wells location to the maximum of 1E-8 m/s, which was decreased to 1E-10 and 1E-12 m/s along the lower pressure line between the wells. The brine of 6% NaCl was used as the transfer fluid due to its higher volumetric heat capacity than fresh water. The hydraulic and thermal variations became stable after 2 years of wells operation to the end of simulation time (30 years).

The Generic model was able to provide 110°C at a depth of 3 km. Formation depths was the only difference between the Tilston site and the Generic model, which affect the formations' temperature and the final derived temperature of the fluid. The final derived temperature at

the surface of the Generic model was 105°C, which provided energy for efficient electricity production.

Therefore, the Prairie Evaporite containing halite as its main component, at 3 km depth, was supplying adequate thermal energy for electricity production. Besides, the thermal gradient of the halite was significantly lower comparing to other types of rocks as presented in Table 6.3, which represented the high efficiency of halite with lower thermal resistance.

Outcome of research

The outcome of the research regarding the numerical modeling approaches, assumptions, and results were classified as following:

- By numerical modeling, temperature, hydraulic head, and pressure of saturated porous media was determined. The application of an open loop system, which was modeled by a multilayer well, depended on the hydraulic conductivity and mesh distribution significantly. The mesh system was selected fine enough to lead to the convergence in an appropriate amount of time. A very fine mesh could increase the accuracy of modeling; however, it increased the simulation time considerably. Therefore, by evaluating the mesh consistency, which was described in section 6.1, the appropriate mesh size was determined with minimum computational time. Fine mesh system, reduced the simulation error in hydraulic head estimation with wells operation.
- The location of the observation point affected the results in the surface such as recorded temperature or hydraulic head. The lengths of meshing elements were not exactly the same on various directions. The observation points, which were closer to the production well, recorded higher temperature comparing to the ones in further distances.

- The effect of BCs at the surface on simulation results was not negligible. For temperature determination, by accepting an error of 0.05°C, reliable results were derived from 10 m depth instead of the temperature at the surface of the model. This dependency increased the computation time considerably.
- On one hand, adding the hydraulic fractures increased the hydraulic conductivity of the thermal reservoir at the well screen of the injection and production well and along the fluid path from the injection to the production well. Stronger fluid transfer consequently led to less heat loss and shorter required distance for fluid to absorbed temperature, which reduced the costs of hydraulic fracturing. On the other hand, it increased the risks of seismic activities for potential fields, which required continuing monitoring.
- Pressure drop at the production well was controlled to eradicate the fluid's phase change and extensive temperature loss. The hydraulic conductivity of thermal reservoir was important in defining the allowable pressure changes.
- Measured data conducted to fewer assumptions and better simulation results. Fortunately, the sedimentary basins are popular in providing information regarding the temperature, formations, lithology, hydrostratigraphy, etc. However, the lack of information regarding recorded temperature along the drilling length was tangible. The applied analytical method for estimating the deeper formations temperature did not cover the WCSB, which was a short come of this method. To have a comprehensive knowledge of the temperature at deeper formations, the analytically derived temperatures at specific depths were compared to the few measured data at same depth to increase the accuracy of estimation.

- The impact of high temperature and pressure on density and viscosity increased the efficiency of the system for the cases which the fluid temperature changes more than 50°C between 15 to 100°C. However, for smaller temperature changes (15-50°C) the density can be assumed as a linear function of temperature and viscosity as a constant value.
- Temperature gradient for formations containing halite with 5.6W/mK thermal conductivity was twice the reservoir with a thermal conductivity of 3 W/mK.

In this research, the numerical modeling provided information regarding the final derived temperature and fluid transfer within defined study areas. The mesh distribution, BCs, parameters estimation, and ICs influenced the simulation results. It was derived that the Prairie Evaporite Formation could be used as geothermal field with capacity of providing enough energy for a 10 MW electricity power plant.

Chapter 8. Recommendations

This research presented the geological and lithological formations, numerical modeling approaches, calibrations, simulations of heat and fluid transfer and discussion the final derived temperature and pressure (hydraulic head) within specific sites. Further investigations are appreciated to promote the outcome of this research in the following fronts:

- Hydraulic fractures modeling
- Minerals dissolution and precipitation along the wells, and
- Effective thermal conductivity estimation by experimental approaches.

The geometry of the fractures along the reservoir is hypothetical in this research. The hydraulic head, pressure and temperature changes within the fractured area can be modeled using FEFLOW and the fractures size and distribution based on pressure variations can be determined. Determining the fractures size and geometry, reduce the cost of hydraulic fracturing by hindering the impractical fractures creation and reduce computational time of numerical model by optimizing the number and location of the elements.

The saturated brine will be unsaturated to most minerals at open fractures due to pressure and temperature changes which lead to salt dissolution. Mineral dissolution avoids the fractures

clogging caused by salt creeping. The effect of different minerals dissolution on the salt formation considering the fractures opening can be determined geochemical transport modeling e.g. SEAWAT (Guo and Langevin, 2002) and PHT3D (Prommer et al., 2003). The candidates of saturated brines have been introduced in the literature review. $MgCl_2$ was introduced as the most appropriate brine for heat transfer within saline formations, which can be further studied in detail by developing numerical models. The saturated brine at the production well screen will become under saturated along the production well due to temperature and pressure reduction and results in precipitation of salts. It is important to investigate the salts precipitation, its effect on the hydraulics along the production well and possible methods to diminish its effects. This technical detail has to be closely studied if geothermal energy should be derived from saline formations in the future.

The thermal properties used to investigate the heat transfer for this study were based on literature review and mostly analytical methods. By having experimental approaches to determine the thermal conductivity of the main formation's components at the proposed temperature in the laboratory, the simulation's uncertainties will be reduced.

Appendix (a) Key parameters to estimate the depth temperature relationship of four main geological formations of Canada (Grasby et al., 2012).

Region	D (km)	Q_r (mW/m^2)	A_0 (μW/m^3)	λ (W/mK)
Craton	9.6	33	1.7-3.7	1.8-3.4
Shield	8-10	33	0.9-2.6	2.6-3.4
Atlantic	8-12	40	1.6-2.3	2.6-3.4
Cordillera	10	50-60	2.0-5.0	2.6-3.4
This study	9.6	0.033	3.4	2

Appendix (b) Below equations are the frictional and dynamic pressure terms for non-artesian well design.

$$\text{Production well frictional pressure drop } = 1.89 \times 10^{-5}\, D_{Tp}\left[1+\left(\frac{D_{Dp}}{D_{Tp}}\right)^{2}\right]^{0.5}\frac{\mu^{0.21}Q_p{}^{1.79}}{d^{4.79}} \qquad \text{Eq.37}$$

$$\text{Production well dynamic pressure drop } = 9.87 \times 10^{-5}\frac{Q_p\mu}{kh}\log_{10}\left[\frac{2z}{d}\right] \qquad \text{Eq.38}$$

$$\text{Injection well frictional pressure rise } = 1.89 \times 10^{-5}\, D_{Tp}\left[1+\left(\frac{D_{Dp}}{D_{Tp}}\right)^{2}\right]^{0.5}\frac{\mu^{0.21}Q_p{}^{1.79}}{d^{4.79}} \qquad \text{Eq.39}$$

$$\text{Injection well dynamic pressure rise } = 9.87 \times 10^{-5}\frac{Q_p\mu}{kh}\log_{10}\left[\frac{2z}{d}\right] \qquad \text{Eq.40}$$

Appendix (c) Tilston geology, lithology, thickness, and hydrostratigraphy information

Layer number	Era	Period	Formation	Lithology	Thickness	Hydrostratigraphy (Palombi, 2008)
1	Cenozoic	Tertiary	Wynyard formation	Gravel Siltstone	134	Aquifer
				Clay		
				Gravel		
			Turtle mountain formation	Clay & Sandstone		Aquitard
2	Mesozoic	Cretaceous	Boissevian	Shale (Non-limy)	252	Aquitard
			Pierre shale (flat white specks)			Aquifer
			Niobrara			Aquitard
			Modern shale			
3			Favel	Shale-Limy	210	
			Ashville			Aquifer
4			Swan River	Sandstone	60	
				Shale		
				Sandstone		
5		Jurassic-Triassic	Waskada	Shale	112	Aquitard
6			Melita	Limestone	36	Aquifer
7			Reston	Anhydrite	45	
8			Amaranth-Evaporite	Shale-Teriasic	30	Aquitard
			Amaranth-Red Beds			
9	Paleozoic	Mississippian	Lodgepole	Dolomite	24	Aquifer
10				Limestone	91	
11			Bakken Formation	Shale & Sandston	42	

11	Paleozoic	Devonian	Torquay Formation-Three Forks Formation (Lyleton)	Shale		Aquitard
12			Birdbear Formation(Nisku)	Limestone	70	Aquifer
			Duperow Formation	Limestone		Aquitard
				Limestone		Aquifer
				Limestone		
13				Dolomite	30	
14				Limestone	15	
15				Dolomite	64	
16			Souris River	Limestone	15	Aquitard
17				Dolomite	73	
18				Shale	70	
				Dolostone		
			Dawson Bay	Dolomite		Aquifer
19			Prairie Evaporate	Salt	118	Aquitard
20			Winnipegosis & Elm point	Dolomite	195	Aquifer
21			Ashern	Dolomite	21	Aquitard
		Silurian	Interlake	Dolomite		Aquifer
		Ordovician	Stony Mountain	Dolomite		Aquitard
			Stony Mountain Shale	Limestone		
22			Red River	Dolomite	149	Aquifer
				Limestone		
				Dolomite		
				Limestone		
23			Winnipeg	Shale	70	Aquitard
				Sandstone		
				Shale		
				Sandstone		
24		Precambrian		Quartz	24	

Appendix (d) Temperature-depth variation for Tilston model.

Layer	Elevation (m)	Temperature (°C)
Clay & Sandstone	134	11
Shale-Non Limy	387	21
Shale-Limy	597	26
Sandstone	658	28
Shale	771	30
Limestone	808	32
Anhydrite	853	33
Shale	884	33
Dolomite	908	33
Limestone	1000	34
Shale & Sandstone	1042	35
Limestone	1113	36
Dolomite	1143	37
Limestone	1158	38
Dolomite	1222	39
Dolomite	1237	40
Dolomite	1311	42
Salt	1381	44
Dolomite	1431	47
Limestone	1500	52
Dolomite	1695	53
Shale	1716	57
Sandstone	1865	59
Quartz	1935	60

Appendix (e) Selected values for Eq.3 considering the lowest error from the root mean square method between measured and calculated temperature (Grasby et al., 2012).

Depth (m)	z (m)	Q_r (W/m^2)	A_0 ($\mu W/m^3$)	D (m)	K(W/mK)	Temperature calculated (°C)	Temperature measured (°C)
10	0	0.033	3.4E-06	9600	2	8	8
50	134	0.033	3.4E-06	9600	2	9	11
90	253	0.033	3.4E-06	9600	2	10	9
134	210	0.033	3.4E-06	9600	2	11	11
387	61	0.033	3.4E-06	9600	2	18	21
597	113	0.033	3.4E-06	9600	2	23	26
658	37	0.033	3.4E-06	9600	2	25	28

Appendix (f) Density, pressure, and temperature of the Tilston site's formations.

Layer	Density (kg/m^3)	Pressure (MPa)	Temperature (°C)
Clay & Sandstone	2050	2.75	10.62
Shale-Non Limy	1586	6.76	20.55
Shale-Limy	2691	12.42	26.48
Sandstone	1601	13.39	27.54
Shale	1586	15.18	30.30
Limestone	1554	15.75	32.10
Anhydrite	2970	17.11	32.78
Shale	1586	17.59	32.83
Dolomite	2899	18.30	33.28
Limestone	1554	19.72	34.48
Shale & Sandstone	1588	20.40	34.54
Limestone	1554	21.49	36.45
Dolomite	2899	22.38	37.29
Limestone	1554	22.61	37.71
Dolomite	2899	24.47	39.46
Dolomite	1554	24.70	39.88
Dolomite	2899	26.83	41.88
Salt	2899	28.86	43.80
Dolomite	2323	31.62	47.05
Limestone	2899	37.27	52.38
Dolomite	1554	37.61	52.96
Shale	2021	40.62	57.04
Sandstone	1592	41.01	58.96
Quartz	1592	41.01	59.63

Appendix (g) Tilston formations effective specific heat capacity values.

Layer	T_1(°C)	Cp_{T1}	T_2(°C)	Cp_{T2}	Specific heat capacity (J/kg/K)
Clay & Sandstone	20	0.742	10.62	0.734	1.57
Shale-Non Limy	20	0.742	20.55	0.750	1.29
Shale-Limy	20	0.742	26.48	0.760	2.22
Sandstone	20	0.742	27.54	0.762	1.27
Shale	20	0.742	30.30	0.766	1.32
Limestone	20	0.742	32.10	0.769	1.16
Anhydrite	20	0.742	32.78	0.770	2.49
Shale	20	0.742	32.83	0.770	1.33
Dolomite	20	0.742	33.28	0.771	2.64
Limestone	20	0.742	34.48	0.773	1.16
Shale & Sandstone	20	0.742	34.54	0.773	1.33
Limestone	20	0.742	36.45	0.776	1.17
Dolomite	20	0.742	37.29	0.777	2.67
Limestone	20	0.742	37.71	0.778	1.17
Dolomite	20	0.742	39.46	0.781	2.68
Dolomite	20	0.742	39.88	0.781	1.17
Dolomite	20	0.742	41.88	0.784	2.69
Salt	20	0.742	43.80	0.787	2.70
Dolomite	20	0.742	47.05	0.792	2.51
Limestone	20	0.742	52.38	0.800	2.75
Dolomite	20	0.742	52.96	0.801	2.25
Shale	20	0.742	57.04	0.807	1.48
Sandstone	20	0.742	58.96	0.810	1.78
Quartz	20	0.742	59.63	0.798	1.33

Appendix (h) Effective thermal conductivity, specific heat capacity, volumetric heat capacity, and porosity for Tilston model.

Layer	Thermal conductivity (W/mK)	Effective thermal conductivity (W/mK)	Effective specific heat capacity (J/kg/K)	Volumetric heat capacity ($J/m^3°C$)	Porosity (-)
Clay & Sandstone	3.042	3.040	798.995	1.638	0.42
Shale-Non Limy	1.400	1.412	837.962	1.329	0.06
Shale-Limy	1.400	1.420	839.181	2.258	0.06
Sandstone	4.060	5.330	810.319	1.297	0.39
Shale	1.400	1.400	844.552	1.339	0.06
Limestone	2.800	2.910	752.056	1.169	0.30
Anhydrite	6.500	6.500	845.913	2.512	0.02
Shale	1.400	1.400	846.440	1.342	0.06
Dolomite	3.100	4.448	923.561	2.677	0.26
Limestone	2.800	2.903	756.397	1.175	0.30
Shale & Sandstone	2.350	1.400	851.668	1.353	0.06
Limestone	2.800	2.896	757.859	1.178	0.30
Dolomite	3.100	4.461	927.894	2.690	0.26
Limestone	2.800	2.892	760.089	1.181	0.30
Dolomite	4.200	4.448	929.814	2.696	0.26
Dolomite	2.800	2.879	761.820	1.184	0.30
Dolomite	4.200	4.434	931.509	2.700	0.26
Salt	4.200	4.423	933.146	2.705	0.26
Dolomite	5.700	5.175	1078.029	2.504	0.50
Limestone	4.700	4.373	938.828	2.722	0.26
Dolomite	2.800	2.846	768.281	2.227	0.30
Shale	2.904	2.834	943.443	1.466	0.30
Sandstone	2.137	4.980	867.938	1.754	0.06
Quartz	5.600	6.200	833.697	1.327	0.001

Appendix (i) The used coefficients of pure water for temperature-dependent density function.

Parameters	Coefficients
a_1	9.998396e+02
a_2	6.764771e-02
a_3	-8.993699e-03
a_4	9.143518e-05
a_5	-8.907391e-07
a_6	5.291959e-09
a_7	-1.359813e-11

Appendix (j) RMS between the generic and calculated thermal gradient for the Tilston site (Total RMS=0.03).

Depth (m)	Generic thermal gradient (°C/m)	Simulated thermal gradient (°C/m)	RMS
10	0.1716	0.0453	0.0160
15	0.0206	0.0519	0.0010
20	0.0206	0.0519	0.0010
25	0.0206	0.0519	0.0010
30	0.0206	0.0599	0.0015
40	0.0206	0.0599	0.0015
90	0.0206	0.0519	0.0010
134	0.0284	0.0440	0.0002
387	0.0393	0.0327	0.0000
597	0.0282	0.0245	0.0000
658	0.0174	0.0551	0.0014
771	0.0245	0.0227	0.0000
808	0.0492	0.0166	0.0011
853	0.0148	0.0252	0.0001
884	0.0016	0.0208	0.0004
908	0.0187	0.0273	0.0001
1000	0.0131	0.0389	0.0007
1042	0.0013	0.0181	0.0003
1113	0.0274	0.0241	0.0000
1143	0.0274	0.0275	0.0000
1158	0.0274	0.0233	0.0000
1222	0.0274	0.0275	0.0000
1237	0.0274	0.0230	0.0000
1311	0.0274	0.0218	0.0000
1381	0.0274	0.0077	0.0004
1431	0.0274	0.0109	0.0003
1500	0.0274	0.0325	0.0000
1695	0.0273	0.0284	0.0000
1716	0.0274	0.0298	0.0000
1865	0.0273	0.0201	0.0001
1935	0.0274	0.0094	0.0003
1960	0.0274	0.0089	0.0003

Appendix (k) Final calibrated thermal conductivities of the Tilston site for each formation.

Layer	Thermal conductivity (W/mK)	Effective thermal conductivity (W/mK)
Clay & Sandstone	1.64	1.36
Shale-Non Limy	2.00	2.02
Shale-Limy	2.00	2.03
Sandstone	2.70	2.73
Shale	2.00	1.48
Limestone	2.80	2.94
Anhydrite	6.50	5.20
Shale	2.00	2.05
Dolomite	3.10	3.22
Limestone	2.80	2.92
Shale & Sandstone	2.50	2.57
Limestone	2.80	2.91
Dolomite	3.10	3.23
Limestone	2.80	2.90
Dolomite	3.10	3.63
Dolomite	2.80	2.88
Dolomite	3.10	3.68
Salt	4.00	3.72
Dolomite	6.23	5.20
Limestone	4.70	3.27
Dolomite	2.80	2.80
Shale	2.90	2.77
Sandstone	4.20	4.24
Quartz	5.60	7.14

Appendix (l) Layering, lithology, and thicknesses for the Generic model.

Layer Number	Era	Period	Formation	Lithology	Thickness
1	Cenozoic	Tertiary	Wynyard Formation	Gravel Siltstone	590
				Clay	
				Gravel	
			Turtle Mountain Formation	Clay & Sandstone	
2	Mesozoic	Cretaceous	Boissevain	Shale (Non-limy)	490
			Pierre Shale (Flat White Specks)		
			Niobrara		
			Modern Shale		
3			Favel	Shale (Limy)	207
			Ashville		
4			Swan River	Sandstone	27
				Shale	
				Sandstone	
5		Jurassic-Triassic	Waskada	Shale	130
6			Melita	Limestone	76
7			Reston	Anhydrite	147
8			Amaranth-Evaporite	Shale-Triassic	15
			Amaranth-Red Beds		

9	Paleozoic	Mississippian	Charles Formation	Anhydrite	295
10			Lodgepole	Dolomite	187
11			Bakken Formation	Shale And Sandstone-Limy	580
		Devonian	Torquay Formation-Three Forks Formation	Shale	
12			Birdbear Formation (Nisku)	Limestone	79
			Duperow Formation	Limestone	
				Limestone	
				Limestone	
				Dolomite	
				Limestone	
				Dolomite	
13			Souris River	Limestone	137
				Dolomite	
				Shale	
				Dolostone	
14			Dawson Bay	Dolomite	95
15			Prairie Evaporate	Salt	118
16			Winnipegosis & Elm Point	Dolomite	849
			Ashern	Dolomite	

Appendix (m) Temperature, density, and pressure of the Generic model.

Layer	Temperature (°C)	Density (kg/m^3)	Pressure (MPa)
Clay	26.48	2,050	12.10
Shale	34.54	1,586	19.87
Shale	48.33	2,691	25.44
Sandstone	49.26	1,601	25.89
Shale	53.59	1,586	27.96
Limestone	56.13	1,554	29.15
Anhydrite	61.00	2,970	33.51
Shale	61.53	1,586	33.76
Anhydrite	71.28	2,970	42.52
Dolomite	77.47	2,899	47.95
Shale	96.51	1,588	57.16
Limestone	99.15	2,227	58.92
Limestone	103.70	1,554	61.06
Dolomite	106.86	2,899	63.82
Salt	109.98	1,592	64.44
Dolomite	135.87	2,899	89.07

Appendix (n) Thermal properties of the Generic model.

Layer	Effective thermal conductivity(W/mK)	Effective specific heat capacity (J/kg/K)	Volumetric heat capacity (J/m^3 °C)	Porosity (-)
Clay	4.17	786.36	1.61	0.42
Shale	2.02	841.85	1.34	0.06
Shale	2.03	851.45	2.29	0.06
Sandstone	2.69	852.74	1.37	0.39
Shale	1.48	858.72	1.36	0.06
Limestone	2.74	767.30	1.19	0.30
Anhydrite	5.20	868.82	2.58	0.02
Shale	2.05	869.53	1.38	0.06
Anhydrite	3.22	882.56	2.62	0.26
Dolomite	2.92	969.23	2.81	0.23
Shale	2.57	915.06	1.45	0.28
Limestone	2.51	817.27	1.82	0.30
Limestone	4.36	822.29	1.28	0.26
Dolomite	4.40	1,009.65	2.93	0.26
Salt	5.6	1,166.87	1.86	0.50
Dolomite	4.92	1,047.05	3.04	0.26

- *Bibliography*

ABDULAGATOVA, Z., ABDULAGATOV, I. & EMIROV, V. 2009. Effect of temperature and pressure on the thermal conductivity of sandstone. *International Journal of Rock Mechanics and Mining Sciences,* 46**,** 1055-1071.

AGEMAR, T., WEBER, J. & SCHULZ, R. 2014. Deep geothermal energy production in Germany. *Energies,* 7**,** 4397-4416.

AMARAL, L. C. M. 2014. Assessment of Geothermal Energy from Saline Structures. University of Manitoba.

ARORA, K., CAZENAVE, A., ENGDAHL, E. R., KIND, R., MANGLIK, A., ROY, S., SAIN, K., UYEDA, S. & GUPTA, H. 2011. *Encyclopedia of Solid Earth Geophysics*, Springer Science & Business Media.

BARTON, N. 1973. Review of a new shear-strength criterion for rock joints. *Engineering Geology,* 7**,** 287-332.

BEZYS, R. K. & MCCABE, H. R. 1996. Lower to middle Paleozoic stratigraphy of southwestern Manitoba. Geological Association of Canada/Mineralogical Association of Canada Annual Meeting, Winnipeg, Manitoba.

BLÖCHER, M., ZIMMERMANN, G., MOECK, I., BRANDT, W., HASSANZADEGAN, A. & MAGRI, F. 2010. 3D numerical modeling of hydrothermal processes during the lifetime of a deep geothermal reservoir. *Geofluids,* 10**,** 406-421.

BROWN, D. W. A hot dry rock geothermal energy concept utilizing supercritical CO2 instead of water. of the twenty-fifth workshop on geothermal reservoir engineering, Stanford University, 2000. 233-238.

BRUNO, M. & NAKAGAWA, F. Pore pressure influence on tensile fracture propagation in sedimentary rock. International journal of rock mechanics and mining sciences & geomechanics abstracts, 1991. Elsevier, 261-273.

CACACE, M., KAISER, B. O., LEWERENZ, B. & SCHECK-WENDEROTH, M. 2010. Geothermal energy in sedimentary basins: What we can learn from regional numerical models. *Chemie der Erde - Geochemistry,* 70, Supplement 3**,** 33-46.

CHEN, M., TOMPSON, A. F. B., MELLORS, R. J. & ABDALLA, O. 2015. An efficient optimization of well placement and control for a geothermal prospect under geological uncertainty. *Applied Energy,* 137**,** 352-363.

CON-STRUC. 2015. *World energy consumption.* [Online]. BP Statistical Review of World Energy. Available: https://upload.wikimedia.org/wikipedia/commons/3/3a/World_energy_consumption.svg.

DEEP. 2014. *Deep earth energy porduction corp* [Online]. Project updates, 2014-08-22 Pre-feasibility Updates. Available: http://www.deepcorp.ca/publications/.

DEHKORDI, S. E., OLOFSSON, B. & SCHINCARIOL, R. A. 2014. Effect of groundwater flow in vertical and horizontal fractures on borehole heat exchanger temperatures. *Bulletin of Engineering Geology and the Environment,* 74**,** 479-491.

DEHKORDI, S. E., OLOFSSON, B. & SCHINCARIOL, R. A. 2015. Effect of groundwater flow in vertical and horizontal fractures on borehole heat exchanger temperatures. *Bulletin of Engineering Geology and the Environment,* 74**,** 479-491.

DIERSCH, H.-J. 2013. *FEFLOW: finite element modeling of flow, mass and heat transport in porous and fractured media*, Springer Science & Business Media.

DIERSCH, H. 2002. FEFLOW reference manual. *Institute for Water Resources Planning and Systems Research Ltd,* 278.

DOMENICO, P. A. & SCHWARTZ, F. W. 1998. *Physical and chemical hydrogeology*, Wiley New York.

DUCHANE, D. & BROWN, D. 2002. Hot dry rock (HDR) geothermal energy research and development at Fenton Hill, New Mexico. *Geothermal Heat Center Bulletin*.

EPPELBAUM, L., KUTASOV, I. & PILCHIN, A. 2014. Thermal properties of rocks and density of fluids. *Applied Geothermics.* Springer.

FASINA, O. O., FLEMING, H. P. & MCFEETERS, R. F. 2002. Thermal and rheological properties of brine from fermented and sulfite-preserved cucumbers. *Journal of Food Process Engineering,* 25**,** 307-322.

FEIGIE, M., SICHTING, S. & HIELSCHER, P. 2008. Geocando 1.1. Technische Universität Bergakademie Fireiberg, Department of Geosciences.

FERGUSON, G. & GRASBY, S. E. 2014. The geothermal potential of the basal clastics of Saskatchewan, Canada. *Hydrogeology Journal,* 22**,** 143-150.

FISHER, M. K. & WARPINSKI, N. R. 2012. Hydraulic-fracture-height growth: Real data. *SPE Production & Operations,* 27**,** 8-19.

FRANCO, A. & VACCARO, M. 2014. Numerical simulation of geothermal reservoirs for the sustainable design of energy plants: A review. *Renewable and Sustainable Energy Reviews,* 30**,** 987-1002.

GEORGE, P. L. 1992. *Automatic mesh generation: applications to finite element methods*, John Wiley & Sons Inc.

GHOSH, T. & PRELAS, M. 2011. *Energy resources and systems: volume 2: renewable resources*, Springer Science & Business Media.

GOVERNMENT OF CANADA. 2015. *Environment and natural resources, past weather and climate* [Online]. Available: http://climate.weather.gc.ca/historical_data/search_historic_data_e.html.

GOVERNMENT OF MANITOBA & MANITOBA MINERAL RESOURCES. 2014. *Petroleum Maps GIS* [Online]. Available: http://www.gov.mb.ca/iem/petroleum/gis/.

GRASBY, S. E., ALLEN, D. M., BELL, S., CHEN, Z., FERGUSON, G., JESSOP, A., KELMAN, M., KO, M., MAJOROWICZ, J., MOORE, M., RAYMOND, J. & THERRIEN, R. 2012. Geothermal Energy Resource Potential of Canada. Geological Survey of Canada.

GRINGARTEN, A. & SAUTY, J. 1975. A theoretical study of heat extraction from aquifers with uniform regional flow. *Journal of Geophysical Research,* 80**,** 4956-4962.

GUO, W. & LANGEVIN, C. D. 2002. User's guide to SEAWAT; a computer program for simulation of three-dimensional variable-density ground-water flow. *Techniques of water-resources investigations.* Supersedes OFR 01-434 ed.

GUPTA, H. K. & ROY, S. 2006. *Geothermal Energy : An Alternative Resource for the 21st Century,* Amsterdam, NLD, Elsevier Science & Technology.

HARRISON, R., MORTIMER, N. & SMARASON, O. 2013. *Geothermal Heating: A handbook of engineering economics,* Elsevier.

HERBERT, A. W., JACKSON, C. P. & LEVER, D. A. 1988. Coupled groundwater flow and solute transport with fluid density strongly dependent upon concentration. *Water Resources Research,* 24**,** 1781-1795.

INGEBRITSEN, S. E. & WARD, S. E. 1998. *Groundwater in geologic process,* Cambridge New York, NY, USA Cambridge University Press

JESSOP, A. 1990. Comparison of industrial and high-resolution thermal data in a sedimentary basin. *pure and applied geophysics,* 133**,** 251-267.

JESSOP, A. M. & VIGRASS, L. W. 1989. Geothermal measurements in a deep well at Regina, Saskatchewan. *Journal of Volcanology and Geothermal Research,* 37**,** 151-166.

KARASINSKI, D. R. 2006. Sedimentology and hydrocarbon potential of the Devonian Three Forks and Mississippian Bakken Formations, Sinclair Area, southeast Saskatchewan-southwest Manitoba.

KARVOUNIS, D., GISCHIG, V. & WIEMER, S. EGS probabalistic seismic hazard assessment with 3-D discrete fracture modeling. Proceedings of the Thirty-Ninth Workshop on Geothermal Reservoir Engineering, Stanford, 2014.

KENT, D. & CHRISTOPHER, J. 1994. Geological history of the Williston Basin and Sweetgrass arch. *Geological atlas of the Western Canada Sedimentary Basin.* Canadian Society of Petroleum Geologists and the Alberta Research Council.

KJARTANSSON, K. D. 2011. Effect of Well Diameter on Productivity of High Temperature Geothermal Wells.

KLASSEN, R. W., WYDER, J. E. & BANNATYNE, B. B. 1970. Bedrock Topography and Geology of Southerm Manitoba. Geological Survey of Canada.

LACHENBRUCH, A. H. 1970. Crustal temperature and heat production: Implications of the linear heat-flow relation. *Journal of Geophysical Research,* 75**,** 3291-3300.

LAW, M. & COLLINS, A. 2013. *Getting to know ArcGIS for desktop,* Esri press.

LEWIS, J. F. & HYNDMAN, R. D. 1976. Oceanic heat flow measurements over the continental margins of eastern Canada. *Canadian Journal of Earth Sciences,* 13**,** 1031-1038.

LI, M. & LIOR, N. 2015. Energy analysis for guiding the design of well systems of deep Enhanced Geothermal Systems. *Energy,* 93, Part 1**,** 1173-1188.

LIM, K., LEE, S. & LEE, C. 2007. An experimental study on the thermal performance of ground heat exchanger. *Experimental thermal and fluid science,* 31**,** 985-990.

LUMB, J. 1981. Prospecting for geothermal resources. *Rybach L, Muffler LJP (eds) Geothermal systems, principles and case histories. Wiley, New York***,** 77-108.

MAJOROWICZ, J. & GRASBY, S. E. 2010. High Potential Regions for Enhanced Geothermal Systems in Canada. *Natural Resources Research,* 19**,** 177-188.

MCCOY, J., JOHNSTON, K. & INSTITUTE, E. S. R. 2001. *Using ArcGIS spatial analyst: GIS by ESRI*, Environmental Systems Research Institute.

MEEK, K. Precambrian of the Canadian Williston Basin. 1958. Williston Basin Symposium.

MEER, F. V. D., HECKER, C., VAN RUITENBEEK, F., VAN DER WERFF, H., DE WIJKERSLOOTH, C. & WECHSLER, C. 2014. Geologic remote sensing for geothermal exploration: A review. *International Journal of Applied Earth Observation and Geoinformation,* 33**,** 255-269.

MOHAN, A. R., TURAGA, U., SHEMBEKAR, V., ELSWORTH, D. & PISUPATI, S. V. 2013. Utilization of carbon dioxide from coal-based power plants as a heat transfer fluid for electricity generation in enhanced geothermal systems (EGS). *Energy,* 57**,** 505-512.

NICOLAS, M. P. B. & BARCHYN, D. 2008. Williston Basin Project (Targeted Geoscience Initiative II):Summary report on Paleozoic stratigraphy, mapping and hydrocarbon assessment, southwestern Manitoba; Manitoba Science, Technology, Energy and Mines, Manitoba Geological Survey.

ONDRAK, R., WENDEROTH, F., SCHECK, M. & BAYER, U. 1998. Integrated geothermal modeling on different scales in the Northeast German basin. *Geologische Rundschau,* 87**,** 32-42.

OSADETZ, K. G., KOHN, B. P., FEINSTEIN, S. & O'SULLIVAN, P. B. 2002. Thermal history of Canadian Williston basin from apatite fission-track thermochronology—implications for petroleum systems and geodynamic history. *Tectonophysics,* 349**,** 221-249.

PALOMBI, D. D. 2008. *Regional Hydrogeological Characterization Of The Northeastern Margine In The Willisotn Basin.* University of Alberta.

PÁLSSON, H. 2011. Simulation of two phase flow in a geothermal well. *Lecture notes in the course VÉL203F Geothermal Systems at the University of Iceland*.

PANEL, H. D. R. A. 1977. Hot dry rock geothermal energy'status of exploration and assessment. *Energy Research and Development Administration Report ERDA-77-74, Energy Research and Development Administration, Washington, DC*.

PETERSEN, K. & LERCHE, I. 1995. Quantification of thermal anomalies in sediments around salt structures. *Geothermics,* 24**,** 253-268.

PINE, R. & BATCHELOR, A. Downward migration of shearing in jointed rock during hydraulic injections. International Journal of Rock Mechanics and Mining Sciences & Geomechanics Abstracts, 1984. Elsevier, 249-263.

PLUMMER, L. N., PARKHURST, D., FLEMING, G. & DUNKLE, S. 1988. A computer program incorporating Pitzer's equations for calculation of geochemical reactions in brines.

POLSKY, Y., CAPUANO, L., FINGER, J., HUH, M., KNUDSEN, S., CHIPMANSURE, A., RAYMOND, D. & SWANSON, R. 2008. Enhanced geothermal systems (EGS) well construction technology evaluation report. *Sandia National Laboratories, Sandia Report, SAND2008-7866***,** 1-108.

PROMMER, H., BARRY, D. & ZHENG, C. 2003. MODFLOW/MT3DMS-Based Reactive Multicomponent Transport Modeling. *Ground Water,* 41**,** 247-257.

RAMAZANOVA, A. & EMIROV, S. 2012a. Baric and temperature dependences for the thermal conductivity of sedimentary rocks. *Bulletin of the Russian Academy of Sciences: Physics,* 76**,** 1152-1156.

RAMAZANOVA, A. & EMIROV, S. 2012b. Effect of pressure and temperature on the thermal conductivity of siltstone and dolomite. *Bulletin of the Russian Academy of Sciences: Physics,* 76**,** 125-127.

ROBERTS, V. W. 1978. Geothermal Energy Prospects for the Next 50 Years. *Electric Power Research Institute (EPRI), Report ER-611-SR***,** 4-1.

ROBERTSON, E. C. 1988. Thermal properties of rocks. US Geological Survey.

ROSCOE MOSS COMPANY 1990. *Handbook of ground water development*, John Wiley & Sons.

ROWLEY, J. C. 1982. Worldwide geothermal resources. In: Handbook of Geothermal Energy. Gulf Publishing, Houston, TX, USA. 44-176.

ROYLE, A., CLAUSEN, F. & FREDERIKSEN, P. 1981. Practical universal kriging and automatic contouring. *Geoprocessing,* 1**,** 377-394.

SAEID, S., AL-KHOURY, R. & BARENDS, F. 2013. An efficient computational model for deep low-enthalpy geothermal systems. *Computers & Geosciences,* 51**,** 400-409.

SCHECK, M. & BAYER, U. 1999. Evolution of the Northeast German Basin — inferences from a 3D structural model and subsidence analysis. *Tectonophysics,* 313**,** 145-169.

SPYCHER, N. & PRUESS, K. 2010. A Phase-Partitioning Model for CO2–Brine Mixtures at Elevated Temperatures and Pressures: Application to CO2-Enhanced Geothermal Systems. *Transport in Porous Media,* 82**,** 173-196.

STOBER, I. & BUCHER, K. 2013. Enhanced-Geothermal-Systems, Hot-Dry-Rock Systems, Deep-Heat-Mining. *Geothermal Energy.* Springer.

TESTER, J. W. 2005. *Sustainable energy: choosing among options*, MIT press.

TETRA TECHNOLOGIES, I. 2014. *Engineered Solution Guide* [Online]. Available: solutionsguide.tetratec.com/getFile.asp?File_Content_ID=2437.

VALBERG, T. 2005. Temperature calculations in production and injection wells. Faculty of Engineering Science and Technology, NTNU.

VIGRASS, L., JESSOPE, A. & BRUNSKIL, B. 2007. Regina Geothermal Project; in Summary of Investigations 2007. Saskatchewan Geological Survey, Sask. Industry Resources, Mics. Rep. 2007-4.1, CD-ROM. Paper A-2.

VOSTEEN, H.-D. & SCHELLSCHMIDT, R. 2003. Influence of temperature on thermal conductivity, thermal capacity and thermal diffusivity for different types of rock. *Physics and Chemistry of the Earth, Parts A/B/C,* 28**,** 499-509.

WAPLES, D. W. & WAPLES, J. S. 2004. A review and evaluation of specific heat capacities of rocks, minerals, and subsurface fluids. Part 1: Minerals and nonporous rocks. *Natural resources research,* 13**,** 97-122.